UNIVERSIDAD MICHOACANA
DE SAN NICOLÁS DE HIDALGO

Facultad de Ingeniería Eléctrica
División de Estudios de Posgrado

Methodologies for Multiterminal AC-DC Transmission Grids: Power Flow, State Estimation and Frequency Tracking

by
Ricardo Martínez Parrales

A thesis presented in compliance with the requirements
for the degree of Doctor of Science
in Electrical Engineering

Advisor: Claudio Rubén Fuerte Esquivel, PhD.
Co-advisor: Boris Adrián Alcaide Moreno, PhD.

Morelia, Michoacán
August 2019

METHODOLOGIES FOR MULTITERMINAL AC-DC TRANSMISSION GRIDS: POWER FLOW, STATE ESTIMATION AND FREQUENCY TRACKING

Los Miembros del Jurado de Examen de Grado aprueban la **Tesis de Doctorado en Ciencias en Ingeniería Eléctrica, Opción en Sistemas Eléctricos** de ***Ricardo Martínez Parrales.***

Dr. Fernando Ornelas Téllez
Presidente del Jurado

Dr. Claudio Rubén Fuerte Esquivel
Director de Tesis

Dr. Boris Adrian Alcaide Moreno
(Co-director)

Dr. J. Aurelio Medina Rios
Vocal

Dr. César Ángeles Camacho
Revisor Externo (UNAM)

Dr. Roberto Tapia Sánchez
Jefe de la División de Estudios de Posgrado
de la Facultad de Ingeniería Eléctrica. UMSNH
(Por reconocimiento de firmas)

UNIVERSIDAD MICHOACANA DE SAN NICOLÁS DE HIDALGO
Agosto 2019

To my lovely wife Adriana

for her incredible support

and company in this journey.

Abstract

The aim of this thesis is the proposal of a power flow and a static state estimation approaches suitable for electric power transmission systems containing fully controlled multi-terminal high voltage direct current networks. An integrated electric circuit model of the voltage source converter station is proposed in order to determine the state variables associated with the AC-DC interface, constrained to its physical limits, together with the nodal voltages associated with the AC and DC networks, as well as the duty cycle of the DC-DC converters, for a unified solution in a single frame of reference of positive sequence.

A new approach to incorporate inequality constraints into the equality constrained weighted least squares state estimator, without modifying the way in which this estimator is formulated and solved is presented. The inequality constraints are first represented as complementarity constraints, which are then transformed to equality constraints by using the Fischer-Burmeister merit function. The state estimation problem is formulated based on Hachtel's augmented matrix method in order to directly consider the physical constraints associated with the AC-DC network.

In addition, a new technique to perform multiple bad data analysis is proposed in which the original level of measurement redundancy is maintained unaltered during the estimation process. In this context, this work also aims to provide a numerical assessment of the suitability of applying such bad data analysis for detecting, identifying and correcting or eliminating multiple measurements with gross errors under Gaussian and non-Gaussian noises.

Moreover, this thesis proposes a formulation to estimate the frequency at all the buses of a transmission system. Such formulation is derived from a tracking state estimation containing SCADA and PMU measurements and is intended for the detection of system anomalies related to frequency oscillations.

All the proposals are duly presented and their validity and effectiveness are fully demonstrated by numerical examples.

Key words: SCADA, PMU, Bad Data, Voltage Source Converter, Oscillations.

Resumen

El objetivo de esta tesis es la propuesta de enfoques para el estudio de flujos de potencia de estimación de estado estático adecuado para sistemas de transmisión de energía eléctrica que contengan redes de corriente continua de alto voltaje multi-terminales totalmente controladas. Se propone un modelo de circuito eléctrico integrado de la estación convertidora de fuente de voltaje para determinar las variables de estado asociadas con la interfaz AC-DC, restringidas a sus límites físicos, junto con los voltajes nodales asociados con las redes AC y DC, así como El ciclo de trabajo de los convertidores DC-DC, para una solución unificada en un solo marco de referencia de secuencia positiva.

Se presenta un nuevo enfoque para incorporar restricciones de desigualdad en el estimador de estado de mínimos cuadrados ponderados con restricciones de igualdad, sin modificar la forma en que se formula y resuelve este estimador. Las restricciones de desigualdad se representan primero como restricciones de complementariedad, que luego se transforman en restricciones de igualdad mediante el uso de la función de mérito Fischer-Burmeister. El problema de estimación de estado se formula con base al método de matriz aumentada de Hachtel para considerar directamente las restricciones físicas asociadas con la red AC-DC.

Además, se propone una nueva técnica para realizar el análisis de múltiples datos erróneos en la que el nivel original de redundancia de medición se mantiene inalterado durante el proceso de estimación. En este contexto, este trabajo también tiene como objetivo proporcionar una evaluación numérica de la idoneidad de aplicar dicho análisis de datos incorrectos para detectar, identificar y corregir o eliminar múltiples mediciones con errores graves bajo ruidos gaussianos y no gaussianos.

Finalmente, esta tesis propone una formulación para estimar la frecuencia en todos los buses de un sistema de transmisión. Dicha formulación se deriva de un estimador de estado de seguimiento que contiene mediciones SCADA y PMU y está destinada a la detección de anomalías del sistema relacionadas con oscilaciones de frecuencia.

Todas las propuestas se presentan debidamente y su validez y eficacia se demuestran plenamente mediante ejemplos numéricos.

Palabras clave: SCADA, PMU, Datos erróneos, Convertidor de fuente de voltaje, Oscilaciones.

Acknowledgements

First of all, I appreciate the time and patience granted by my advisor Dr. Claudio Fuerte Esquivel, as well as the opportunity to work with him. His advice has been an invaluable help during this process. His experiences have been of paramount importance to have a clear view about the qualities that a great scientific researcher must have.

To my wife, the most important person in the world for me, for her support, patience and love.

To my co-advisor, Dr. Boris Alcaide Moreno, for all his contributions related to the development of the proposals, especially those related to the real-time operation requirements of the Mexican system.

To my parents and friends, they always know how to cheer me up.

To the classmates: Rafa, Omar, Jaqueline, Jose Luis and Uriel for the help given as well as the moments of laughter and talks.

To my reviewers, their comments have improved the quality of this work.

To the professors and workers of the university for their daily work.

To the national council of science and technology (CONACyT) for the financial support through the scholarship 268680.

Financial support given by CONACyT, México, through the project CB-256680 and by the Fondo de Sustentabilidad Energética SENER-CONACyT, México, under grants 246949 and 249795 is gratefully acknowledged.

Contents

List of Figures

List of Tables

Abbreviations

AC	Alternating current
BAEVA	Biggest absolute error of estimated voltage angle
BAEVM	Biggest absolute error of estimated voltage magnitude
BDA	Bad data analysis
BDCI	Bad data correctly identified
COI	Center of inertia
DC	Direct current
DFIG	Doubly-fed induction generator
DSIC	Double-sided inequality constraints
ECLS	Equality constrained least squares
ECC	Energy control center
EEV	Error of estimated variables
FACTS	Flexible AC transmission systems
FBMF	Fisher-Burmeister merit function
GMIIB	Good measurements incorrectly identified as bad
GPS	Global positioning system
GSC	Grid side converter
HVDC	High voltage direct current
IBD	Identified bad data
ICSSE	Inequality constrained static state estimation
LAV	Least absolute value
LNER	Largest normalized estimated residual
LNERT	Largest normalized estimated residual test
LNRT	Largest normalized residual test
LTC	Load tap changer
MAEVA	Mean absolute error of estimated voltage angle
MAEVM	Mean absolute error of estimated voltage magnitude
MSC	Machine side converter
MSE	Mean squared errors
MTDC	Multi-terminal high voltage direct current
NCP	Nonlinear complementary problem
NER	Normalized estimated residual

NR	Newton Raphson
OLTC	On load tap changing
OPF	Optimal power flow
PCC	Point of common coupling
PF	Power flow
PLL	Phase loop locked
PMSG	Permanent magnet synchronous generator
PMU	Phasor measurement units
PS	Projection statistics
PWM	Pulse width modulation
RSC	Rotor side converter
RTU	Remote terminal units
SBD	Suspected bad data
SCADA	Supervisory control and data acquisition
SE	State estimation
SSE	Static state estimation
TSE	Tracking state estimation
VSC	Voltage source converter
WLS	Weighted least squares

Nomenclature

m_a	VSC modulation index.
Q_{vsc}	VSC reactive power.
ϕ	VSC fire angle.
R_1	VSC conducting losses modeling resistance.
G_{sw}	VSC switching losses modeling conductance.
$\bar{\boldsymbol{V}}_i$	Complex voltage value at the *i*-th node.
$\boldsymbol{V}_{AC}$	Vector of AC voltage magnitudes.
$\boldsymbol{\theta}_{AC}$	Vector of AC voltage angles.
V_i	Voltage magnitude at the *i*-th node.
θ_i	Voltage angle at the *i*-th node.
$\bar{\boldsymbol{Y}}_s$	Complex admittance value on element *s*.
G_s	Conductance on element *s*.
B_s	Susceptance on element *s*.
R_s	Resistance on element *s*.
X_s	Reactance on element *s*.
$\bar{\boldsymbol{Y}}_{km}$	Complex serial admittance from node *k* to node *m*.
G_{km}	Serial conductance from node *k* to node *m*.
B_{km}	Serial susceptance from node *k* to node *m*.
P_{km}	Active power flowing from node *k* to node *m*.
P_i	Active power injected at node *i*.
Q_{km}	Reactive power flowing from node *k* to node *m*.
Q_i	Reactive power injected at node *i*.
V_i^{sp}	Specified voltage magnitude to control at the *i*-th node.
Q_{km}^{sp}	Specified reactive power flow from node *k* to node *m*.

P_{km}^{sp}	Specified active power flow from node *k* to node *m*.
$x^{\max}$	Maximum permissible value of *x*.
$x^{\min}$	Minimum permissible value of *x*.
$0 \le \boldsymbol{x} \perp \boldsymbol{y} \ge 0$	Complementarity condition between vectors ***x*** and ***y***.
$\boldsymbol{x}^{\mathrm{T}}$	Transpose of ***x***.
$\hat{\boldsymbol{x}}$	Estimates of ***x***.
$\boldsymbol{x}^{k}$	Vector of ***x*** obtained in the *k*-th iteration.
$\Delta\boldsymbol{x}$	Increments of ***x***.
x_i	The *i*-th element of vector ***x***.
$\mathcal{N}_{AC}$	The complete set of AC nodes.
$\mathcal{N}_{AC}^{P}$	The subset *P* of the AC nodes.
$\boldsymbol{z}$	Complete set of measurements.
$\boldsymbol{\varepsilon}$	Vector of uncorrelated noise errors in measurements.
$\boldsymbol{r}$	Vector of measurements' residuals.
$\sigma_{(\cdot)}$	Standard deviation of the measurement type $(\cdot)$
$\boldsymbol{h}(\cdot)$	Vector of functions that are the mathematical representation of ***z*** evaluated in $(\cdot)$.
$\boldsymbol{H}(\cdot)$	Jacobian matrix of $\boldsymbol{h}(\cdot)$ evaluated in $(\cdot)$.
$\boldsymbol{c}(\cdot)$	Vector of equality constraints functions evaluated in $(\cdot)$.
$\boldsymbol{C}(\cdot)$	Jacobian matrix of $\boldsymbol{c}(\cdot)$ evaluated in $(\cdot)$.
$\boldsymbol{R}$	Covariance matrix of Measurements.
$\boldsymbol{W}$	Weighting matrix of Measurements.
$\boldsymbol{S}$	Residuals sensitivity matrix.
$\boldsymbol{\Omega}$	Residuals covariance matrix.
$\boldsymbol{\mu}$	Vector of Lagrange multipliers from Hachtel's residuals constraints.
$\boldsymbol{\lambda}$	Vector of Lagrange multipliers from Hachtel's equality constraints.
α	Filter's tuning parameter in proposed bad data analysis.

β	Times of standard deviation in a measurement's error
Th	Threshold parameter for bad data analysis.
Th_{se}	Threshold of second filter in proposed bad data analysis.
SBD	Set of index numbers of measurements suspected as bad data.
IBD	Set of index numbers of measurements identified as bad data.
$\chi^2_{k,a}$	Chi squares value for k degrees of freedom and significance a.
PS_i	Projection statistics of the i-th measurement.

List of Publications

Published Papers in Journals

- **Martínez-Parrales, R.**, and Fuerte-Esquivel C. R. "A new unified approach for the state estimation and bad data analysis of electric power transmission systems with multi-terminal VSC-based HVDC networks." ***Electric Power Systems Research*** 160 (2018): 251-260.

Cited by

- Jung, S. H., & Huh, J. H. (2019). A Novel on Transmission Line Tower Big Data Analysis Model Using Altered K-means and ADQL. Sustainability, 11(13), 3499.
- Chitsazan, M. A. (2019). Grid Power Quality with FACTS Devices and Renewable Energy Sources Using Deep Learning Algorithms (Doctoral dissertation).
- Chitsazan M.A., Fadali M.S. & Trzynadlowski M.A. (2019) State Estimation for Large-Scale Power Systems and FACTS Devices Based on Spanning Tree Maximum Exponential Absolute Value. IEEE Transactions on Power Systems, Early Access.

Published Papers in Conferences

- **Martínez-Parrales, R.**, and Fuerte-Esquivel C. R. "Noise Estimation in Measurements to Improve the State Estimation of Electric Power Systems." ***2019 16th International Conference on Electrical Engineering, Computing Science and Automatic Control*** (CCE), Mexico City, Mexico, September 11-13, 2019.

Papers under review in Journals

- **Martínez-Parrales, R.**, C. R. Fuerte-Esquivel and Alcaide-Moreno Boris A. "Numerical Assessment of the WLS-Based State Estimation Performance and Residual-Based Bad Data Analyses under Non-Gaussian Measurement Noise" submitted to ***Electric Power Systems Research***, June 14, 2019.

- **Martínez-Parrales, R.**, C. R. Fuerte-Esquivel and Alcaide-Moreno Boris A. "Static State Estimation with Inequality Constraints in a Complementarity Framework" submitted to ***IEEE Transactions on Power Systems***, August 11, 2019.

Chapter 1

1 Introduction

1.1 Introduction

The evolution of electrical power transmission systems into larger interconnected networks includes the challenge of the integration of renewable power plants located offshore through the voltage source converter-based (VSC) high-voltage direct current (HVDC) technology, which is one of the most feasible solutions for the efficient grid integration of these types of power plants. In this context, point-to-point HVDC systems have advanced in the direction of multi-terminal VSC-HVDC (VSC-MTDC) systems, with the North Sea Super DC Grid being the clearest example of this kind of system development [Orths *et al*. 2012]. In this specific case, the VSC-MTDC system will be used for interconnecting several offshore wind farms, offshore loads and the onshore power grids. On the other hand, since the VSC enables a fast and independent control of the active and reactive powers at its alternating current (AC) terminals, as well as the reversal of the power flow direction without changing the DC line's polarity, VSC-MTDC systems can be used to interconnect independent AC transmission systems and to provide balancing services between these AC networks.

1.2 State of the art

1.2.1 Power flow in multi-terminal AC-DC systems

In order to fully quantify the way in which a VSC-based DC transmission grid can improve the flexible operation of multi-terminal AC-DC systems, it is necessary to develop suitable VSC mathematical models considering both the converter's control characteristics and its operational limits. In this context, there have been different proposals focused on the steady state aspects of such mathematical modeling and its suitable implementation for power flow, optimal power flow and state estimation studies. Among these proposals, however, very few consider VSC-MTDC systems along with their control modes and operational limits in a unified framework of analysis.

Each converter station composing a VSC-based HVDC link has been modeled by an AC controllable voltage source behind a complex impedance, with the interaction of both converters via the common DC link represented by an active power flow constraint [Angeles-Camacho *et al*. 2003]. This generic model was implemented in the formulations of the power flow [Angeles-Camacho *et al*. 2003], [Zhang 2004] and optimal power flow (OPF) [Pizano-Martinez *et al*. 2007] problems, respectively, in such a way that the magnitude and phase angle of those controllable voltage sources were combined with the nodal network state variables for a simultaneous iterative solution. This type of formulation is referred to as the unified solution approach. The modulation of the complex voltage source within its operating limits allows to meet the operation control mode specified for the converter station. Contrary to [Angeles-Camacho *et al*. 2003] and [Pizano-Martinez *et al*. 2007] where the DC system is not accessible, the MTDC network is explicitly represented in [Zhang 2004].

The generic model reported in [Angeles-Camacho *et al*. 2003] is also used in [Beerten *et al*. 2012] to sequentially solve the AC and DC power flow equations associated with an AC electric network containing VSC-MTDC systems. All AC-DC converters embedded in the MTDC network can be operating in either PQ- or PV-control mode, except the one referred to as the DC slack converter. The former control mode is set to accomplish constant active and reactive power injections into the AC grid, while the objective of the latter control mode is to attain a constant active power injection and a constant AC voltage magnitude at the system node. On the other hand, the DC slack converter operates under a QVdc-control mode in which its active power is modulated to attain a constant DC voltage. Furthermore, the amount of reactive power injected into the network is set to a fixed value. These control modes permit the decoupling and sequential solution of the AC and DC systems by representing the converter stations as constant power injection models. The feasible operation of each converter is assessed by checking its power limits at the system node, which are expressed in terms of the converter current and voltage limits. Following the same definitions of converter control modes reported in [Beerten *et al*. 2012], as well as the converter representation by a controllable voltage source behind an impedance [Angeles-Camacho *et al*. 2003], a unified approach for the power flow problem of multi-frequency AC systems interconnected by VSC-DC links is proposed in [Nguyen *et al*. 2019]. The VSC limits are expressed in terms of constraints of voltage and power at the converter AC terminal, which are checked during the iterative solution process.

Since the controllable voltage at the converter AC side can be expressed in terms of its DC side voltage and its modulation index, the DC-AC power conversion is explicitly represented by an ideal complex tap-changing transformer in [Acha *et al*. 2013]. The inverter modulation index is used to control its AC voltage magnitude, while the phase angles of the transformers' complex taps are used to control the active power flowing through the VSCs. Lastly, the VSC capacity to inject or withdraw reactive power from the AC grid is represented by a controllable shunt susceptance embedded at the converter's AC terminal. This VSC model is used to represent back-to-back and point-to-point VSC-HVDC links. This proposal is extended in [Acha & Castro 2016] to represent a MTDC ring.

1.2.2 State estimation in multi-terminal AC-DC systems

Because of the advantages of using VSC-MTDC systems in some specific cases, power systems application tools must be upgraded to estimate the operating state of AC-DC transmission systems, as well as to conduct system-wide studies. The state estimation (SE) is one of the most fundamental applications for efficiently operating and controlling electric power systems at both transmission and distribution levels. In contrast to the number of publications addressing the SE of power systems with VSC-HVDC links, however, very few papers have actually focused on mathematical formulations to estimate operating states of grids containing VSC-MTDC links.

The weighted least squares (WLS) method is employed in [de la Villa Jaén *et al*. 2008] to estimate the operating state of power systems containing both the back-to-back and the point-to-point VSC-HVDC links, where their operational constraints are treated as zero power injections, referred to as pseudo-measurements. In this case, only the voltage and current on the DC side of one of the converters comprising the HVDC link are included in the set of AC state variables to be estimated. A WLS-based state estimator that considers phasor measurement units (PMUs) and point-to-point VSC-HVDC links is detailed in [Zamora-Cárdenas *et al*. 2016]. In this proposal, the AC-DC interface is represented by an ideal controllable AC voltage source. Furthermore, the DC link operation is modeled by an active power balance constraint expressed as a function of powers on the converters' AC sides and losses through the DC link. This constraint is included as a pseudo-measurement in the formulation. Furthermore, because of the way in which the VSC-HVDC link is modeled, only AC nodal voltage magnitudes and phase angles are considered in the set of estimated state variables. On the other hand, a proposal to integrate a VSC-MTDC model into a WLS-based estimator is reported in [Cao *et al*. 2012]. In this case, the VSC-based AC-DC interface considers the converter's AC side as a controlled AC voltage source, while the DC side is modeled as a controllable current source [Cao *et al*. 2012]. Hence, the power flow equations at both converter terminals are completely decoupled because they are only expressed in terms of their corresponding AC or DC variables. Moreover, the DC network is only composed of transmission lines linking converters terminals so that the number of DC buses is also the number of converters. Finally, the state vector is augmented by including the voltages at both terminals of the AC-DC interface.

A PMU-only state estimation algorithm that considers classic HVDC links is proposed [Li & Vanfretti 2015]. The formulation avoids using active and reactive power equations and depends on the knowledge of the control mode operation and control targets of the HVDC link. The state variables of HVDC links and the AC grid are estimated simultaneously by using the WLS algorithm, with the AC-DC interface represented by means of the voltage and current phasors at the points of common coupling (PCC) of DC links. In [Qifeng *et al*. 2000], a sequential WLS-based SE approach is presented where the AC grid and classic MTDC links are decoupled and solved independently using SCADA measurements. In [Donde *et al*. 2016], a decentralized SE is proposed where the AC and VSC-MTDC grids are solved independently by using the concept of overlapped buses and SCADA measurements. In this case, the PCC buses are duplicated and appear in both networks such that the information in these buses is iteratively exchanged during the sequential SE solution process. The VSC-MTDC grid consists of HVDC links between converters and converterless DC buses. The estimated variables correspond to the DC voltages, converter transformer tap positions and complex voltages at the PCC buses.

1.2.3 Bad data analysis

The secure and economic operation of a power system requires an accurate assessment of its operating state, which is achieved by means of the state estimation (SE) process. Among the large diversity of proposals to solve the state estimation problem, the most common solution approaches adopted in practice are based on the weighted least squares (WLS) method. Since this method does not possess any robust features to recognize the presence of measurements with gross errors, a post-processing technique needs to be applied for the detection, identification and removal/correction of bad data to ensure an accurate estimation of the system state. On the other hand, least absolute value (LAV)-based estimators have the inherent ability to automatically discard gross errors present in measurements, as long as these measurements are not associated with leverage points [Kotiuga & Vidyasagar 1982] [Gol & Abur 2014]. Even though the solution provided by these robust state estimators is not affected by the existence of bad data [Mili *et al*. 1996] [Zhao & Mili 2018], none of these estimators are used in today's control centers [Abur & Lin 2018].

From a global perspective, the WLS-based estimators currently used in control centers must have a computationally efficient post-processing technique for the analysis of erroneous data, which allows a fast and reliable estimation of large-scale power systems containing a large volume of erroneous measurements. The largest normalized residual test (LNRT) still remains as the most frequently used concept for bad data processing [Abur & Lin 2018].

Very recently, an approach has been proposed for a highly efficient bad data analysis within the framework of the WLS-based estimators [Abur & Lin 2018]. In this proposal, the suspected measurements with gross errors are classified into groups based on their interacting sensitivities [Abur & Lin 2018]. Lastly, the bad data analysis is performed at the end of the state estimation.

A general assumption underlying the power system state estimators used in practice is that the measurement errors are independent Gaussian random variables. It has been recently reported, however, that measurement errors associated with phasor measurement units (PMUs) are unlikely to follow a Gaussian distribution [Wang *et al*. 2017] [Zhou *et al*. 2014]. Furthermore, processed SCADA measurements by multifunction meters may deviate their noise statistics' errors from Gaussian distributions [Zhao & Mili 2018]. In this sense, it would be desirable to obtain the probability distribution associated with each measurement error to mathematically formulate a generalized state estimation approach, but it is not practical for real power systems with thousands of measurements and a large communications infrastructure. In these operation conditions, however, it is possible to quantify how the state estimation is affected when the solution is obtained by estimators that consider correlated non-Gaussian measurement errors as if they were Gaussian and statistically independent. Note that this is what really happens with the state estimators used in today's control centers.

1.2.4 Inequality constrained state estimation

In order to provide reliable state estimates, a large number of theoretical developments and practical improvements have been proposed to solve the state estimation problem since its introduction by Schweppe in the late 1960s [Abur & Exposito 2004]. However, very few papers have been published on mathematical formulations of the static SE problem with inequality constraints [Clements *et al.* 1995] [Abur & Celik 1993] [Singh *et al.* 1997] [Rakpenthai *et al.* 2006], where the limits of electric components may be directly checked during the estimation process. In practice, actual operating conditions can violate the operational limits of some electric components, which is permissible for a given period of time. Hence, the operational limits cannot be enforced by the state estimator because the result will be biased with respect to the "true" power system state. Because of the physical limitations of the electrical components or specific control actions, however, some algebraic state variables are subject to inequality constraints to avoid the state estimates not making physical sense or not being physically possible. For example, the estimated state of the power system might indicate that some electric components are operating out of their physical limits if the states were estimated in the presence of undetectable gross errors in measurements. This could lead to the unnecessary activation of remedial control actions that steer the power system to a normal operating condition. In this same context, in the Mexican interconnected power system it is "common" to have telemetry errors in remote terminal units. If the SCADA system detects these errors, they are eliminated and replaced by pseudo-measurements taken from a database, which may not correspond to the actual operating state. If this is the case, the estimated values of the electrical variables may also indicate that some electric components are operating beyond their physical limits.

Based on the information mentioned above, the application of the proposal described in this thesis has focused on incorporating inequality constraints representing physical limits of electric power components in the SE formulation. The use of inequality constraints also helps to make an unobservable part of the system observable and improves the redundancy of measurements in local parts of the network [Abur & Celik 1993], [Monticelli 2000].

The inequality constraints are mathematically included in a state estimator by formulating a constrained optimization problem, which can be solved by using different mathematical optimization methods. A logarithmic barrier function method is used in [Clements *et al.* 1995] to solve a constrained least square problem considering VAr limits in generators. The incorporation of inequality constraints in a least absolute value (LAV) state estimator is reported in [Abur & Celik 1993], which is formulated as a sequence of linear programming problems solved by a simplex method. The proposal is successfully applied to enforce power flows through tie lines connecting two systems. This type of inequality constraint is also included in a weighted LAV-based state estimator in [Singh *et al.* 1997]. The solution is obtained by formulating a dual WLAV optimization problem solved through applying an interior point method. In this formulation, the inequality constraints are converted to equality constraints by using exact penalty functions. A constrained nonlinear WLAV optimization problem is formulated in [Rakpenthai *et al.* 2006] to enforce the physical constraints of the unified power flow controller. The optimization problem is solved with a primal-dual interior point method, where the inequality constraints are converted to equality constraints by adding nonnegative slack variables. The nonnegative value of these variables is ensured by adding logarithmic barrier functions to the problem objective function.

Even though most of the proposals centers on WLAV-based estimators, which can automatically reject bad measurements as long as these are not leverage points [Singh *et al.* 1997], these estimators are not typically installed in today's control centers [Lin & Abur 2018]. Hence, the WLS-based state estimators currently used in control centers must have a computationally efficient technique to include inequality constraints, which allows a fast and a reliable estimation of large-scale power systems.

1.2.5 Nodal frequency estimation

The estimation of the system frequency has been of great interest in recent years because the increasing integration of unconventional renewable-based generators, as well as the low frequency power oscillation between control areas. A method called frequency divider is presented in [Milano & Ortega 2017], where the frequency at each system's node can be computed from a set of frequency measurements by using an extended admittance matrix that includes the machines' internal impedances. In [Golpîra & Messina 2018], a center of gravity approach based on the center of inertia (COI) is presented, where dependencies of bus frequencies with respect to the COI are derived to calculate the local frequency deviations based on the deviation of the COI. An estimation of the frequency of the COI based on the frequency divider is presented in [Milano F. 2018], where only the information about the machines' inertia constants and internal reactances are needed.

An analytical method for computing the voltage and frequency oscillations based on a linearized power system model is presented in [Vanfretti 2009], where the sensitivities of bus frequencies are computed by filtering the voltage phase angles. This filter is connected in series to the linearized model of the system by considering the machine internal angles and the angular velocities as state variables. Furthermore, the modal analysis is used to obtain the voltage and frequency variations when a particular mode of oscillation is excited.

1.3 Justification

While the conventional power systems rely heavily on bulk generation by synchronous machines, future power systems will be comprised of a large-scale integration of renewable generation that is usually interfaced to the network through power electronic devices. The integration of this type of generation will decrease the total system inertia that adversely affect frequency and voltage stability. Hence, it is necessary to update the system operation tools to consider these types of electric components, as well as their control modes and operational limits.

The correct estimation of the system state is of paramount importance to maintain the system in a normal operating state through the correct control actions made during real-time operation.

The state estimation accuracy needs to be enhanced by means of better bad data detection/identification or by the application of constraints to the estimation problem.

Lastly, one of the main objectives in the operation of electric power systems is to maintain a near real-time equilibrium between load power and generation power. The effectiveness of this control action, however, will depend on the accuracy with which the system-wide frequency is measured. Hence, the knowledge of the frequency in every node of the system is highly desirable since this type of information allows the system operators to detect other types of problems and improve the control decisions.

1.4 Objective

The main objective of this work is the formulation and implementation of a power flow and a static state estimation approaches suitable for the analysis of large-scale multi-terminal VSC-based AC-DC power systems considering renewable energy sources.

In order to achieve this objective, the following goals must be accomplished:

- The set of nonlinear equations that reflects the steady state operation of the VSC must be derived from first principles to be applied for both power flows and state estimation studies.
- To apply the complementarity optimization theory for directly including the inequality constraints in the formulation of the power flow and state estimation problems.
- To perform the derivation and implementation of an iteratively multiple bad data analysis approach suitable for large-scale systems and non-Gaussian measurement errors.
- To derive a mathematical formulation suitable for the estimation of nodal frequencies based on the concept of tracking state estimation.

1.5 Main contributions

The main contribution of this thesis are as follows.

- A new VSC model is derived from first principles, where the VSC operational limits are represented in the complementary framework.

- A new and comprehensive model for the doubly-fed induction generator and for the permanent magnet synchronous generator is developed starting from the VSC model and considering different control modes of operation.
- In the context of multi-terminal AC-DC transmission grids, the power flow approaches reported in the literature were found insufficient, and in this thesis a new unified approach to the power flow problem is presented. This proposal simultaneously solves the state variables of the AC and DC networks with the state variables associated with the wind generators and VSCs in a single frame of reference.
- A static state estimation approach suitable for electric power transmission systems containing fully controlled multi-terminal high voltage direct current networks is proposed. VSC-MTDC grids are directly integrated in a Hachtel-based SE algorithm that considers both SCADA and PMU measurements. The VSC-MTDC network is not restricted to transmission lines connecting VSCs such that different voltage levels of transmission lines can be considered in the DC network.
- A new practical bad data analysis is proposed, in which multiple bad data are detected, identified and corrected within the iterative solution of the estimation process. Hence, the original level of measurement redundancy is maintained unaltered during the state estimation study.
- The question of what effect non-Gaussian data have on the outcome of state estimators and of bad data analyses used in power system control centers is answered in this thesis. The suitability of applying the proposed bad data analysis together with a WLS-based state estimator, which is the one currently used in control centers, to obtain accurate estimates when the error distribution of measurements is not truly Gaussian has been demonstrated by numerical examples.
- A new approach to incorporate inequality constraints into the equality constrained weighted least squares state estimator, without modifying the way in which this estimator is formulated and solved, is reported.
- Finally, a methodology to estimate the nodal frequency based on the results of the SE in the context of systems containing phasor measurements units (PMU) is presented.

1.6 Methodology

This thesis mainly focuses on the modeling and analysis of multi-terminal AC-DC transmission grids where different tools have been developed in this line: power flows, state estimation and frequency tracking. Since the state estimation studies require a set of measurements to be performed, the power flow study is used to define the state of a system from where a set of perfect measurements is obtained. In the context, a power flow approach suitable for fully controlled multi-terminal AC-DC transmission grids is formulated and implemented. By the application of this tool, the set of measurements were obtained to perform the static state estimation studies.

On the other hand, VSC-MTDC grids are directly integrated in a Hachtel-based SE algorithm that considers both SCADA and PMU measurements. A set of equality constraints is used to represent the operational restrictions associated with the VSC model adopted in this thesis. Note that these constraints are directly taken into account in the problem formulation instead of by using virtual measurements with high weighting factors. Lastly, the estimation is carried out in a unified manner where the state variables associated with the DC grid and the converter stations are simultaneously estimated together with the AC nodal voltages. Those state variables correspond to the nodal voltages at the DC grid, the duty cycles of the DC-DC converters, the modulation index and phase angle of each VSC, as well as the tap ratio of the transformer connecting the converter station to the AC grid.

In the context of state estimation bad data analysis, two proposals have been implemented where one is applied during the iterative solution process [Martínez-Parrales & Fuerte-Esquivel 2018] and the other is applied as a post-estimation process. Based on these proposals, the suitability of applying the WLS-based state estimator and residual-based bad data analyses to estimate the operation status of power systems under non-Gaussian noise conditions is numerically assessed. The numerical results are compared with the ones obtained by using robust state estimators. Furthermore, it is statistically demonstrated under different non-Gaussian noises that the proposed bad data analysis approach based on the largest normalized estimated residual test (LNERT) [Martínez-Parrales & Fuerte-Esquivel 2018] can be successfully applied for detecting, identifying and correcting/eliminating multiple measurements with non-Gaussian gross errors. It is also shown that the use of the LNERT provides better results that the ones obtained by using the largest normalized residual test (LNRT). Lastly, since multiple uncorrelated bad data are simultaneously corrected or eliminated, depending on how these measurements are handled in the bad data analysis, it is shown that the LNERT approach [Martínez-Parrales & Fuerte-Esquivel 2018] drastically reduces the computation time required to estimate the operation state of large-scale power systems.

The proposal to consider inequality constraints in the WLS-based SE problem is formulated and implemented by using the concept of complementarity constraints. The application of this concept permits representing physical limits as complementarity constraints, which are in turn directly included as equality constraints in a constrained WLS-based state estimator by using the Fischer-Burmeister merit function [Fischer 1992]. Hence, the traditional methods used to solve the equality constrained estimation problem remain unaltered in their mathematical formulation. In this context, this proposal uses Hachtel's augmented matrix method to solve the SE problem, where the equality constraints representing physical limits are directly added to the set of constraints originally considered in the primal problem formulation.

Lastly, a methodology to estimate the nodal frequency based on the results of two consecutives PMU-based SEs is presented. When the system is not observable by PMUs only and SCADA measurements are necessary for observability, the time between SCADA samples may be too long to estimate the frequencies with the time derivative of the voltage angles' estimates, so an alternative methodology is presented using three consecutive SE results. Finally, an application is presented to detect interarea oscillations based on the frequency estimates derived from the SE results on where no detailed information of the machines, such as dynamic parameters or internal reactances, is needed.

1.7 Thesis outline

Apart from the information mentioned above, the proposals of this research are detailed in the rest of this thesis, which is structured as follows.

Chapter 2 details the proposed VSC model where the DC and AC terminals of the converter are represented as state variables and the advantages of this new model over previous models are highlighted. Furthermore, the steady state operation of the VSC is explained in the context of the new model's state variables, and the power flow equations are presented based on these characteristics. The application of the new model in the context of power flow studies is also detailed in this chapter.

Chapter 3 contains the proposed formulation of the multi-terminal AC-DC state estimation. Moreover, the proposed bad data analysis is duly presented with a detailed explanation of each filtering step of its process and a flowchart of the algorithm. On the other hand, the proposed modeling of the inequality constraints and their inclusion as equality constraints, derived from the reformulation of the nonlinear complementary problem, in the Hachtel augmented matrix method is also detailed in this chapter.

Chapter 4 presents numerical examples of state estimation studies based on the contributions detailed in Chapter 3.

Chapter 5 details the proposed nodal frequency estimation formulation, where the formulation of a tracking state estimator and the way that different types of measurements are handled is presented. Numerical examples to show the performance of the proposed frequency estimator versus the frequency divider method are also reported.

Chapter 6 gives the general conclusions about all the proposals presented in this work based on the numerical achievements obtained with the numerical examples. Moreover, future work derived from the presented work is proposed.

Chapter 2

2 Multi-terminal AC-DC Power Flow

2.1 Introduction

This chapter focuses on the power flow (PF) solution of voltage source converter (VSC) based multi-terminal AC-DC power electric transmission systems. Under this subject, three main contributions are presented. First, a new VSC model where the nodal voltages of the AC and the DC terminals of the converters are represented as state variables together with the converters modulation index and firing angle. Secondly, the complementary constraints method is applied to convert the VSC operational limits into equality constraints to be further integrated into the power flow (PF) formulation. These constraints are associated with the VSC inner current control, the modulation index limits and the DC terminal voltage limits. Finally, a PF unified formulation is proposed to solve multi-terminal AC-DC transmission grids.

2.2 Voltage source converter-based multi-terminal AC-DC systems

The voltage source converter-based high voltage direct current technology is one of the most feasible solutions to integrate a large amount of renewable energy to alternating current transmission grids, while ensuring the operational security of the electric power system. Direct current transmission links have advanced in the direction of multi-terminal VSC-HVDC (VSC-MTDC) systems, with the North Sea Super DC Grid as a clear example of this kind of development [Orths *et al*. 2012].

Unlike the current source converter-based technology, the VSC technology improves the flexibility of operation through a fast and independent control of active and reactive powers. Furthermore, the power flow direction can be reversed without changing the DC line voltage's polarity. VSC-MTDC systems can also be used to interconnect asynchronous AC transmission systems and to provide balancing services between these AC networks.

2.3 Voltage source converter model

The derivation of the mathematical model representing the VSC steady state operation is based on the converter schematic representation shown in Fig. 2.1a, and Fig. 2.1b. The differences with respect to the model reported in [Acha & Castro 2016] are as follows: i) The *ac* terminals of the VSC are explicitly modeled to separate its corresponding power flow equations from the power flow equations in the reactor/filter. This facilitates the inclusion of the converter operational constraints. ii) The equivalent susceptance is changed for a reactive power source Q_{vsc} in order to constrain the reactive power limits of this source. This correctly represents the VSC inner current limits. Lastly, iii) no internal inductance is considered in the VSC, i.e., only the resistance R_1 is modeled to represent the conductance losses associated with the conducting resistance of the IGBT´s, while the switching losses are represented by the conductance G_{sw}.

The VSC operation is modeled through two decision variables, named modulation index m_a and firing angle ϕ, which permit representing the VSC independent control of the magnitude and angle of $\bar{\boldsymbol{V}}_{\boldsymbol{ac}}$, respectively. Note that $\bar{\boldsymbol{V}}_{\boldsymbol{ac}}$ represents the positive sequence equivalent of the three-phase voltage at the converter's *ac* side. Note also that the voltage angle θ_{ac} of $\bar{\boldsymbol{V}}_{\boldsymbol{ac}}$ is defined by the VSC fire angle $\theta_{ac} = \phi$.

2.4 Voltage source converter power equations

Based on the VSC equivalent circuit representation given in Fig. 2.1, the power flow equations associated with the proposed VSC based AC-DC station model are the following:

$$P_{dcac} = V_{dc}{}^2\left(G_{sw} + K^2 m_a{}^2 R_1^{-1}\right) - K m_a V_{dc} V_{ac} R_1^{-1}\cos\left(\phi - \theta_{ac}\right) \ , \tag{2.1}$$

$$Q_{dcac} = -K m_a V_{dc} V_{ac} R_1^{-1}\sin\left(\phi - \theta_{ac}\right), \tag{2.2}$$

$$P_{acdc} = R_1^{-1} V_{ac}^2 - K m_a V_{dc} V_{ac} R_1^{-1}\cos\left(\theta_{ac} - \phi\right) \ , \tag{2.3}$$

$$Q_{acdc} = -K m_a V_{dc} V_{ac} R_1^{-1}\sin\left(\theta_{ac} - \phi\right), \tag{2.4}$$

$$P_{viac} = G_{kk} V_{vi}{}^2 + V_{vi} V_{ac}\left(G_{km}\cos\left(\theta_{vi} - \theta_{ac}\right) + B_{km}\sin\left(\theta_{vi} - \theta_{ac}\right)\right) \ , \tag{2.5}$$

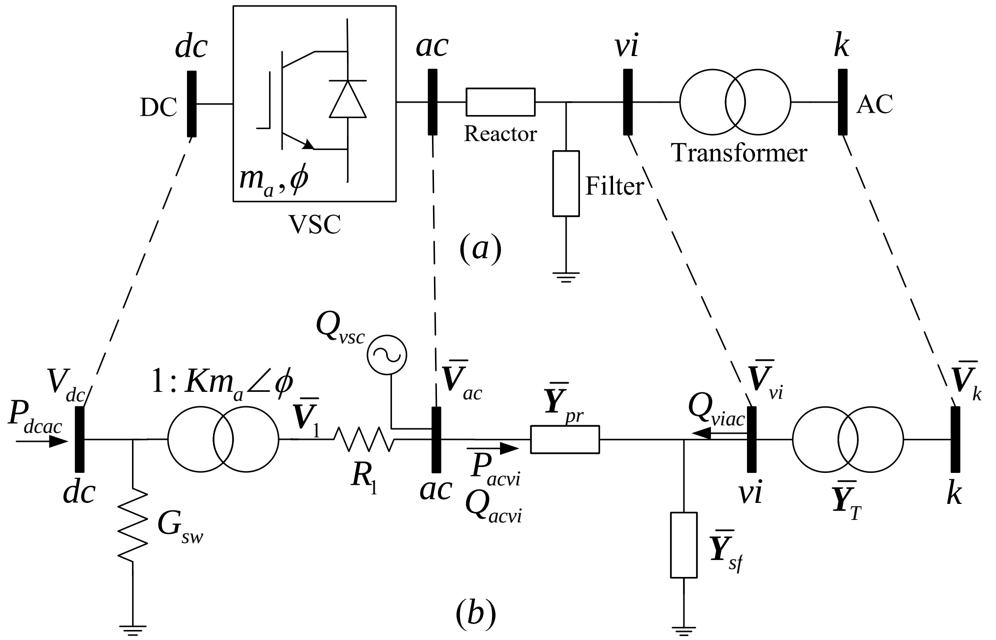

Fig. 2.1 AC-DC converter station and transformer. (a) Schematic representation. (b) Positive sequence equivalent circuit model.

$$Q_{viac} = -B_{kk}V_{vi}^{\,2} + V_{vi}V_{ac}\left(G_{km}\sin\left(\theta_{vi}-\theta_{ac}\right) - B_{km}\cos\left(\theta_{vi}-\theta_{ac}\right)\right) , \tag{2.6}$$

$$P_{acvi} = G_{mm}V_{ac}^{\,2} + V_{ac}V_{vi}\left(G_{mk}\cos\left(\theta_{ac}-\theta_{vi}\right) + B_{mk}\sin\left(\theta_{ac}-\theta_{vi}\right)\right) , \tag{2.7}$$

$$Q_{acvi} = -B_{mm}V_{ac}^{\,2} + V_{ac}V_{vi}\left(G_{mk}\sin\left(\theta_{ac}-\theta_{vi}\right) - B_{mk}\cos\left(\theta_{ac}-\theta_{vi}\right)\right) , \tag{2.8}$$

where G_{kk} and B_{kk} are the equivalent conductance and susceptance of $\bar{\boldsymbol{Y}}_{sf} + \bar{\boldsymbol{Y}}_{pr}$, respectively. Similarly, G_{mm} and B_{mm} denote the conductance and susceptance of $\bar{\boldsymbol{Y}}_{pr}$, respectively. In this case, $G_{km} = G_{mk} = -G_{mm}$ and $B_{km} = B_{mk} = -B_{mm}$. The value of $K = \sqrt{3/2}$ for a two-level, three-phase VSC and R_1 represent the conductance losses associated with the conducting resistance of the IGBT′s. Lastly, since $\theta_{ac} = \phi$ at the power flow solution, $Q_{dcac} = Q_{acdc} = 0$.

2.5 Voltage source converter control modes of operation

Fig. 2.2 shows the set of measurements that can be taken in the VSC. In this case, the voltage measurement at the *vi* node together with a phase-loop locked (PLL) on phase A, as well as the measurement of the current flowing from nodes *vi* to *ac*, provide the information associated with the active/reactive powers P_{acvi} / Q_{acvi} flowing from nodes *vi* to *ac*. On the other hand, the

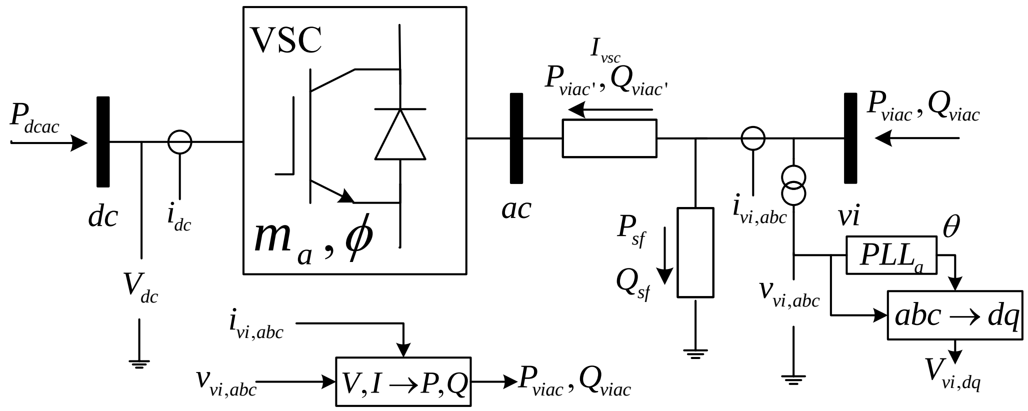

Fig. 2.2 VSC´s control measurements.

dc node voltage measurement and the current's measurement from *dc* to *ac* nodes gives the information required to control the active power P_{dcac} flowing from the *dc* to *ac* nodes.

Based on the information mentioned above and considering the reactor/filter characteristics, the voltage amplitude at the *ac* node can be modulated through the modulation index m_a to achieve the following control actions: i) to maintain the voltage magnitude *vi* to a given setpoint V_{vi}^{sp} by injecting or extracting the necessary reactive power or ii) to keep the reactive power flowing from *vi* to *ac* nodes at an specified value Q_{viac}^{sp}.

On the other hand, the adjustment of the firing angle ϕ permits controlling the voltage angle on the *ac* node with respect to the *vi* voltage angle to achieve one of the following control actions: i) to transfer an specified amount of active power P_{dcac}^{sp} through the converter; ii) to keep the *dc* node voltage at a given value V_{dc}^{sp} by injecting or extracting the necessary active power to maintain the DC grid's power balance and the capacitor charge such that this node becomes the DC grid slack; or iii) to become the AC grid slack transferring the necessary amount of active power to give balance to the AC grid.

The two possible control modes associated with modulation index m_a and the three control modes that can be achieved with the firing angle ϕ provide six possible control combinations for the VSC as shown in Fig. 2.3: $V_{vi}^{sp}\text{-}P_{dcac}^{sp}$, $..\text{-}P_{dcac}^{sp}$, $V_{vi}^{sp}\text{-}V_{dc}^{sp}$, $Q_{viac}^{sp}\text{-}V_{dc}^{sp}$, $V_{vi}^{sp}\text{-}AC_{slack}$ and $Q_{viac}^{sp}\text{-}AC_{slack}$ control modes. Note that when a VSC provides frequency regulation support, a

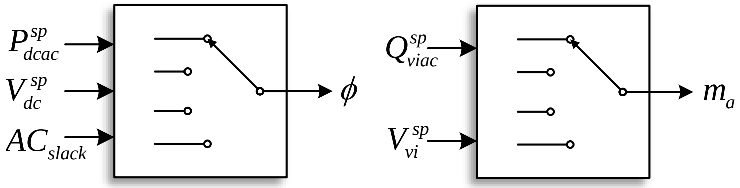

Fig. 2.3 VSC control modes.

MW/Hz relation is defined in such a way that the converter will increase the active power injection to the AC network when the frequency must be increased by a defined amount of Hz and *vice versa*. In this context, the converter must be operating in a P_{dcac}^{sp} control.

2.6 Voltage source converter limits

To guarantee that the power flow solution corresponds to a feasible VSC steady state operation, three limiting factors must be considered in the formulation: i) the upper and lower DC capacitor charge limits; ii) the modulation index operational range associated with the modulation technique and the filter size; and iii) the maximum continuous current that the converter's switching elements can handle [Haileselassie 2012]. The first two operating limits are considered by the inequality constraints $V_{dc}^{\min} \le V_{dc} \le V_{dc}^{\max}$ and $m_a^{\min} \le m_a \le m_a^{\max}$, while the maximum continous current $I_{vsc}^{\max}$ is used together with V_{ac} to obtain the maximum apparent power $S_{acvi}^{\max}$ at which the converter can operate. In this case, $S_{acvi}^{\max}$ is decomposed to obtain the lower and upper limits $Q_{vsc}^{\min} \le Q_{vsc} \le Q_{vsc}^{\max}$ and $P_{dcac}^{\min} \le P_{dcac} \le P_{dcac}^{\max}$ based on the inner current limiter technique .

The current control scheme applied to the VSC is shown in Fig. 2.4. The converter's outer control defines the desired direct $I_{vsc,d}^{des}$ and quadrature $I_{vsc,q}^{des}$ current components based on the active and reactive power requirements respectively, to achive the control setpoint. After this, a current limiter receives the desired current components and applies a technique to avoid the converter's overcurrent by defining both currents references. Finally, the inner current control receives these current references and defines the modulation index m_a and the firing angle ϕ. Details of how these controllers dinamically operate are out of the scope of this work but can be found at [Yazdani & Iravani 2010] [Haileselassie 2012] [Arrillaga *et al*. 2007].

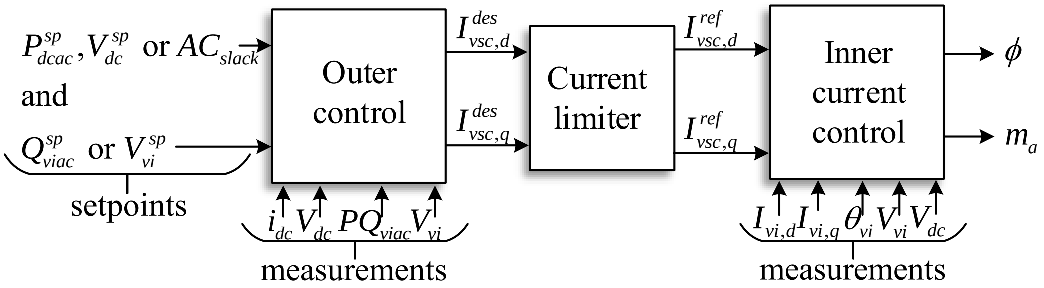

Fig. 2.4 Current control scheme.

The current limiter technique can be in a vector form as detailed in [Vrana *et al*. 2013], where if the desired current magnitude exceeds the VSC continuous current capacity, the direct and quadrature components are scaled down in the same proportion to maintain the converter's current within the limit, as shown in Fig. 2.5a.

Another type of current limiter technique gives priority to the current's direct component over the quadrature component, which in turn translates into a priority of active power [Haileselassie 2012]. In this case, if the desired current magnitude exceeds the current limit, the direct component is limited to a given percent value of the maximum current, e.g. 95%, and the quadrature component is then limited to the rest of the converter's current capacity, as shown in Fig. 2.5b.

By considering a voltage invariant transformation, the active power $P_{viac'}$ shown in Fig. 2.2 is defined as the active power flowing from node *vi* to node *ac* minus the active power P_{sf} flowing through the filter. Similarly, the reactive power $Q_{viac'}$ is defined as the reactive power flowing from node *vi* to node *ac* minus the reactive power Q_{sf} flowing through the filter.

In this case, the active power is mathematically defined by $P_{viac'} = 1.5 V_{vi,d} I_{vsc,d}$, where $V_{vi,d}$ is the direct component of the *vi* bus voltage and $I_{vsc,d}$ is the VSC direct current component. On the other hand, the reactive power $Q_{viac'}$ is mathematically defined by $Q_{viac'} = -1.5 V_{vi,d} I_{vsc,q}$ where $I_{vsc,q}$ is the VSC quadrature current component.

Based on this transformation of coordinates, the desired current components are calculated at each *k*-th iteration of the power flow solution process as

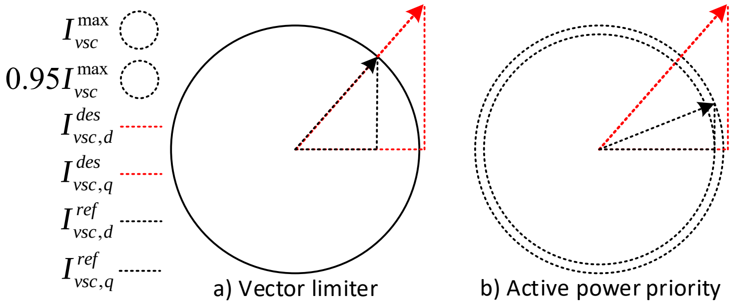

Fig. 2.5 Current limiter techniques.

$$I_{vsc,d}^{des\ \ k} = P_{viac'}{}^{k} / 1.5 V_{vi,d}{}^{k} \tag{2.9}$$

$$I_{vsc,q}^{des\ \ k} = -Q_{viac'}{}^{k} / 1.5 V_{vi,d}{}^{k} \quad . \tag{2.10}$$

For sake of simplicity, the upper index k is removed under the assumption that the magnitudes of all currents are calculated at each Newton-Raphson (NR) iteration.

When a limiter technique is applied and $I_{vsc}^{des} > I_{vsc}^{\max}$, the desired current of the VSC is constrained to $I_{vsc}^{des} = 1.5\sqrt{\left(I_{vsc,d}^{des}\right)^2 + \left(I_{vsc,q}^{des}\right)^2}$. In the case of the current vector limiter, the *dq* current components are scaled down as

$$I_{vsc,d}^{ref} = I_{vsc,d}^{des}\left(I_{vsc}^{\max} / I_{vsc}^{des}\right) \tag{2.11}$$

$$I_{vsc,q}^{ref} = I_{vsc,q}^{des}\left(I_{vsc}^{\max} / I_{vsc}^{des}\right) \quad . \tag{2.12}$$

If the active power is a priority over the reactive power, $I_{vsc,d}^{des}$ is limited to $I_{vsc,d}^{PF} = P.F.\left(I_{vsc}^{\max} / 1.5\right)$, where *P.F.* is the minimum power factor that can be achieved when the direct component is in its maximum value: $I_{vsc,d}^{ref} = \min(I_{vsc,d}^{des}, I_{vsc,d}^{PF})$. The quadrature component $I_{vsc,q}^{des}$ is also limited to $I_{vsc,q}^{\max} = \sqrt{\left(I_{vsc}^{\max} / 1.5\right)^2 - \left(I_{vsc,d}^{ref}\right)^2}$: $I_{vsc,q}^{ref} = \min(I_{vsc,q}^{\max}, I_{vsc,q}^{des})$.

After applying a current limiter technique, the maximum and minimum values of $P_{viac'}$ are computed as $P_{viac'}^{\max} = 1.5 V_{vi,d} I_{vsc,d}^{ref}$ and $P_{viac'}^{\min} = -1.5 V_{vi,d} I_{vsc,d}^{ref}$, respectively. Furthermore, $P_{acvi}^{\max} = -P_{viac'}^{\min}$ and $P_{acvi}^{\min} = -P_{viac'}^{\max}$ because the reactor resistance is neglected. Note that the maximum current I_{acvi} is the converter´s current limit $I_{vsc}^{\max}$.

On the other hand, the converter's reactive power limits are computed by

$$Q_{vsc}^{\max} = Q_{acvi}^{\max} = \sqrt{\left(V_{ac} I_{vsc}^{\max}\right)^2 - \left(P_{acvi}^{\max}\right)^2} \; , \tag{2.13}$$

$$Q_{vsc}^{\min} = Q_{acvi}^{\min} = -\sqrt{\left(V_{ac} I_{vsc}^{\max}\right)^2 - \left(P_{acvi}^{\max}\right)^2} \; . \tag{2.14}$$

Lastly, the converter losses P_{loss} are computed as the difference between P_{dcac} and P_{acvi} such that the limits of the active power entering the *dc* node are given by

$$P_{dcac}^{\max} = P_{loss} + P_{acvi}^{\max} \, , \tag{2.15}$$

$$P_{dcac}^{\min} = P_{loss} + P_{acvi}^{\min} \; . \tag{2.16}$$

2.7 Voltage source converter-based wind generator models

The VSC model proposed in Sections 2.3 to 2.6 can be used to represent the back-to-back converters composing the doubly-fed induction generator (DFIG) and the permanent magnet synchronous generator (PMSG). This new representation ensures that the power flow solution corresponds to a feasible steady state operation of the VSC.

2.7.1 Doubly-fed induction generator

In the DFIG, the mechanical power P_m is obtained from the rotating windmill, which is connected to the generator's rotor with a gearbox to transfer the mechanical torque and to increase the rotational speed. The generator's stator directly injects the active power P_s to the AC grid, and its electromagnetic field is rotating at the grid´s angular speed. The rotor is connected to a rotor-side converter (RSC) via a slip ring transferring the P_{rsc} power. The RSC is connected back-to-back to a grid side converter (GSC), which transfers the P_{gsc} power into the AC grid via a transformer, as shown in Fig. 2.6.

The slip s relates the stator angular speed ω_s, the rotor angular speed ω_r and the pole pairs p [Li S. 2013]:

$$s = \frac{\omega_s - p\omega_r}{\omega_s} \; . \tag{2.17}$$

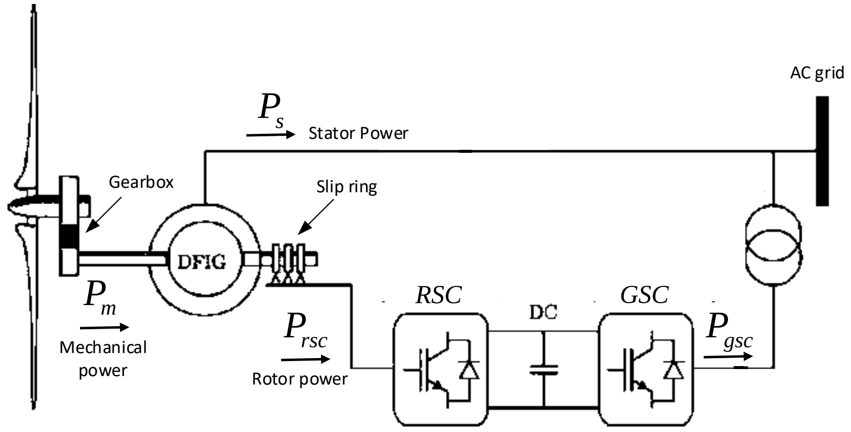

Fig. 2.6 Schematic representation of a DFIG

This slip has a positive value when the rotor is rotating at subsynchronous speed and a negative value when the rotor is going at supersynchronous speed. Moreover, the slip value defines how the mechanical power P_m is partitioned into the stator power P_s and the RSC power P_{rsc} by

$$P_s = \left(\frac{1}{1-s}\right) P_m , \tag{2.18}$$

$$P_{rsc} = \left(\frac{-s}{1-s}\right) P_m . \tag{2.19}$$

The blades' angular velocity ω_w is related to the rotor's angular velocity ω_r through the gearbox ratio η, where ω_r depends on the slip according to (2.17):

$$\omega_w = \frac{\omega_r}{\eta} = \frac{\omega_s}{p\eta}(1-\mathrm{s}) . \tag{2.20}$$

The tip speed ratio λ is related to the slip by

$$\lambda = \frac{r\omega_w}{v} = \frac{r\omega_s}{vp\eta}(1-\mathrm{s}) , \tag{2.21}$$

where *r* is the blade's length, also known as radius, and *v* is the wind speed.

The electrical equivalent circuit relating the rotor and stator circuits through the slip is shown in Fig. 2.7 [Fletcher & Yang 2010] [Li S. 2013], where $\bar{\boldsymbol{V}}_r$ and $\bar{\boldsymbol{V}}_s$ are the rotor and stator

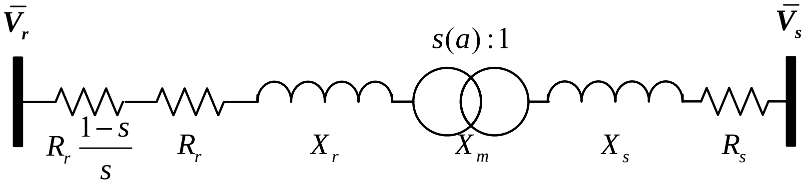

Fig. 2.7 Rotor to stator circuit.

voltages, respectively. The circuit elements R_r and X_r represent the rotor's resistance and reactance while R_s and X_s represent the stator's resistance and reactance. Note that the rotor and stator circuits are connected through a transformer with a magnetizing reactance X_m and with a turn ratio that depends on the slip [Fletcher & Yang 2010].

The per-unit equivalent model of the stator to the AC grid connection [Li S. 2013] adopted in this work is presented in Fig. 2.8.

On the other hand, and different from other proposals, the DFIG's back-to-back converters are represented using the constrained VSC model presented in Section 2.3. The complete DFIG's positive sequence representation proposed in this work is presented in Fig. 2.9. Note that the DC capacitor is not explicitly considered in this model because the power flow problem is formulated in the steady state time frame: the DC capacitor dynamics are neglected.

In order to formulate the mathematical model of the DFIG, the stator power equations are defined by [Li S. 2013]:

$$P_s = \frac{-sR_rV_m^2 + V_mV_r\left[R_r\cos\left(\theta_m-\theta_r\right) - sX_r\sin\left(\theta_m-\theta_r\right)\right]}{R_r^2+s^2X_r^2}, \tag{2.22}$$

$$Q_s = \frac{-s^2X_rV_m^2 + V_mV_r\left[sX_r\cos\left(\theta_m-\theta_r\right) + R_r\sin\left(\theta_m-\theta_r\right)\right]}{R_r^2+s^2X_r^2}. \tag{2.23}$$

The active power P_{rsc} injected in node vi_{rsc} is obtained by subtracting the stator power to the mechanical power $P_{rsc} = P_m - P_s$, where the mechanical power is obtained from

$$P_m = \frac{1}{2P_{base}}\rho A v^3 C_p, \tag{2.24}$$

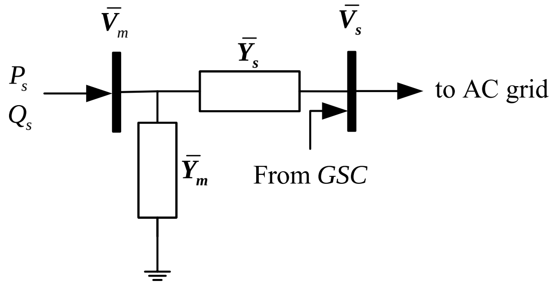

Fig. 2.8. Stator to AC grid connection.

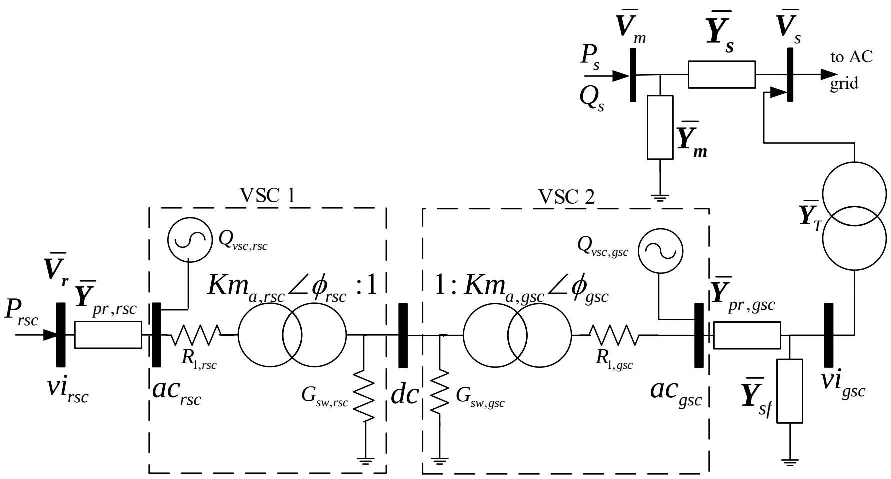

Fig. 2.9 Positive sequence representation of DFIG.

where ρ, A, C_p, v and P_{base} denote the air density, the sweep area, the power utilization coefficient, the air speed and the system base power, respectively:

On the other hand, the power utilization coefficient C_p is computed by

$$C_p = \left(c_1 \frac{c_2}{\gamma} - c_3\beta - c_4\beta^{c_5} - c_6 \right) e^{-\frac{c_7}{\gamma}}, \quad \gamma = \left(\frac{1}{\lambda + c_8\beta} - \frac{c_9}{\beta^3 + 1} \right)^{-1}, \tag{2.25}$$

where the constants $c_1 ... c_9$ correspond to the generator coefficients, the pitch angle is denoted by β, while γ is an intermediate variable that depends on the tip speed ratio λ that in turns depends on the slip value.

Lastly, the slip value is solved as a state variable, and the power flow solution is restricted to (2.18), where P_m and P_s has derivatives w.r.t the slip value. The DFIG's RSC is operating under the Q_{viac}^{sp} - AC_{slack} control mode, while the GSC operates under either the Q_{viac}^{sp}-V_{dc}^{sp} or the V_{vi}^{sp}-V_{dc}^{sp} control mode.

2.7.2 Permanent magnet synchronous generator

The schematic representation of the PMSG is depicted in Fig. 2.10, and the proposed positive sequence representation is shown in Fig. 2.11.

The active power P_m entering the vi_{msc} node is calculated with (2.24), where the power utilization coefficient C_p is given with (2.25), but the tip speed ratio λ is obtained by

$$\lambda = \frac{r\omega_w}{v} \ . \tag{2.26}$$

2.8 Nonlinear complementarity problem

Two vectors $\boldsymbol{x}$ and $\boldsymbol{y}$ of dimension N_{dv} satisfy the complementarity condition if they are orthogonal and each of their components are nonnegative: $0 \le \boldsymbol{x} \perp \boldsymbol{y} \ge 0$ [Leyffer 2002]. In the context of optimization theory, each of those components is either a decision variable or a function of the decision variables [Billups & Murty 2000], and at least one element of the complementarity dyad $(x_i, y_i)\ \forall\, i = 1,\ldots,N_{dv}$ should be equal to 0 at the optimal solution. Hence, the most basic nonlinear complementarity problem (NCP) consists of finding two vectors of decision variables $\boldsymbol{x} \in \mathbb{R}^{N_{dv}}$ and $\boldsymbol{y} \in \mathbb{R}^{N_{dv}}$ that satisfy the set of equations [Leyffer 2002]:

$$\boldsymbol{x} \ge \boldsymbol{0}, \quad \boldsymbol{y} \ge \boldsymbol{0}, \quad \boldsymbol{x}^{\mathrm{T}}\boldsymbol{y} = 0 \ . \tag{2.27}$$

Since $\boldsymbol{x}^{\mathrm{T}}\boldsymbol{y} = \sum_{i=1}^{N_{dv}} x_i y_i = 0$ and at least one element of the complementarity dyad (x_i, y_i) must be 0, this can be equivalently stated that

$$x_i \ge 0, \quad y_i \ge 0, \quad x_i y_i = 0 \quad i = 1,\ldots,N_{dv}. \tag{2.28}$$

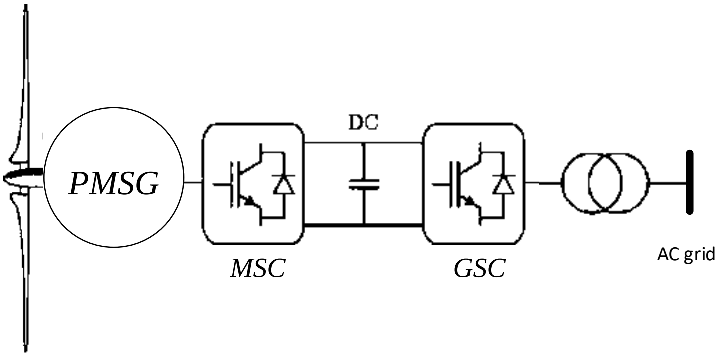

Fig. 2.10 Schematic representation of a PMSG.

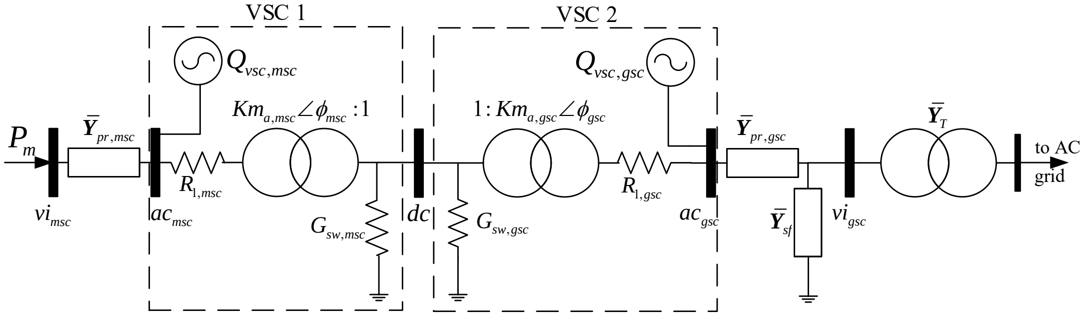

Fig. 2.11 Positive sequence representation of a PMSG.

Similarly, the NCP can be formulated in terms of decision variables $\boldsymbol{x} \in \mathbb{R}^{N_{dv}}$ and functions of the decision variables $\boldsymbol{F}(\boldsymbol{x}) : \mathbb{R}^{N_{dv}} \to \mathbb{R}^{N_{dv}}$. In this case, the vector of decision variables $\boldsymbol{x}$ satisfies the set of equations (2.29) at the solution:

$$\boldsymbol{x} \geq \boldsymbol{0}, \quad \boldsymbol{F}(\boldsymbol{x}) \geq \boldsymbol{0}, \quad \boldsymbol{x}^{\mathrm{T}}\boldsymbol{F}(\boldsymbol{x}) = 0 . \tag{2.29}$$

Since $\boldsymbol{x}^{\mathrm{T}}\boldsymbol{F}(\boldsymbol{x}) = \sum_{i=1}^{N_{dv}} x_i F_i(\boldsymbol{x}) = 0$ subject to the fact that the value of x_i and/or $F_i(\boldsymbol{x})$ must be 0, (2.29), it can be equivalently expressed as

$$x_i \geq 0, \quad F_i(\boldsymbol{x}) \geq 0, \quad x_i F_i(\boldsymbol{x}) = 0 \quad i = 1, \ldots, N_{dv} . \tag{2.30}$$

2.8.1 Reformulation of the nonlinear complementarity problem

One way of reformulating the NCP is based on the fact that the *i*-th complementarity conditions $\{x_i \geq 0, y_i \geq 0, \, x_i y_i = 0\}_{i=1}^{N_{dv}}$ or $\{x_i \geq 0, F_i(\boldsymbol{x}) \geq 0, \, x_i F_i(\boldsymbol{x}) = 0\}_{i=1}^{N_{dv}}$ may be expressed in terms of an NCP function $\varphi_i : \mathbb{R}^2 \to \mathbb{R}$, also referred to as a merit function, such that $\varphi_i(x_i, y_i) = 0$ or $\varphi_i(x_i, F_i(\boldsymbol{x})) = 0$, respectively [Fischer 1992], [Leyffer 2002]. Among the different NCP functions proposed to perform this transformation [Leyffer 2002], the used in power system applications is the Fischer-Burmeister merit function (FBMF) [Diaz & Gonzalez-Moran 2012], [Sundaresh & Rao 2014], [Sandoval-Perez 2015], [Tapia-Juarez *et al.* 2018]:

$$\varphi_i\left(x_i, y_i\right) = \sqrt{x_i^2 + y_i^2} - x_i - y_i = 0 \tag{2.31}$$

or

$$\varphi_i\left(x_i, F_i(\boldsymbol{x})\right) = \sqrt{x_i^2 + F_i(\boldsymbol{x})^2} - x_i - F_i(\boldsymbol{x}) = 0\,. \tag{2.32}$$

Since this reformulation transforms a complementarity problem into a set of nonlinear equations, the optimization problem can be solved by Newton-based methods. A successful application of this transformation into the formulation of the Newton-based power flow problem is associated with the modeling of generators' reactive power limits [Diaz & Gonzalez-Moran 2012], [Sundaresh & Rao 2014], the operational limits of FACTS controllers and wind generators [Sandoval-Perez 2015], as well as different operation control modes of photovoltaic generators [Tapia-Juarez *et al.* 2018]. This idea is extended in this work for automatically checking the physical limits during the iterative solution process of the AC-DC power flow and AC-DC state estimation problems.

2.8.2 Inequality constraints model

In the specific case of the complementary condition between a variable x_i^{cc} and a function $F_i(\boldsymbol{x})$, the corresponding equality constraint derived from the FBMF is

$$\sqrt{\left(F_i(\boldsymbol{x})\right)^2 + \left(x_i^{cc}\right)^2} - F_i(\boldsymbol{x}) - x_i^{cc} = 0, \quad \boldsymbol{x}^{cc} \subset \boldsymbol{x}\,. \tag{2.33}$$

When a variable x or a function of the variables $g(\boldsymbol{x})$ must be constrained to a lower or an upper limit, i.e. $x^{\min} \le x \le x^{\max}$ or $g^{\min} \le g(\boldsymbol{x}) \le g^{\max}$, each inequality can be transformed to an equality constraint by using (2.33) with an auxiliary variable x_i^{cc}. In this context, $F_i(\boldsymbol{x})$ is given by $F_i(\boldsymbol{x}) = x - x^{\min}$ or $F_i(\boldsymbol{x}) = g(\boldsymbol{x}) - g^{\min}$, for the lower limits; otherwise, $F_i(\boldsymbol{x}) = x^{\max} - x$ or $F_i(\boldsymbol{x}) = g^{\max} - g(\boldsymbol{x})$, for the upper limits.

2.8.3 Complementarity-based generator limits

When a generator is connected to a PV node *i*, the *i*-th node voltage magnitude V_i is regulated to a specified value V_i^{sp} by injecting or withdrawing the necessary amount of reactive power. This regulation is subject to the generator's reactive power capability, which can be represented by [Sandoval-Perez 2015]:

$$Q_{Gen}^{\min} \le Q_{Gen} \le Q_{Gen}^{\max} \ , \tag{2.34}$$

where $Q_{Gen} = g^{Gen}(\boldsymbol{x})$. The complementarity conditions of these constraints are given by

$$\begin{aligned} &0 \le \left(Q_{Gen} - Q_{Gen}^{\min}\right) \perp x^{cc,Gen-} \ge 0 \\ &0 \le \left(Q_{Gen}^{\max} - Q_{Gen}\right) \perp x^{cc,Gen+} \ge 0 \end{aligned} , \tag{2.35}$$

while the FBMF-based equality constraints are given by

$$\begin{aligned} &\sqrt{\left(Q_{Gen} - Q_{Gen}^{\min}\right)^2 + \left(x^{cc,Gen-}\right)^2} - \left(Q_{Gen} - Q_{Gen}^{\min}\right) - x^{cc,Gen-} = 0 \\ &\sqrt{\left(Q_{Gen}^{\max} - Q_{Gen}\right)^2 + \left(x^{cc,Gen+}\right)^2} - \left(Q_{Gen}^{\max} - Q_{Gen}\right) - x^{cc,Gen+} = 0 \end{aligned} . \tag{2.36}$$

The *i*-th node voltage magnitude is then solved as a state variable, i.e., $V_i \subset \boldsymbol{x}$, subject to the constraint [Sandoval-Perez 2015]:

$$V_i = V_i^{sp} + x^{cc,Gen-} - x^{cc,Gen+} . \tag{2.37}$$

When the generator reaches its $Q_{Gen}^{\max}$, the auxiliary variables have the values $x^{cc,Gen+} \ge 0, x^{cc,Gen-} = 0$ and $V_i \le V_i^{sp}$. On the other hand, when the generator reaches its $Q_{Gen}^{\min}$, the auxiliary variables have the values $x^{cc,Gen-} \ge 0, x^{cc,Gen+} = 0$ and $V_i \ge V_i^{sp}$.

2.8.4 Complementarity-based voltage source converter limits

In this proposal, the operating state of each VSC is constrained to $m_a^{\min} \le m_a \le m_a^{\max}$ and $Q_{vsc}^{\min} \le Q_{vsc} \le Q_{vsc}^{\max}$. On the other hand, all VSCs using the fire angle for controlling the active power P_{dcac}^{sp} are also constrained to satisfy $V_{dc}^{\min} \le V_{dc} \le V_{dc}^{\max}$ and $P_{dcac}^{\min} \le P_{dcac} \le P_{dcac}^{\max}$.

Lastly, the VSCs working under the V_{dc}^{sp} or AC_{slack} control contribute the necessary amount of active power to the DC or AC grid, respectively, in order to achieve the specified control. Hence, the operation of these converters is not constrained by either $P_{dcac}^{\min} \le P_{dcac} \le P_{dcac}^{\max}$ nor $V_{dc}^{\min} \le V_{dc} \le V_{dc}^{\max}$; otherwise, these constraints could be the reason for no convergence during the iterative solution process.

The complementarity conditions associated with the VSC modulation index $m_a \subset \boldsymbol{x}$ are expressed by

$$\begin{aligned} 0 \le \left(m_a - m_a^{\min}\right) \perp x^{cc,ma-} \ge 0 \\ 0 \le \left(m_a^{\max} - m_a\right) \perp x^{cc,ma+} \ge 0 \end{aligned}, \tag{2.38}$$

while the FBMF equivalent transformations are given by

$$\begin{aligned} \sqrt{\left(m_a - m_a^{\min}\right)^2 + \left(x^{cc,ma-}\right)^2} - \left(m_a - m_a^{\min}\right) - x^{cc,ma-} = 0 \\ \sqrt{\left(m_a^{\max} - m_a\right)^2 + \left(x^{cc,ma+}\right)^2} - \left(m_a^{\max} - m_a\right) - x^{cc,ma+} = 0 \end{aligned}. \tag{2.39}$$

A similar line of reasoning is applied to $Q_{vsc} \subset \boldsymbol{x}$ subject to the complementarity conditions $0 \le \left(Q_{vsc} - Q_{vsc}^{\min}\right) \perp x^{cc,Qvsc-} \ge 0$ and $0 \le \left(Q_{vsc}^{\max} - Q_{vsc}\right) \perp x^{cc,Qvsc+} \ge 0$ while $V_{dc} \subset \boldsymbol{x}$ is subject to $0 \le \left(V_{dc} - V_{dc}^{\min}\right) \perp x^{cc,Vdc-} \ge 0$ and $0 \le \left(V_{dc}^{\max} - V_{dc}\right) \perp x^{cc,Vdc+} \ge 0$.

Lastly, for $P_{dcac} = g^{Pdcac}(\boldsymbol{x})$, the complementarity conditions are:

$$\begin{aligned} 0 \le \left(P_{dcac} - P_{dcac}^{\min}\right) \perp x^{cc,Pdcac-} \ge 0, \\ 0 \le \left(P_{dcac}^{\max} - P_{dcac}\right) \perp x^{cc,Pdcac+} \ge 0. \end{aligned} \tag{2.40}$$

When the VSC′s modulation index is used to achieve the V_{vi}^{sp} control, the *vi* voltage's magnitude is solved as a state variable in the power flow formulation, i.e., $V_{vi} \subset \boldsymbol{x}$, and this voltage is subject to the constraint

$$V_{vi} = V_{vi}^{sp} + x^{cc,ma-} - x^{cc,ma+} + x^{cc,Qvsc-} - x^{cc,Qvsc+}. \tag{2.41}$$

When $m_a = m_a^{\max}$, the values of V_{ac} and Q_{vsc} are indirectly limited to their corresponding upper values. In this case, $x^{cc,ma-}$, $x^{cc,Qvsc-}$ and $x^{cc,Qvsc+}$ will be zero such that $V_{vi} \le V_{vi}^{sp}$. In the case where $m_a = m_a^{\min}$, the values of V_{ac} and Q_{vsc} are indirectly limited to their corresponding lower values such that $x^{cc,ma+}$ $x^{cc,Qvsc-}$ and $x^{cc,Qvsc+}$ will be 0, while $V_{vi} \ge V_{vi}^{sp}$. On the other hand, when $Q_{vsc} = Q_{vsc}^{\max}$, the auxiliary variables $x^{cc,Qvsc-}$, $x^{cc,ma-}$ and $x^{cc,ma+}$ are equal to 0, which results in a value of $V_{vi} \le V_{vi}^{sp}$. When $Q_{vsc} = Q_{vsc}^{\min}$, the auxiliary variables $x^{cc,Qvsc+}$, $x^{cc,ma-}$ and $x^{cc,ma+}$ are equal to 0, which results in a value of $V_{vi} \ge V_{vi}^{sp}$.

A similar line of reasoning is applied if the VSC´s modulation index is used to control the reactive power Q_{viac}^{sp}, but instead of using (2.41) the power flow problem is subject to

$$-Q_{viac} = -Q_{viac}^{sp} + x^{cc,ma-} - x^{cc,ma+} + x^{cc,Qvsc-} - x^{cc,Qvsc+}. \tag{2.42}$$

On the other hand, if the active power P_{dcac}^{sp} is being controlled by modulating the VSC firing angle, the power flow problem is constrained by

$$P_{dcac} = P_{dcac}^{sp} + x^{cc,Vdc+} - x^{cc,Vdc-} + x^{cc,Pdcac-} - x^{cc,Pdcac+}. \tag{2.43}$$

The active power P_{dcac}, which is injected from the DC grid to the VSC, is decreased or increased when the converter's *dc* voltage is, increased or decreased, respectively, with respect to the DC voltage at those nodes directly connected to the VSC. In this sense, if $V_{dc} = V_{dc}^{\max}$ or $V_{dc} = V_{dc}^{\min}$, the active power P_{dcac} will be indirectly limited to its lower or upper value respectively. In the case where $V_{dc} = V_{dc}^{\max}$, the values of the auxiliary variables $x^{cc,Vdc-}$, $x^{cc,Pdcac-}$ and $x^{cc,Pdcac+}$ will be 0, while the value of P_{dcac} is $P_{dcac} \ge P_{dcac}^{sp}$. When $V_{dc} = V_{dc}^{\min}$, the values of the auxiliary variables $x^{cc,Vdc+}$, $x^{cc,Pdcac-}$ and $x^{cc,Pdcac+}$ will be 0 and $P_{dcac} \le P_{dcac}^{sp}$.

On the other hand, if $P_{dcac} = P_{dcac}^{\max}$, the null auxiliary variables are $x^{cc,Pdcac-}$, $x^{cc,Vdc-}$ and $x^{cc,Vdc+}$, while $P_{dcac} \le P_{dcac}^{sp}$. In the case where $P_{dcac} = P_{dcac}^{\min}$, the null auxiliary variables are $x^{cc,Pdcac+}$, $x^{cc,Vdc-}$ and $x^{cc,Vdc+}$, while $P_{dcac} \ge P_{dcac}^{sp}$.

Lastly, when the firing angle is used to control the state variable V_{dc}^{sp} at a given setpoint, (2.43) is replaced by

$$V_{dc} = V_{dc}^{sp} \ , \tag{2.44}$$

when the firing angle is used to become the AC_{slack}, (2.43) is replaced by

$$\phi = 0 \ . \tag{2.45}$$

When the VSC is operating under a V_{dc}^{sp} control and violates its current capability during the power flow solution, other VSCs must modify their corresponding P_{dcac}^{sp} value. Droop control techniques can be applied to achieve this hierarchical control, but it is out of the scope of this thesis. A similar reasoning applies when one VSC is operating under the AC_{slack} control, where the setpoints of the AC grid's active powers must be modified if the VSC exceeds its current capability.

2.9 Multi-terminal AC-DC power flow problem

The generalized power flow model for a multi-terminal AC-DC system can be categorized in AC grids and DC grids. The following notation will be used to indicate the type of nodes:

$\mathcal{N}_{AC}$ The complete set of AC nodes;

$\mathcal{N}_{DC}$ The complete set of DC nodes;

$\mathcal{N}_{AC}^{PQ}$ The set of nodes without the synchronous generator's voltage regulation, except the *ac* nodes of AC-DC converter stations;

$\mathcal{N}_{AC}^{P}$ The set of nodes with the synchronous generator's voltage regulation, except the slack node;

$\mathcal{N}_{AC}^{S}$ The set of slack nodes;

$\mathcal{N}_{AC}^{ac}$ The set of *ac* nodes of AC-DC converter stations;

$\mathcal{N}_{DC}^{dc}$ The set of *dc* nodes of AC-DC converter stations;

$\mathcal{N}_{DC}^{P}$ The complete set of DC nodes, except the *dc* nodes of AC-DC converter stations;

2.9.1 AC grids

In these types of grids, all the voltage's magnitudes and angles are solved as state variables, i.e. $V_i \subset \boldsymbol{x},\ \ \theta_i \subset \boldsymbol{x},\ \ \forall i \in \mathcal{N}_{AC}$. Depending on the type of node, a couple of constraints will be defined for each node.

The active and reactive power mismatch equations ΔP_i, ΔQ_i are applied to all the nodes without the synchronous generator's voltage regulation except to the AC-DC converter station *ac* nodes:

$$\Delta P_i = P_i^{Gen} - P_i^{Load} - V_i \sum_{j \in \mathcal{N}_{AC}} V_j \left[G_{i,j} \cos\left(\theta_i - \theta_j\right) + B_{i,j} \sin\left(\theta_i - \theta_j\right) \right] = 0 \ \ \forall i \in \mathcal{N}_{AC}^{PQ}, \quad (2.46)$$

$$\Delta Q_i = Q_i^{Gen} - Q_i^{Load} - V_i \sum_{j \in \mathcal{N}_{AC}} V_j \left[G_{i,j} \sin\left(\theta_i - \theta_j\right) - B_{i,j} \cos\left(\theta_i - \theta_j\right) \right] = 0 \ \ \forall i \in \mathcal{N}_{AC}^{PQ}, \quad (2.47)$$

where P_i^{Gen} and Q_i^{Gen} are the active and reactive power generation in the *i*-th node, P_i^{Load} and Q_i^{Load} are the active and reactive power load in the *i*-th node. Furthermore, $G_{i,j}$ and $B_{i,j}$ are the conductance and susceptance respectively, between the *i*-th and *j*-th nodes.

The active power mismatch equation (2.46) is the only one considered for the nodes with the synchronous generator's voltage regulation, except the slack node, i.e., $\Delta P_i,\ \forall i \in \mathcal{N}_{AC}^{P}$. On the other hand, the reactive power mismatch equation is replaced by the constraint (2.37) $\forall i \in \mathcal{N}_{AC}^{P}$.

No power mismatch equations are considered for slack nodes such that the associated constraints are

$$\theta_i = \theta_i^{ref}, \forall i \in \mathcal{N}_{AC}^{S}, \quad (2.48)$$

$$V_i = V_i^{sp}, \forall i \in \mathcal{N}_{AC}^{S}. \quad (2.49)$$

Lastly, the associated constraints for the *ac* nodes of AC-DC converter stations are given by

$$P_{acdc} + P_{acvi} = 0, \quad (2.50)$$

$$Q_{vsc} = Q_{acvi}, \quad (2.51)$$

where P_{acdc}, P_{acvi} and Q_{acvi} are obtained according to (2.3), (2.7) and (2.8) respectively and $Q_{vsc} \subset \boldsymbol{x}$. The constraint associated with the fact that no reactive power flows from the *ac* node to the *dc* node, and used to solve Q_{vsc}, is:

$$\phi = \theta_{ac} . \tag{2.52}$$

2.9.2 DC grids

In these types of grids, all the nodal voltage's magnitudes are solved as state variables, i.e., $V_i \subset \boldsymbol{x},\ \forall i \in \mathcal{N}_{DC}$. Depending on the type of node, one constraint is defined as described below.

For all the DC grid nodes, excluding all *dc* nodes of AC-DC converter stations, the following DC-type power mismatch equation ΔP_i^{DC} is applied:

$$\Delta P_i^{DC} = V_i \sum_{j \in \mathcal{N}_{DC}} V_j G_{i,j} = 0 \quad \forall i \in \mathcal{N}_{DC}^{P} \ . \tag{2.53}$$

Lastly, an special kind of power mismatch is applied to the DC side of all AC-DC converter stations:

$$V_i \sum_{j \in \mathcal{N}_{DC}} V_j G_{i,j} + P_{dcac} = 0 \quad \forall i \in \mathcal{N}_{DC}^{dc} , \tag{2.54}$$

where P_{dcac} is computed according to (2.1).

2.9.3 Unified solution approach

The Newton Raphson's method is used to solve the nonlinear set of equations associated with the formulation of the AC-DC power flow problem:

$$\Delta \boldsymbol{x}^k = -\left(\boldsymbol{J}^k\right)^{-1} \boldsymbol{M}^k \ , \tag{2.55}$$

where $\Delta \boldsymbol{x}$ is the incremental vector for the state variables $\boldsymbol{x}$, $\boldsymbol{M}$ is the vector of constraints associated with the state variables, $\boldsymbol{J}$ is the Jacobian matrix composed of the derivatives of $\boldsymbol{M}$ with respect to $\boldsymbol{x}$ and k is the iteration number associated with the iterative solution process.

In this context, the vector of state variables is composed of $\boldsymbol{x} = \left[\boldsymbol{\theta}_{AC}, \boldsymbol{V}_{AC}, \boldsymbol{V}_{DC}, \boldsymbol{m}_a, \boldsymbol{\phi}, \boldsymbol{Q}_{vsc}, \boldsymbol{D}, \boldsymbol{s}, \boldsymbol{x}^{cc}\right]$, where the vectors $\boldsymbol{\theta}_{AC}$, $\boldsymbol{V}_{AC}$ and $\boldsymbol{V}_{DC}$ can be separated into subsets depending on the type of node defined in Section 2.9:

$$\begin{aligned} \boldsymbol{\theta}_{AC} &= \left[\boldsymbol{\theta}_{AC}^{PQ}, \boldsymbol{\theta}_{AC}^{P}, \boldsymbol{\theta}_{AC}^{S}, \boldsymbol{\theta}_{AC}^{ac}\right], \\ \boldsymbol{V}_{AC} &= \left[\boldsymbol{V}_{AC}^{PQ}, \boldsymbol{V}_{AC}^{P}, \boldsymbol{V}_{AC}^{S}, \boldsymbol{V}_{AC}^{ac}\right], \\ \boldsymbol{V}_{DC} &= \left[\boldsymbol{V}_{DC}^{P}, \boldsymbol{V}_{DC}^{dc}\right]. \end{aligned} \tag{2.56}$$

The duty cycle $\boldsymbol{D}$ of the DC-DC converters, connected between nodes *k* and *m*, is associated with their capacity to perform the control of the active power injected to node *m*: P_m^{sp} [Vrana *et al*. 2013]. In this case, the following constraint equation must be included in the power flow formulation, which is solved for $\boldsymbol{D}$:

$$P_{mk} = V_m^2 \left(2/R\right) - V_m V_k \left(2D/R\right) = -P_m^{sp} , \tag{2.57}$$

where *R* is the internal DC-DC converter's resistance.

Lastly, the existing relationship between the state variables and the corresponding equality constraint equation *M* is reported in Table 2.1, where the mismatch equations associated with the VSC modulation index and firing angle depends on the VSC control mode of operation.

2.9.4 Initialization of state variables

The initial values of the state variables used in the PF studies are defined as follows: i) The voltage magnitudes of the nodes with voltage regulation are initialized in the specified value, while the rest of the voltage magnitudes are initialized in 1 p.u. ii) The AC voltage angles are initialized in 0 radians except for the *ac* nodes of the VSC, which are determined by using (2.60). iii) The initial value of VSC modulation indexes are calculated from (2.58). Lastly, iv) the duty cycle of DC-DC converters is started in 1 p.u.

$$m_a^0 = \left| m_a \angle \phi^0 \right|, \tag{2.58}$$

$$m_a \angle \phi^0 = \frac{\bar{\boldsymbol{V}}_{vi}^0 + \left(\bar{\boldsymbol{Y}}_{pr}^{-1} + R_1\right)\left(\bar{\boldsymbol{Y}}_T\left(\bar{\boldsymbol{V}}_{vi}^0 - \bar{\boldsymbol{V}}_k^0\right) + \bar{\boldsymbol{V}}_{vi}^0 \bar{\boldsymbol{Y}}_{sf}\right)}{K V_{dc}^0}, \tag{2.59}$$

Table 2.1 Relation between state variables and constraint equations.

x	M equation	x	M equation
$\boldsymbol{\theta}_{AC}^{PQ}$	(2.46)	$\boldsymbol{V}_{AC}^{PQ}$	(2.47)
$\boldsymbol{\theta}_{AC}^{P}$	(2.46)	$\boldsymbol{V}_{AC}^{P}$	(2.37)
$\boldsymbol{\theta}_{AC}^{S}$	(2.48)	$\boldsymbol{V}_{AC}^{S}$	(2.49)
$\boldsymbol{\theta}_{AC}^{ac}$	(2.50)	$\boldsymbol{V}_{AC}^{ac}$	(2.51)
$\boldsymbol{V}_{DC}^{P}$	(2.53)	$\boldsymbol{V}_{DC}^{dc}$	(2.54)
$\boldsymbol{m}_a$	(2.41) or (2.42)	ϕ	(2.43), (2.44) or (2.45)
$\boldsymbol{Q}_{vsc}$	(2.52)	$\boldsymbol{D}$	(2.57)
$\boldsymbol{s}$	(2.18)	$\boldsymbol{x}^{cc}$	(2.33)

$$\theta_{ac}^{0} = \arctan\left(imag(m_a \angle \phi^{0}) / real(m_a \angle \phi^{0})\right) \, . \qquad (2.60)$$

2.10 Power flow case studies

The effectiveness of the proposed constrained PF is numerically demonstrated for three different operating scenarios of the CIGRE test system [Vrana *et al*. 2013] shown in Fig. 2.12.

The system is composed as follows: i) two onshore AC networks of 2 and 4 nodes, respectively, operating at 380 kV; ii) four offshore AC systems operating at 145 kV to connect wind farms; and iii) three VSC-HVDC systems corresponding to one point-to-point link at ±200 kV, another monopolar radial network with 5 nodes at ±200 kV, and iv) lastly a bipolar 8-node meshed grid at ±400 kV. There exist 11 VSC-based AC-DC interfaces, where 6 of them have a monopolar configuration, while the rest have a bipolar arrangement. Furthermore, there are two DC-DC converters supplying specific power, and one of them enables power exchange from the meshed grid to the radial network. Finally, the total number of nodes corresponds to 33 AC nodes and 15 nodes at the DC systems, where 4 of them have no connections to the AC system.

The system parameters are given in [Vrana *et al*. 2013], while those corresponding to the transformers, filters and reactors of the VSC-based AC-DC station model detailed in Section 2.3 are $\overline{\boldsymbol{Y}}_T = -j10000$, $\overline{\boldsymbol{Y}}_{sf} = j0.05$ and $\overline{\boldsymbol{Y}}_{pr} = -j1000$.

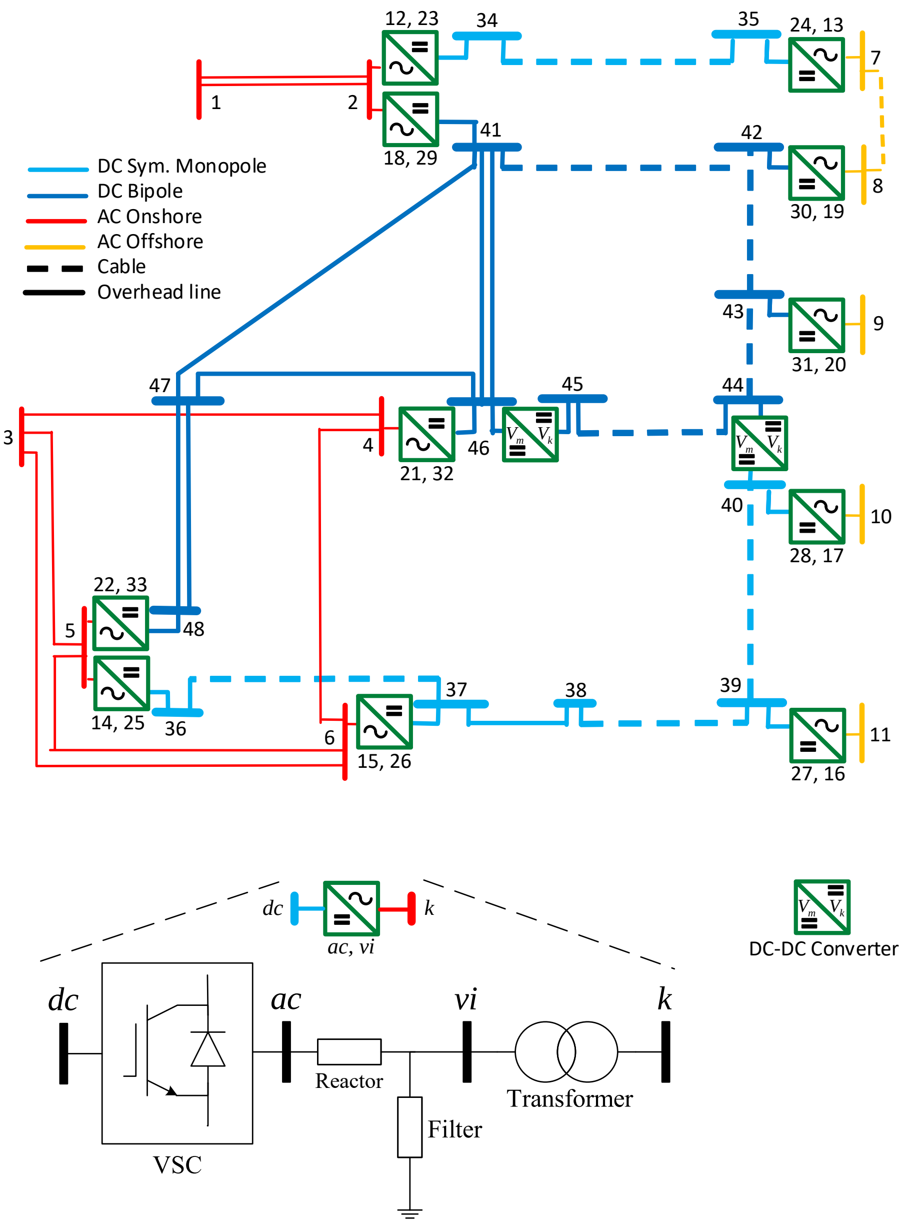

Fig. 2.12 CIGRE test system

2.10.1 Power flow base case

For the first PF scenario, the control modes and capacities of all VSC are the ones specified in [Vrana *et al*. 2013], the modulation indexes' allowable range for all converters is from 0.77 to 0.86, and the *dc* node voltage permissible range is defined from 0.95 to 1.05 p.u. In this scenario all converters are working within their operational limits, which means that the complementarity constraints are solved with all their auxiliary variables equal to 0.

The power flow solution converged in three iterations to a tolerance of 1x10^{-6} and in four iterations to a tolerance of 1x10^{-12}. A comparison of the results obtained with the proposed approach for the DC power flow with respect to the ones reported in [Vrana *et al*. 2013] shows that the maximum relative difference was 0.57%, which is attributed to the way in which the AC-DC converter is modeled.

The PF results for the AC-DC converter stations, the AC nodal voltages and the DC nodal voltages for the power flow base case are presented in Table 2.2, Table 2.3 and Table 2.4, respectively. All powers are expressed in MVA and voltage angles in degrees. All other values are given in p.u. The first three columns of Table 2.2 indicate the numbers associated with the internal nodes of each converter station, i.e., *dc*, *ac* and *vi* nodes, which are shown in the equivalent circuit of Fig. 2.1b. The nodal voltage angles are relative to the corresponding AC grid slack node angle reference. Since each independent AC network has its own slack node, a slack synchronous generator is connected at nodes 1 and 3, respectively. Furthermore, nodes 24, 27, 28 and 31 are the *ac* nodes of the corresponding AC-DC converters using their firing angles to achieve an AC_{slack} control mode. In this case, the voltage phase angle at these nodes become the angle reference to the AC grids connected to these converters. The P_{dcac} column in Table 2.2 indicates that four AC-DC converters connected to the *ac* nodes 26, 30, 32 and 33 are using their firing angles to achieve the P_{dcac}^{sp} control mode at 800 MW, -600 MW, 1500 MW and 1700 MW, respectively. Lastly, the AC-DC converters connected to the *dc* nodes 34, 36 and 41 are using their corresponding firing angles to achieve the V_{dc}^{sp} control mode at 1.00, 0.99 and 1.01 p.u. as indicated in Table 2.4.

Regarding the converter control modes achieved by adjusting the modulation index, the Q_{viac} column in Table 2.2 indicates that two AC-DC converters connected to the *vi* nodes 12 and 14, respectively, are using their modulation indexes to achieve a Q_{viac}^{sp} control mode at 0.0 MVAs, while the rest of the AC-DC converters are working under the V_{vi}^{sp} control mode to regulate the corresponding *vi* nodes voltage magnitudes at 1.0 p.u. as shown in Table 2.3.

Table 2.2. AC-DC converter stations results for power flow base case

dc	ac	vi	m_a	$\phi\,(deg)$	P_{dcac}	P_{acdc}	P_{loss}	Q_{viac}	Q_{kvi}	I_{vsc}
34	23	12	0.8202	-21.6963	384.7557	-382.1297	2.6260	0.0000	0.1461	3.8222
35	24	13	0.8048	0.0000	-389.2817	392.0188	2.7371	31.5566	31.7112	3.9372
36	25	14	0.8234	11.7353	-121.9047	122.8775	0.9728	0.0000	0.0151	1.2298
37	26	15	0.8328	6.2475	800.0000	-793.5844	6.4156	-18.2529	-17.6227	7.9370
39	27	16	0.8060	0.0000	-496.0640	500.0000	3.9360	-0.2500	0.0000	5.0002
40	28	17	0.8113	0.0000	100.7046	-100.0000	0.7046	-0.0100	0.0000	1.0012
41	29	18	0.8029	-23.2029	-1991.7182	2010.9635	19.2453	-141.1831	-137.1192	20.1557
42	30	19	0.7995	-4.2174	-600.0000	605.4005	5.4005	-39.6315	-39.2634	6.0639
43	31	20	0.7998	0.0000	-992.1032	1000.0000	7.8968	-1.0000	0.0000	10.0001
46	32	21	0.8233	13.6212	1500.0000	-1488.3838	11.6162	-22.2465	-20.0308	14.8848
48	33	22	0.8363	12.8751	1700.0000	-1685.8435	14.1565	-19.3070	-16.4646	16.8590

Table 2.3. AC nodal voltage results for power flow base case

Node	V	$\theta\ (deg)$	Node	V	$\theta\,(deg)$	Node	V	$\theta\,(deg)$
1	1.0000	0.0000	12	0.9999	-21.9153	23	0.9998	-21.6963
2	0.9999	-21.9372	13	1.0000	0.2247	24	0.9996	0.0000
3	1.0000	0.0000	14	1.0000	11.8057	25	0.9999	11.7353
4	1.0000	12.6834	15	1.0000	5.7929	26	1.0002	6.2475
5	1.0000	11.8128	16	1.0000	0.2865	27	1.0000	0.0000
6	1.0000	5.7474	17	1.0000	-0.0573	28	1.0000	0.0000
7	1.0000	0.2472	18	1.0000	-22.0524	29	1.0016	-23.2029
8	1.0000	-3.8360	19	1.0000	-3.8707	30	1.0004	-4.2174
9	1.0000	0.6303	20	1.0000	0.5730	31	1.0000	0.0000
10	1.0000	-0.0630	21	1.0000	12.7687	32	1.0003	13.6212
11	1.0000	0.3151	22	1.0000	11.9094	33	1.0003	12.8751

Table 2.4. DC nodal voltage results for power flow base case

Node	V	Node	V	Node	V	Node	V	Node	V
34	1.0000	37	0.9871	40	1.0114	43	1.0146	46	0.9982
35	1.0091	38	0.9985	41	1.0100	44	1.0092	47	0.9927
36	0.9900	39	1.0067	42	1.0139	45	1.0056	48	0.9835

2.10.2 Case considering violations of current limits

To test the complementarity constraints associated with the current limits, three operational set points and one VSC current capacity are modified as follows: i) the specified reactive power Q_{viac}^{sp} of the converter connected at *vi* node 12 is changed from 0 to 800 MVA; ii) the way the converter connected at *vi* node 14 operates is changed from the reactive power control mode Q_{viac}^{sp} to the voltage control mode V_{vi}^{sp} considering a set point of 1 p.u.; iii) the control mode of the converter at *vi* node 22 is changed from voltage control V_{vi}^{sp} to reactive power control Q_{viac}^{sp} with a specified setpoint of $Q_{viac}^{sp} =$ 40 MVA; and iv) the current limit of the converter at *vi* node 22 is changed from 24 to 16 A p.u.

These operational modifications create overcurrent scenarios in both VSCs mentioned above. The current is limited by active power priority in the converter embedded at *vi* node 12, while the current vector control is applied to the converter at *vi* node 22.

The PF results for the AC-DC converter stations are reported in Table 2.5, where all powers are expressed in MVA and converters' currents are expressed in A p.u. These results indicate that the converter at *vi* node 12 is operating at its current limit of 8 A p.u., and its generation of reactive power is 696.5040 MVARs instead of the original set point of 800 MVARs. Similarly, the converter at *vi* node 22 injects an active power of 1612.22 MW instead of the 1700 MW originally specified and a reactive power of 39.99 MVARs instead of the 40 MVARs specified. Furthermore, the converter's current is at its limit of 16 A p.u.

Lastly, the solution for this second scenario converged in 8 iterations to meet a tolerance of $1\text{x}10^{-6}$ and in 11 iterations to satisfy a tolerance of $1\text{x}10^{-12}$. The increment in the number of iterations in this case study is due to the activation of the complementarity constraints.

2.10.3 Case with violations of modulation indexes and DC voltages

The complementarity constraints associated with the modulation index limits and the *dc* node voltage limits are tested in this section by changing the following control modes and current limits. Firstly, the maximum permissible modulation index of the converters connected at *vi* nodes 12, 18 and 22 is reduced from 0.86 to 0.81, from 0.86 to 0.80 and from 0.86 to 0.83, respectively. Secondly, the minimum modulation index of the converters embedded at *vi* nodes 19 and 20 is increased from 0.77 to 0.80. Lastly, the minimum permissible voltage at the *dc* node of all converters is modified from 0.95 to 0.985.

Table 2.5. AC-DC converters results for pf study considering violations of current limits

dc	*ac*	*vi*	m_a	ϕ (*deg*)	P_{dcac}	P_{acdc}	P_{loss}	Q_{viac}	Q_{kvi}	I_{vsc}
34	23	12	0.8135	-18.2732	384.7557	-382.0992	2.6565	**696.5040**	697.1370	**8.0000**
35	24	13	0.8048	0.0000	-389.2817	392.0188	2.7371	31.5566	31.7112	3.9372
36	25	14	0.8238	8.0381	-121.9047	122.8773	0.9727	-48.7269	-48.7095	1.3043
37	26	15	0.8328	4.7674	800.0000	-793.5841	6.4159	-14.9304	-14.3004	7.9365
39	27	16	0.8060	0.0000	-496.0640	500.0000	3.9360	-0.2500	0.0000	5.0002
40	28	17	0.8113	0.0000	100.7046	-100.0000	0.7046	-0.0100	0.0000	1.0012
41	29	18	0.8086	-19.7156	-1899.1990	1916.7083	17.5094	-800.1259	-795.8120	20.7509
42	30	19	0.7995	-4.2174	-600.0000	605.4005	5.4005	-39.6315	-39.2634	6.0639
43	31	20	0.7998	0.0000	-992.1032	1000.0000	7.8968	-1.0000	0.0000	10.0001
46	32	21	0.8230	12.8763	1500.0000	-1488.3819	11.6181	-21.2801	-19.0643	14.8847
48	33	22	0.8344	9.1239	**1612.2152**	-1599.2231	12.9921	**39.9989**	42.5585	**16.0000**

The PF results for all AC-DC converter stations are presented in Table 2.6. These results clearly show that the converters at *vi* nodes 12, 18 and 22 operate with a modulation index value equal to the upper limit, i.e., 0.81, 0.80 and 0.83, respectively. Note that the opposite occurs in converters at *vi* nodes 19 and 20, which are operating at their lower modulation index limit: 0.80. Note also that the reactive power injected by the converter at *vi* node 12 is 415.03 MVARs instead of the originally specified 0 MVARs. Regarding the voltage magnitude setpoint specified at the converters *vi* node, it is observed in Table 2.7 that converters at *vi* nodes 18, 19, 20 and 22 do not achieve the specified control action, i.e., the voltage at that node is 0.9924, 1.0006, 1.0003 and 0.9946 p.u., respectively, instead of 1.0 p.u. The last converter is also operating at its lower DC voltage limit of 0.985 p.u. as shown in Table 2.8, while its active power is 1591.96 MW as observed in Table 2.6 instead of the specified set point of 1700 MW.

Lastly, the PF solution for this case study converged in six iterations to a tolerance of $1\text{x}10^{-7}$ and in seven iterations to a tolerance of $1\text{x}10^{-12}$.

Table 2.6. AC-DC converters results for pf study considering violations of modulation indexes and DC voltages

dc	*ac*	*vi*	m_a	ϕ (*deg*)	P_{dcac}	P_{acdc}	P_{loss}	Q_{viac}	Q_{kvi}	I_{vsc}
34	23	12	**0.8100**	-17.6301	384.7484	-382.0760	2.6724	**415.0335**	415.3573	5.7265
35	24	13	0.8048	0.0000	-389.2743	392.0113	2.7370	32.5614	32.7162	3.9381
36	25	14	0.8190	7.2207	-121.9047	122.8796	0.9749	0.0000	0.0153	1.2364
37	26	15	0.8328	4.4302	800.0000	-793.5845	6.4155	-18.9548	-18.3247	7.9371
39	27	16	0.8060	0.0000	-496.0640	500.0000	3.9360	-0.2500	0.0000	5.0002
40	28	17	0.8113	0.0000	100.7046	-100.0000	0.7046	-0.0100	0.0000	1.0012
41	29	18	**0.8000**	-19.0835	-1877.8816	1895.3729	17.4913	-498.6096	-494.7091	19.7371
42	30	19	**0.8000**	-4.2262	-600.0000	605.3946	5.3946	-40.6758	-40.3081	6.0607
43	31	20	**0.8000**	0.0000	-992.1069	1000.0000	7.8931	-0.9994	0.0000	9.9971
46	32	21	0.8229	12.7068	1500.0000	-1488.3815	11.6185	-21.1037	-18.8880	14.8847
48	33	22	**0.8300**	8.3050	**1591.9608**	-1579.1307	12.8301	1.9154	4.4362	15.8769

Table 2.7. AC nodal voltages for pf study considering violations of modulation indexes and DC voltages

Node	V	θ (*deg*)	Node	V	θ (*deg*)	Node	V	θ (*deg*)
1	1.0000	0.0000	12	0.9914	-17.8538	23	0.9872	-17.6301
2	0.9919	-17.8760	13	1.0000	0.2247	24	0.9996	0.0000
3	1.0000	0.0000	14	0.9946	7.2919	25	0.9946	7.2207
4	1.0000	11.7689	15	1.0000	3.9755	26	1.0002	4.4302
5	0.9946	7.2990	16	1.0000	0.2865	27	1.0000	0.0000
6	1.0000	3.9301	17	1.0000	-0.0573	28	1.0000	0.0000
7	1.0000	0.2471	18	**0.9924**	-17.9864	29	0.9975	-19.0835
8	1.0006	-3.8453	19	**1.0006**	-3.8799	30	1.0010	-4.2262
9	1.0003	0.6299	20	**1.0003**	0.5726	31	1.0003	0.0000
10	1.0000	-0.0630	21	1.0000	11.8542	32	1.0003	12.7068
11	1.0000	0.3151	22	**0.9946**	7.3905	33	0.9947	8.3050

Table 2.8. DC nodal voltages for pf study considering violations of modulation indexes and DC voltages

Node	V	Node	V	Node	V	Node	V	Node	V
34	1.0000	37	0.9871	40	1.0114	43	1.0146	46	0.9986
35	1.0091	38	0.9985	41	1.0100	44	1.0092	47	0.9936
36	0.9900	39	1.0067	42	1.0139	45	1.0056	48	**0.9850**

2.10.4 Power flow study of an electric grid with wind generators

In order to test the proposed DFIG power flow model, a 2 MW DFIG is connected to node 5 of the IEEE 5-bus test system [Abur & Exposito 2004]. The DFIG parameters are the ones reported in [Li S. 2013]. The powers P_m, P_s and P_{rsc} and the slip value are presented in Table 2.9 for different wind speeds. In this specific case study, the nominal DFIG power is achieved with a wind speed around 16m/s. Furthermore, the slip values are solved according to the

Table 2.9 DFIG power flow solution for different wind speeds

v (m/s)	P_m (MW)	P_s (MW)	P_{rsc} (MW)	s
4.0	0.0428	0.0645	-0.0217	0.3360
6.0	0.2260	0.3375	-0.1114	0.3302
8.0	0.3775	0.5599	-0.1824	0.3258
10.0	1.0548	0.9290	0.1258	-0.1354
12.0	1.5470	1.3610	0.1860	-0.1367
14.0	1.8778	1.6507	0.2270	-0.1375
16.0	2.0179	1.7734	0.2446	-0.1379
18.0	1.9887	1.7478	0.2409	-0.1378
20.0	1.8359	1.6141	0.2218	-0.1374
22.0	1.6104	1.4166	0.1938	-0.1368
24.0	1.3560	1.1935	0.1625	-0.1362

system and wind conditions in a unified solution frame where in all cases the solution was found in six iterations for a tolerance of 1×10^{-6}.

2.11 Conclusions

In this chapter a new VSC model was presented where the voltage on both sides of the AC-DC converter, the modulation index, the converter's firing angle and the associated reactive power generation are treated as state variables. The integration of these state variables together with the complementarity constraints' method allows the inclusion of the VSC outer control modes, the inner current control, the modulation index limits and the DC voltage limits to ensure a feasible unified power flow solution in the context of VSC-based multi-terminal AC-DC networks. This new constrained VSC model can be used to model back-to-back converters in wind generators such as DFIG and PMSGs. Lastly, the functionality of the proposed VSC model and the proposed complementarity constraints application has been demonstrated by numerical examples.

Chapter 3

3 Multi-terminal AC-DC Static State Estimation

3.1 Introduction

This chapter focuses on the static state estimation of multi-terminal AC-DC power electric transmission systems. Three main contributions are presented. Firstly, a unified formulation to solve the static state estimation of VSC based multi-terminal AC-DC transmission systems containing DC-DC converters. Secondly, two new bad data analysis (BDA) approaches for Gaussian and non-Gaussian errors capable to identify multiple bad data. Finally, an inequality constrained static state estimation (ICSSE) formulation where system operational variables are constrained to a feasible range to enhance the estimation solution.

3.2 State estimation on multi-terminal AC-DC systems

Power systems state estimation is the process carried out in energy control centers in order to provide the best estimate of what is happening in the system based on real-time system measurements and a predetermined system model. A redundant set of real-time measurements are collected from the entire network through the supervisory control and data acquisition system and phasor measurements units. These measurements are transmitted to the ECC and subjected to a statistical analysis in order to assess the system's state. Since transmitted measurements are usually corrupted by errors, this erroneous data should be filtered to eliminate bad measurements and minimize the effect of measurement noise. This is accomplished with the help of a supplementary function called bad data processing. If after this analysis all state variables can be estimated using the available measurements, a system is said to be observable [Abur & Exposito 2004]. For purpose of this work, it is assumed that the network is observable. Once an accurate estimation has been carried out, the entire system quantities such as branch power flows, line current magnitudes and nodal power injections can be calculated.

In this proposed approach, the nodal voltages at the DC grid, the duty cycles of the DC-DC converters, the VSCs' control variables, as well as the on-load tap-changer of the transformer connecting the converter station to the AC grid, are simultaneously estimated together with the AC nodal voltages. In this case, the VSCs' control variables are associated with the pulse-width modulation (PWM) index and the phase control signal [Martínez-Parrales & Fuerte-Esquivel 2018].

Unlike all other proposals, the multi-terminal DC network considers DC-DC converters for representing how the DC power can be transmitted at different voltage levels. The proposal straightforwardly estimates the different DC voltage magnitudes at which the DC network is operating. Furthermore, the formulation permits considering two or more VSC-MTDCs embedded within a large AC system or connecting two or more independent AC transmission systems.

The VSC-MTDC systems are incorporated into a Hachtel-based state estimation, with the operational constraints of the VSC-based AC-DC station model directly considered in the formulation.

Based on the fact that residuals are considered variables to be estimated in the Hachtel method, a new bad data analysis is proposed where the original number of measurements used for the estimation is not altered because the bad data are corrected during the iterative estimation process. This contrasts with the bad data analysis used in all the proposals reported above, where bad data are eliminated from the set of measurements.

The unified state estimation of AC and DC variables is performed by simultaneously processing measurements provided by a SCADA system and PMUs, which is not the case in all other proposals.

3.3 Formulation of AC-DC static state estimation

In this proposal, the estimated state variables $\hat{\boldsymbol{x}} \in \mathbb{R}^{\mathrm{n}}$ is formed by the voltage magnitudes and phase angles in AC nodes, nodal voltage magnitudes in DC networks, as well as state variables associated with the VSC and DC-DC converters:

$$\hat{\boldsymbol{x}} = \left[\hat{\boldsymbol{\theta}}_{AC} \ \hat{\boldsymbol{V}}_{AC} \ \hat{\boldsymbol{V}}_{DC} \ \hat{\boldsymbol{m}}_{a} \ \hat{\boldsymbol{D}} \right]^{\mathrm{T}} . \tag{3.1}$$

The super index T denotes transposition, vectors and matrices are denoted in bold italic letters and the estimated values of state variables are given in per unit. In this case, a nodal voltage reference angle is defined at each independent AC network and hence not included in $\hat{\boldsymbol{x}}$, unless this network contains a voltage angle PMU measurement. Finally, the state variables associated with VSCs are defined based on the circuit model detailed in Section 2.3 where the angle ϕ of the phase shift transformer is equal to the voltage phase angle of the corresponding *ac* node θ_{ac} which is an element of the $\hat{\boldsymbol{\theta}}_{AC}$ set.

The SE is performed based on the set of physical measurements $\boldsymbol{z} \in \mathbb{R}^{\mathrm{m}}$ collected from the AC-DC network through a supervisory control and data acquisition (SCADA) system and PMUs:

$$\boldsymbol{z} = \left[\boldsymbol{z}_{\mathrm{SCADA}} \boldsymbol{z}_{\mathrm{PMU}}\right]^{\mathrm{T}} . \tag{3.2}$$

In this case, the set of measurements provided by the SCADA system is composed of branch power flows, nodal power injections and nodal voltage magnitudes:

$$\boldsymbol{z}_{\mathrm{SCADA}} = \left\lfloor \boldsymbol{P}_{branch} \ \boldsymbol{Q}_{branch} \ \boldsymbol{P}_{inj} \ \boldsymbol{Q}_{inj} \ \boldsymbol{V} \right\rfloor . \tag{3.3}$$

On the other hand, the set of PMU measurements are associated with phasors of nodal voltages and branch current flows:

$$\boldsymbol{z}_{\mathrm{PMU}} = \left\lfloor \boldsymbol{\theta}_{PMU} \ \boldsymbol{V}_{PMU} \ \boldsymbol{I}_{PMU,r} \ \boldsymbol{I}_{PMU,i} \right\rfloor . \tag{3.4}$$

Note that branch current measurements are considered in rectangular coordinates to avoid the convergence problems reported in [Chakrabarti *et al*. 2010].

The measurement values are mathematically expressed by:

$$\boldsymbol{z} = \boldsymbol{h}(\boldsymbol{x}) + \boldsymbol{\varepsilon} = \boldsymbol{h}(\hat{\boldsymbol{x}}) + \boldsymbol{r} , \tag{3.5}$$

where $\boldsymbol{h}(\cdot) \in \mathbb{R}^{\mathrm{m}}$ is the vector of nonlinear functions that relate $\boldsymbol{z}$ and $\hat{\boldsymbol{x}}$ based on the mathematical representation of physical measurements. In this case, this vector of estimated measurements is denoted as:

$$\boldsymbol{h}(\hat{\boldsymbol{x}}) = [\hat{\boldsymbol{h}}_{\mathrm{SCADA}} \hat{\boldsymbol{h}}_{\mathrm{PMU}}]^{\mathrm{T}} , \tag{3.6}$$

$$\hat{\boldsymbol{h}}_{\mathrm{SCADA}} = [\hat{\boldsymbol{P}}_{branch}\ \hat{\boldsymbol{Q}}_{branch}\ \hat{\boldsymbol{P}}_{inj}\ \hat{\boldsymbol{Q}}_{inj}\ \hat{\boldsymbol{V}}], \tag{3.7}$$

$$\hat{\boldsymbol{h}}_{\mathrm{PMU}} = [\hat{\boldsymbol{\theta}}_{PMU}\ \hat{\boldsymbol{V}}_{PMU}\ \hat{\boldsymbol{I}}_{PMU,r}\ \hat{\boldsymbol{I}}_{PMU,i}]. \tag{3.8}$$

On the other hand, $\boldsymbol{\varepsilon} \in \mathbb{R}^{\mathrm{m}}$ is the vector of uncorrelated noise errors in measurements with expected values $E(\boldsymbol{\varepsilon}) = 0$ and covariance matrix $cov(\boldsymbol{\varepsilon}) = \boldsymbol{R}$. In this regard, $\boldsymbol{R} \in \mathbb{R}^{\mathrm{m\,x\,m}}$ is a diagonal matrix $\boldsymbol{R} = diag\left\lfloor \boldsymbol{R}^{SCADA}\ \boldsymbol{R}_{\boldsymbol{V}}^{PMU}\ \boldsymbol{R}_{I}^{PMU} \right\rfloor$ with elements that are the variances of noise errors denoted as:

$$\left[\boldsymbol{R}^{SCADA}\right] = diag\left\{\boldsymbol{\sigma}_{\boldsymbol{P}_{inj}}^{2}\ \boldsymbol{\sigma}_{\mathbf{Q}_{inj}}^{2}\ \boldsymbol{\sigma}_{\boldsymbol{P}_{branch}}^{2}\ \boldsymbol{\sigma}_{\mathbf{Q}_{branch}}^{2}\ \boldsymbol{\sigma}_{\mathbf{V}}^{2}\right\}, \tag{3.9}$$

$$\left[\boldsymbol{R}_{V}^{PMU}\right] = diag\left\{\boldsymbol{\sigma}_{\boldsymbol{\theta}^{PMU}}^{2}\ \boldsymbol{\sigma}_{\mathbf{V}^{PMU}}^{2}\right\}, \tag{3.10}$$

$$\left[\boldsymbol{R}_{I}^{PMU}\right] = diag\left\{\boldsymbol{\sigma}_{\boldsymbol{I}_{branch,r}}^{2}\ \boldsymbol{\sigma}_{\boldsymbol{I}_{branch,i}}^{2}\right\}. \tag{3.11}$$

Lastly, $\sigma_{(\cdot)}$ is the standard deviation of the measurement type (·) that reflects the expected accuracy of the corresponding measurement device.

The AC-DC state estimation problem is mathematically formulated as an equality constrained least squares (ECLS) problem, which is solved by Hachtel's augmented matrix method [Gjelsvik *et al.* 1985] to find the estimates $\hat{\boldsymbol{x}}$ that minimizes the weighted squares sum

$$J(\hat{\boldsymbol{x}}) = \left(\boldsymbol{z} - \boldsymbol{h}(\hat{\boldsymbol{x}})\right)^{\mathrm{T}} \boldsymbol{R}^{-1} \left(\boldsymbol{z} - \boldsymbol{h}(\hat{\boldsymbol{x}})\right), \tag{3.12}$$

while equality constraints

$$\boldsymbol{c}(\hat{\boldsymbol{x}}) = \mathbf{0}\ , \tag{3.13}$$

$$\hat{\boldsymbol{r}} - \left(\boldsymbol{z} - \boldsymbol{h}(\hat{\boldsymbol{x}})\right) = \mathbf{0}\ , \tag{3.14}$$

are satisfied. In this case $\boldsymbol{c}(\hat{\boldsymbol{x}}) \in \mathbb{R}^{\mathrm{c}}$ corresponds to zero injection measurements and power mismatch equations in the AC-DC interface, whereas the second set of constraints corresponds to the residual equations. In this formulation, the vector of measurement residuals is treated as unknown and retained as explicit variables $\hat{\boldsymbol{r}} \in \mathbb{R}^{\mathrm{m}}$ [Gjelsvik *et al.* 1985]. The ECLS problem is formulated by using the Lagrangian method, which results in

$$\mathcal{L}(\hat{\boldsymbol{x}}, \hat{\boldsymbol{r}}, \boldsymbol{\lambda}, \boldsymbol{\mu}) = J(\hat{\boldsymbol{r}}) - \boldsymbol{\lambda}^{\mathrm{T}} \boldsymbol{c}(\hat{\boldsymbol{x}}) - \boldsymbol{\mu}^{\mathrm{T}} (\hat{\boldsymbol{r}} - \boldsymbol{z} + \boldsymbol{h}(\hat{\boldsymbol{x}}))\ , \tag{3.15}$$

with Lagrange multipliers denoted by $\boldsymbol{\lambda} \in \mathbb{R}^{\mathrm{c}}$ and $\boldsymbol{\mu} \in \mathbb{R}^{\mathrm{m}}$.

In this context, the estimated state $\hat{\boldsymbol{x}}$ is the solution that satisfies the first-order optimality conditions of the Lagrangian function (3.15) with respect to the variables $(\hat{\boldsymbol{x}}, \hat{\boldsymbol{r}}, \boldsymbol{\lambda}, \boldsymbol{\mu})$. Since the equations representing these optimality conditions are nonlinear, these equations are linearized by the Newton-Raphson method with respect to $\hat{\boldsymbol{x}}$ in order to obtain the following set of mathematical equations:

$$\left[\boldsymbol{C}\left(\hat{\boldsymbol{x}}^k\right)^{\mathrm{T}} + (\Delta\hat{\boldsymbol{x}}^k)\mathcal{C}\left(\hat{\boldsymbol{x}}^k\right)^{\mathrm{T}}\right]\boldsymbol{\lambda}^k + \left[\boldsymbol{H}\left(\hat{\boldsymbol{x}}^k\right)^{\mathrm{T}} + (\Delta\hat{\boldsymbol{x}}^k)\mathcal{H}\left(\hat{\boldsymbol{x}}^k\right)^{\mathrm{T}}\right]\boldsymbol{\mu}^k = 0, \tag{3.16}$$

$$\boldsymbol{c}(\hat{\boldsymbol{x}}^k) + \boldsymbol{C}\left(\hat{\boldsymbol{x}}^k\right)(\Delta\hat{\boldsymbol{x}}^k) = 0, \tag{3.17}$$

$$\boldsymbol{R}^{-1}\hat{\boldsymbol{r}}^k - \boldsymbol{\mu}^k = 0, \tag{3.18}$$

$$\hat{\boldsymbol{r}}^k - \boldsymbol{z} + \boldsymbol{h}\left(\hat{\boldsymbol{x}}^k\right) + \boldsymbol{H}(\hat{\boldsymbol{x}}^k)(\Delta\hat{\boldsymbol{x}}^k) = 0, \tag{3.19}$$

where the superindex k represent the iteration number, while $\boldsymbol{C}(\hat{\boldsymbol{x}}) = \partial\boldsymbol{c}(\hat{\boldsymbol{x}})/\partial\boldsymbol{x}$, $\mathcal{C}(\hat{\boldsymbol{x}}) = \partial^2\boldsymbol{c}(\hat{\boldsymbol{x}})/\partial^2\boldsymbol{x}$, $\boldsymbol{H}(\hat{\boldsymbol{x}}) = \partial\boldsymbol{h}(\hat{\boldsymbol{x}})/\partial\boldsymbol{x}$ and $\mathcal{H}(\hat{\boldsymbol{x}}) = \partial^2\boldsymbol{h}(\hat{\boldsymbol{x}})/\partial^2\boldsymbol{x}$. Since the estimated adjustments of state variables become smaller during the iterative process, $\Delta\hat{\boldsymbol{x}} \to \boldsymbol{0}$ as $k \to \infty$, the Hessian matrices can be neglected from obtaining a quasilinear Newton's method with (3.16) given by (3.20). Furthermore, (3.18) can be expressed as (3.21) and substituted in (3.19) to obtain (3.22). Hence, the resulting quasi-linearized problem is given by the set of equations (3.23):

$$\boldsymbol{C}\left(\hat{\boldsymbol{x}}^k\right)^{\mathrm{T}}\boldsymbol{\lambda}^k + \boldsymbol{H}\left(\hat{\boldsymbol{x}}^k\right)^{\mathrm{T}}\boldsymbol{\mu}^k = 0, \tag{3.20}$$

$$\hat{\boldsymbol{r}}^k = \boldsymbol{R}\boldsymbol{\mu}^k, \tag{3.21}$$

$$\boldsymbol{R}\boldsymbol{\mu}^k + \boldsymbol{H}(\hat{\boldsymbol{x}}^k)\Delta\hat{\boldsymbol{x}}^k = \boldsymbol{z} - \boldsymbol{h}\left(\hat{\boldsymbol{x}}^k\right), \tag{3.22}$$

$$\begin{pmatrix} \boldsymbol{R} & \boldsymbol{H}(\hat{\boldsymbol{x}}^k) & \boldsymbol{0} \\ \boldsymbol{H}(\hat{\boldsymbol{x}}^k)^{\mathrm{T}} & \boldsymbol{0} & \boldsymbol{C}(\hat{\boldsymbol{x}}^k)^{\mathrm{T}} \\ \boldsymbol{0} & \boldsymbol{C}(\hat{\boldsymbol{x}}^k) & \boldsymbol{0} \end{pmatrix} \begin{pmatrix} \boldsymbol{\mu}^k \\ \Delta\hat{\boldsymbol{x}}^k \\ \boldsymbol{\lambda}^k \end{pmatrix} = \begin{pmatrix} \boldsymbol{z} - \boldsymbol{h}(\hat{\boldsymbol{x}}^k) \\ \boldsymbol{0} \\ -\boldsymbol{c}(\hat{\boldsymbol{x}}^k) \end{pmatrix}. \tag{3.23}$$

The Jacobian matrix $\boldsymbol{H}(\hat{\boldsymbol{x}})=\left[\boldsymbol{H}_{SCADA}(\hat{\boldsymbol{x}})\ \boldsymbol{H}_{PMU}(\hat{\boldsymbol{x}})\right]^{\mathrm{T}}$ is given by

$$\boldsymbol{H}(\hat{\boldsymbol{x}})=\begin{bmatrix} \partial\hat{\boldsymbol{P}}_{\text{flow}}/\partial\hat{\boldsymbol{\theta}}_{ac} & \partial\hat{\boldsymbol{P}}_{\text{flow}}/\partial\hat{\boldsymbol{V}}_{ac} & \partial\hat{\boldsymbol{P}}_{\text{flow}}/\partial\hat{\boldsymbol{V}}_{dc} & \partial\hat{\boldsymbol{P}}_{\text{flow}}/\partial\hat{\boldsymbol{m}}_{a} & \partial\hat{\boldsymbol{P}}_{\text{flow}}/\partial\hat{\boldsymbol{D}} \\ \partial\hat{\boldsymbol{Q}}_{\text{flow}}/\partial\hat{\boldsymbol{\theta}}_{ac} & \partial\hat{\boldsymbol{Q}}_{\text{flow}}/\partial\hat{\boldsymbol{V}}_{ac} & 0 & \partial\hat{\boldsymbol{Q}}_{\text{flow}}/\partial\hat{\boldsymbol{m}}_{a} & 0 \\ \partial\hat{\boldsymbol{P}}_{\text{inj}}/\partial\hat{\boldsymbol{\theta}}_{ac} & \partial\hat{\boldsymbol{P}}_{\text{inj}}/\partial\hat{\boldsymbol{V}}_{ac} & \partial\hat{\boldsymbol{P}}_{\text{inj}}/\partial\hat{\boldsymbol{V}}_{dc} & \partial\hat{\boldsymbol{P}}_{\text{inj}}/\partial\hat{\boldsymbol{m}}_{a} & \partial\hat{\boldsymbol{P}}_{\text{inj}}/\partial\hat{\boldsymbol{D}} \\ \partial\hat{\boldsymbol{Q}}_{\text{inj}}/\partial\hat{\boldsymbol{\theta}}_{ac} & \partial\hat{\boldsymbol{Q}}_{\text{inj}}/\partial\hat{\boldsymbol{V}}_{ac} & 0 & \partial\hat{\boldsymbol{Q}}_{\text{inj}}/\partial\hat{\boldsymbol{m}}_{a} & 0 \\ 0 & \partial\hat{\boldsymbol{V}}/\partial\hat{\boldsymbol{V}}_{ac} & \partial\hat{\boldsymbol{V}}/\partial\hat{\boldsymbol{V}}_{dc} & 0 & 0 \\ \partial\hat{\boldsymbol{\theta}}^{PMU}/\partial\hat{\boldsymbol{\theta}}_{ac} & 0 & 0 & 0 & 0 \\ 0 & \partial\hat{\boldsymbol{V}}^{PMU}/\partial\hat{\boldsymbol{V}}_{ac} & 0 & 0 & 0 \\ \partial\hat{\boldsymbol{I}}^{r}/\partial\hat{\boldsymbol{\theta}}_{ac} & \partial\hat{\boldsymbol{I}}^{r}/\partial\hat{\boldsymbol{V}}_{ac} & \partial\hat{\boldsymbol{I}}^{r}/\partial\hat{\boldsymbol{V}}_{dc} & \partial\hat{\boldsymbol{I}}^{r}/\partial\hat{\boldsymbol{m}}_{a} & \partial\hat{\boldsymbol{I}}^{r}/\partial\hat{\boldsymbol{D}} \\ \partial\hat{\boldsymbol{I}}^{i}/\partial\hat{\boldsymbol{\theta}}_{ac} & \partial\hat{\boldsymbol{I}}^{i}/\partial\hat{\boldsymbol{V}}_{ac} & \partial\hat{\boldsymbol{I}}^{i}/\partial\hat{\boldsymbol{V}}_{dc} & \partial\hat{\boldsymbol{I}}^{i}/\partial\hat{\boldsymbol{m}}_{a} & \partial\hat{\boldsymbol{I}}^{i}/\partial\hat{\boldsymbol{D}} \end{bmatrix}. \tag{3.24}$$

3.3.1 Voltage source converter-based AC-DC station model

The schematic representation of the VSC-based AC–DC station connected to the secondary winding of an on-load tap-changing (OLTC) transformer and the integrated equivalent electric circuit of both components is shown in Fig. 2.1.

3.3.1.1 Measurements at the AC-DC converter station

For the SE solution, the possible locations of SCADA and PMU measurements at the converter station are shown in Fig. 3.1. These measurements are associated with the active power flowing into the converter's DC terminal, the active power flowing into the AC terminal, as well as the active and reactive powers flowing from the filter bus to the AC terminal and *vice versa* as well as the nodal voltages and currents of the reactor, the filter and the current injected on the *vi* bus.

In this case, the power flow measurements are mathematically represented by

$$P_{dcac}=V_{dc}{}^{2}\left(G_{sw}+K^{2}m_{a}{}^{2}R_{1}^{-1}\right)-Km_{a}V_{dc}V_{ac}R_{1}^{-1}\ , \tag{3.25}$$

$$P_{acdc}=R_{1}^{-1}V_{ac}^{2}-Km_{a}V_{dc}V_{ac}R_{1}^{-1}, \tag{3.26}$$

$$P_{viac}=G_{kk}V_{vi}{}^{2}+V_{vi}V_{ac}\left(G_{km}\cos\left(\theta_{vi}-\theta_{ac}\right)+B_{km}\sin\left(\theta_{vi}-\theta_{ac}\right)\right)\ , \tag{3.27}$$

$$Q_{viac}=-B_{kk}V_{vi}{}^{2}+V_{vi}V_{ac}\left(G_{km}\sin\left(\theta_{vi}-\theta_{ac}\right)-B_{km}\cos\left(\theta_{vi}-\theta_{ac}\right)\right)\ , \tag{3.28}$$

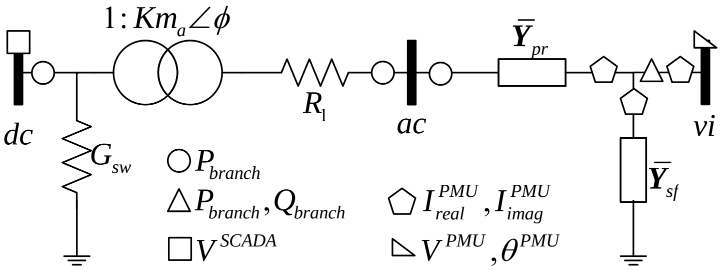

Fig. 3.1 Possible location of measurements in a converter station for SE.

$$P_{acvi} = G_{mm} V_{ac}^{\ 2} + V_{ac} V_{vi} \left(G_{mk} \cos\left(\theta_{ac} - \theta_{vi}\right) + B_{mk} \sin\left(\theta_{ac} - \theta_{vi}\right)\right) , \tag{3.29}$$

$$Q_{acvi} = -B_{mm} V_{ac}^{\ 2} + V_{ac} V_{vi} \left(G_{mk} \sin\left(\theta_{ac} - \theta_{vi}\right) - B_{mk} \cos\left(\theta_{ac} - \theta_{vi}\right)\right), \tag{3.30}$$

where the sub-indices indicate the sending and the receiving node in a two ports model. Furthermore, G_{kk} and B_{kk} are the respective real and imaginary parts of $\bar{\boldsymbol{Y}}_{sf} + \bar{\boldsymbol{Y}}_{pr}$, G_{mm} and B_{mm} the respective real and imaginary parts of $\bar{\boldsymbol{Y}}_{pr}$, $G_{km} = G_{mk} = -G_{mm}$ and $B_{km} = B_{mk} = -B_{mm}$.

3.3.2 DC line model

Under the assumption that active power measurements are located at both ends of a DC transmission line, which is represented by the π equivalent circuit shown in Fig. 3.2, their corresponding mathematical representation is given by

$$P_{km} = V_k^2 \left(G_d + G_{shd} \right) - V_k V_m G_d , \tag{3.31}$$

$$P_{mk} = V_m^2 \left(G_d + G_{shd} \right) - V_m V_k G_d . \tag{3.32}$$

3.3.3 DC-DC converter model

Based on the dynamic model for the DC-DC converter reported in [Vrana *et al.* 2013], a steady-state model is proposed for this converter based on the equivalent circuit shown in Fig. 3.3. Note that the converter side V_k, where the voltage is measured, is represented by an ideal current source behind a conductance, whereas the V_c side is represented by a voltage source behind a resistance. The relationship between these two ideal sources is represented by the

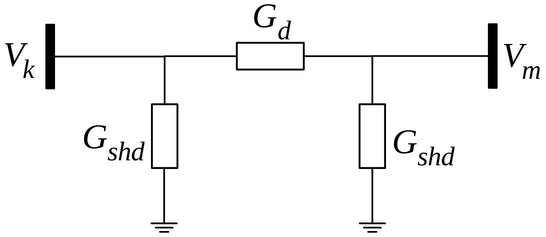

Fig. 3.2 Equivalent circuit of DC lines.

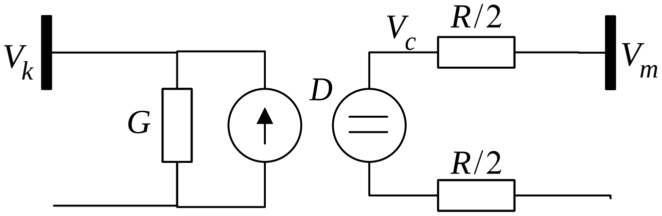

Fig. 3.3 Equivalent circuit of DC-to-DC converter.

duty cycle $D = V_c / V_k$, which must be determined in order to achieve a specified active power to be injected at bus *m*. Hence, the duty cycle is added to the state vector: $\hat{\boldsymbol{x}}_{DCDC} = \left[\hat{\boldsymbol{D}}\right]$.

For the purpose of SE, the active power flow equations representing SCADA active power flow measurements at both terminals of the DC-DC converter are as follows:

$$P_{km} = V_k^2 \left[G + \left(2D^2 / R \right) \right] - V_k V_m \left(2D / R \right), \tag{3.33}$$

$$P_{mk} = V_m^2 \left(2 / R \right) - V_m V_k \left(2D / R \right). \tag{3.34}$$

3.3.4 Initialization of state variables

An initial value must be assigned to each state variable to be estimated, which should be reasonably close to its true value, to initiate the iterative estimation process. Therefore, if no prior information of the system state is available, all AC and DC voltage magnitudes are initialized in one per-unit and AC voltage phase angles in zero radians. The tap values of OLTC transformers of the converter stations and the duty cycles of the DC-DC converters are initialized in one per-unit. Finally, the proposed formulas in Section 2.9.4 are applied to calculate the initial values for the state variables associated with the VSC.

3.4 Bad data analysis

The detection, identification and correction/elimination of multiple bad data reported in [Martínez-Parrales & Fuerte-Esquivel 2018] are detailed in this section. This BDA is performed in a four-stage process, which can be indistinctly executed at the end of each iteration of the estimation process or once the operating state has been estimated. First, the presence of bad data is detected, and a set of suspected measurements with gross errors is formed. Second, a threshold filter is applied to the set of suspected bad data to remove good measurements with residuals that have been biased by bad measurements. Third, a correlation filter is applied to the resulting set of suspected bad data to determine the subset of uncorrelated measurements with gross errors that are identified as bad. Lastly, the last subset of bad data is corrected or eliminated depending on how the BDA is applied. The measurements with gross errors are corrected if the BDA is performed during the state estimation process. Contrarily, these erroneous data are eliminated to perform a new estimation considering the updated data set of measurements.

In the first stage, any measurement is considered a suspected bad datum if the absolute value of its corresponding estimated residual $\left|\hat{r}_i\right|$ is greater than Th times its standard deviation. Hence, a set of suspected bad data (SBD) is composed of all *i*-th measurements for which $\left|\hat{r}_i\right|/\sigma_i > Th$ is satisfied, where *Th* is a threshold for bad data detection. Note that the solution of (3.23) for $\left[\boldsymbol{\mu}, \Delta\hat{\boldsymbol{x}}, \boldsymbol{\lambda}\right]^{\mathrm{T}}$ allows directly obtaining from (3.18) the values of estimated residuals: $\hat{\boldsymbol{r}} = \boldsymbol{R\mu}$. Note also that the estimated residuals are related to the residuals $\boldsymbol{r}$ by $\hat{\boldsymbol{r}} = \boldsymbol{z} - \boldsymbol{h}\left(\hat{x}\right) - \boldsymbol{H}(\hat{x})(\Delta\hat{x}) = \boldsymbol{r} - \boldsymbol{H}(\hat{x})(\Delta\hat{x})$.

In case of multiple bad data, the set of *SBD* might contain good measurements because their residual values are comparable to the ones associated with bad measurements. Therefore, once the set of *SBD* is obtained, another filtering must be applied to avoid identifying good measurements as bad data because of strongly correlated residuals. One way of performing this filtering consists of directly estimating the errors associated with a reduced number of measurements, which are selected from the set of *SBD* [Cutsem *et al*. 1984]. Note that the user decides the selected number of measurements [Abur & Exposito 2004] based on the constraint that they must be linearly independent and noncritical. The estimation of errors is performed by applying a hypothesis testing identification under the assumptions that the errors have a Gaussian probability distribution and that the rest of the unselected measurements are free of errors. On the other hand, the filtering proposed in [Martínez-Parrales & Fuerte-Esquivel 2018] consists of comparing the normalized estimated residual (*NER*) of each measurement composing the set of *SBD* with respect to a smearing effect threshold Th_{se}. In this second stage, only the measurements with normalized estimated residuals higher than or equal to Th_{se} are maintained in the *SBD* set. This filtering is indistinctly applied to both correlated and uncorrelated measurements to bad data. In this context, two measurements are correlated when they have at least one variable in common in their corresponding mathematical representation $\boldsymbol{h}(\hat{\boldsymbol{x}})$; otherwise, the measurements are uncorrelated. The smearing effect threshold Th_{se} is given by

$$Th_{se} = \alpha\left(LNER - Th\right) + Th \ , \tag{3.35}$$

where $0 \le \alpha \le 1$ is a tuning parameter that defines the number of measurements composing the resulting subset of suspected bad data at the end of the filtering stage. The physical meaning of (3.35) is that the number of measurements that must be considered without gross errors are those with normalized estimated residuals that are less than the weighted distance between the LNER and the *Th* sigma limit. Hence, when $\alpha = 1$, the measurement with the *LNER* will be identified as the only bad datum in the set of measurements. In case of existing multiple bad data, however, the solution of the SE problem will be the slowest possible. On the other hand, if $\alpha = 0$ there is no filtering process, and the original set of *SBD* remains unaltered. Lastly, in a firsthand experience based on the Monte Carlo simulation on different systems with different measurement configurations, a value of $\alpha = 0.5$ provides a good balance between the filtering process's efficiency and the accuracy of the SE results. Hence, this value is the one adopted for all simulations reported in this work. Choosing an alpha value of 0.5 is equivalent to the assumption that the bad measurement with the LNER can only bias the uncorrelated measurements' normalized residuals up to half the distance between the *Th* sigma limit and the LNER. Note that the presence of injection measurements smear gross errors between uncorrelated measurements. In this sense, the greater the number of injection measurements, the higher the value of α must be. In the engineering practice adopted to estimate the operating state of the Mexican interconnected system, this type of measurement is not used such that the value of α can be as low as 0.2.

A graphical representation of the smearing effect filtering process is shown in Fig. 3.4, where the set of measurements corresponds to case study 1 reported in Chapter 4. In this case, the red dots represent the 13 measurements contaminated with gross errors, while the blue squares denote good measurements that are correlated with at least one bad datum. On the other hand, the star symbol is used to represent all good measurements uncorrelated to bad measurements, but with their *NER* greater than *Th*. Note that the *NER* of 5 uncorrelated good measurements has been biased to a value up to *Th*, but none of these measurements is identified as a bad datum because in the filtering stage none of them passes the test of Th_{se}. Note also that despite the filtering process some good measurements correlated to bad data will be misidentified such that a second filtering process is necessary as explained next.

An additional correlation filtering is now performed in the resulting subset of *SBD* in order to remove the measurements correlated to bad data. The reason for this correlation filtering is that a bad datum has a stronger smearing effect on the estimated residues of good measurements with which it is correlated so that these good measurements pass the smearing effect threshold test, as shown in Fig. 3.4.

Based on the information mentioned above, in this third stage of the bad data analysis the measurement with the *LNER* is moved into an identified bad data (*IBD)* set, and all its correlated measurements are removed from the subset of *SBD*. This process is repeated until this last subset is empty.

A flowchart explaining the proposed unified approach for the state estimation and bad data analysis for electric power transmission networks is shown in Fig. 3.5.

The correlation between measurements is directly obtained from the Jacobian matrix $\boldsymbol{H}(\hat{\boldsymbol{x}})$. This is possible because the nonzero elements in the columns associated with the nonzero elements of the row related to the measurement with the *LNER* indicate the measurements with state variables in common with this bad datum. By way of example, consider the Jacobian matrix shown in Fig. 3.6. In this case, the measurement z_4 has the *LNER* and the nonzero elements in its corresponding row determine the relation of z_4 with the state variables x_1 and

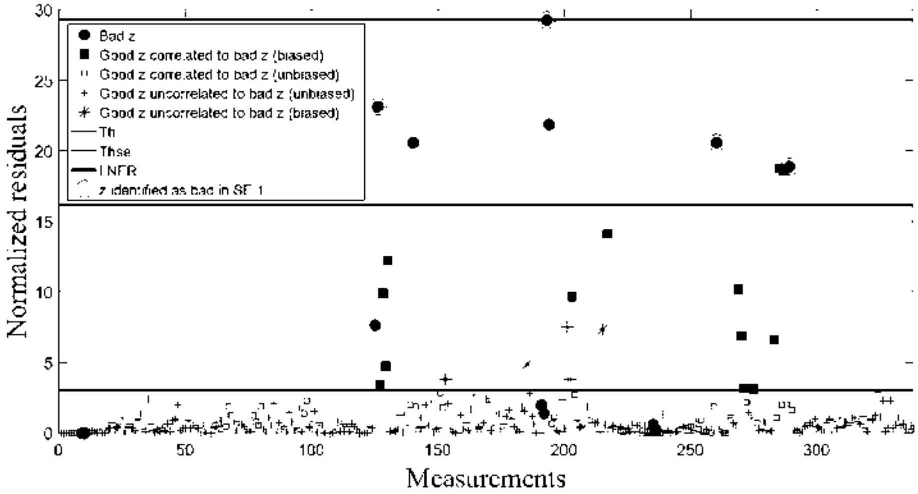

Fig. 3.4 Graphical representation of the smearing effect filtering.

x_3. Furthermore, the columns associated with the nonzero elements of this row, i.e., 1 and 3, show that measurements z_1, z_2, z_3 and z_7 are correlated to z_4.

Note that when two or more measurements with gross errors are correlated, the one with the *LNER* will be considered as a bad datum for the residuals set under analysis. The other measurements will be considered as bad data in subsequent analysis.

Lastly, all the uncorrelated measurements with gross errors in the set of IBD are corrected by subtracting their corresponding estimated residual: $z^k_{i(\text{corrected})} = z^k_i - \hat{r}^k_i \;\;, \forall\, z^k_i \in IBD^k$, if the BDA is applied at each *k*-th iteration of the estimation process. Conversely, these measurements can be corrected or eliminated from the measurement set $\boldsymbol{z}$, and another estimation process is performed by using as the initial value of $\hat{\boldsymbol{x}}$ the last obtained value of $\hat{\boldsymbol{x}}$.

3.5 Constrained AC-DC static state estimation

3.5.1 Model of inequality constraints

The physical limits of electric power system components are mathematically represented in terms of the Fischer-Burmeister in order to include them as equality constraints in the formulation of the state estimation problem. As a first step, the system's physical limits are mathematically formulated in terms of double-sided inequality constraints (DSICs), which

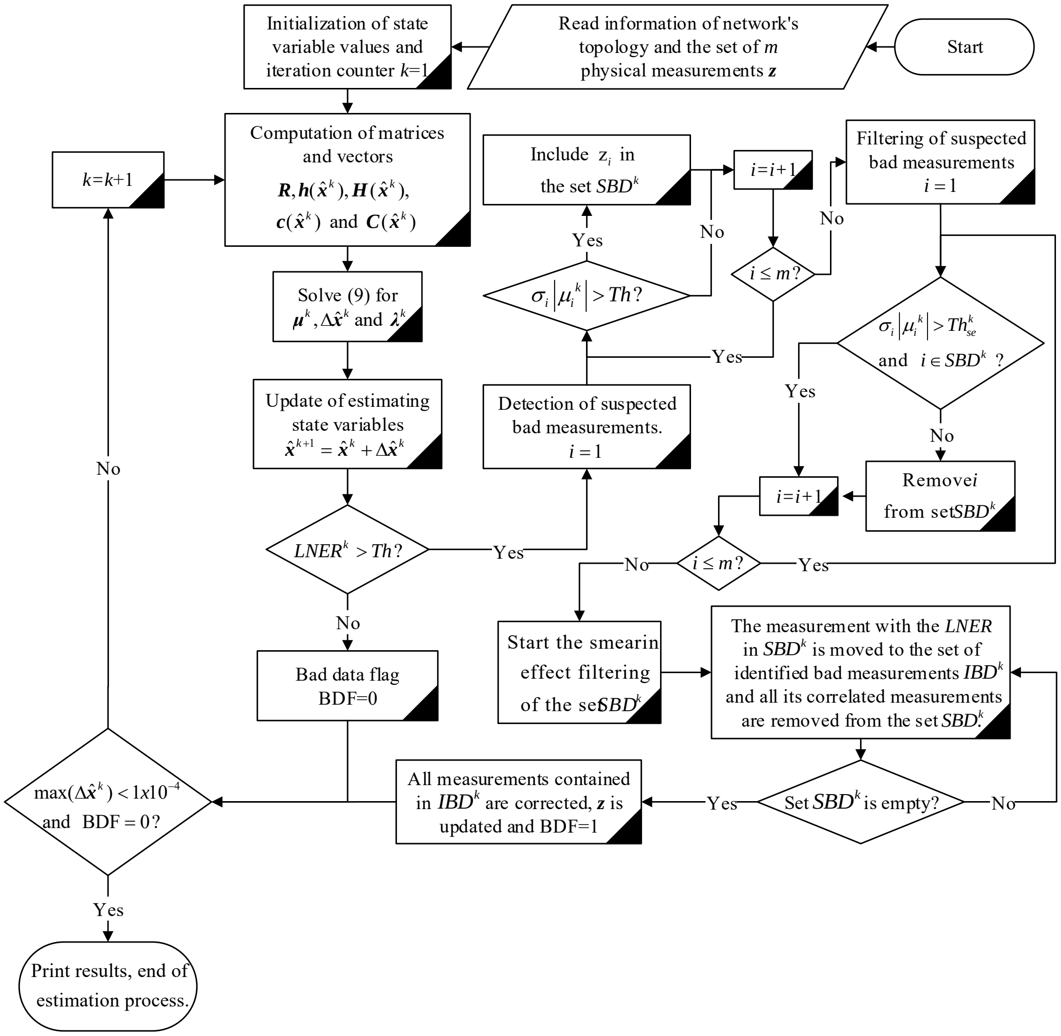

Fig. 3.5 Flowchart of the proposed iterative bad data analysis.

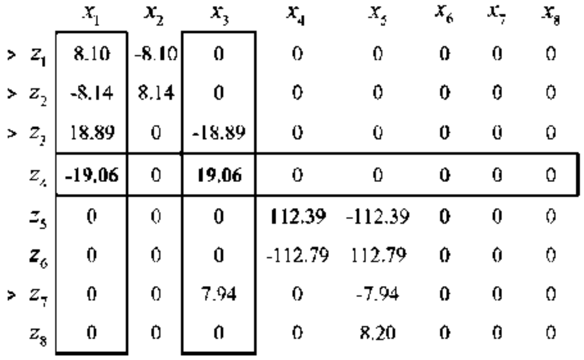

	x_1	x_2	x_3	x_4	x_5	x_6	x_7	x_8
> z_1	8.10	-8.10	0	0	0	0	0	0
> z_2	-8.14	8.14	0	0	0	0	0	0
> z_3	18.89	0	-18.89	0	0	0	0	0
z_4	-19.06	0	19.06	0	0	0	0	0
z_5	0	0	0	112.39	-112.39	0	0	0
z_6	0	0	0	-112.79	112.79	0	0	0
> z_7	0	0	7.94	0	-7.94	0	0	0
z_8	0	0	0	0	8.20	0	0	0

Fig. 3.6 Example of the measurements' correlation determination from matrix $\boldsymbol{H}$.

define the range of values that some electric variables can take without damaging equipment or steering the system towards insecure operating states.

Hence, the bound values on the *i*-th electric variable are represented by $\left\{g_i^{\min} \le g_i(\boldsymbol{x}) \le g_i^{\max}\right\}_{i=1}^{N_{ic}}$, where $g_i^{\max}$ and $g_i^{\min}$ denotes the upper and lower bounds respectively, of the constrained variable $g_i(\boldsymbol{x})$. In addition, *Nic* denotes the total number of DSICs. In a second step, the Fischer-Burmeister function $\varphi_i\left(g_i(\boldsymbol{x}), \upsilon_{g_i}\right) = 0$ is applied to transform each *i*-th DSIC to two equality constraints given by

$$\left\{\sqrt{\left(g_i^{\max} - g_i(\boldsymbol{x})\right)^2 + \left(\upsilon_{g_i}^{\max}\right)^2} - \left(g_i^{\max} - g_i(\boldsymbol{x})\right) - \left(\upsilon_{g_i}^{\max}\right) = 0\right\}_{i=1}^{Nic}, \tag{3.36}$$

$$\left\{\sqrt{\left(g_i(\boldsymbol{x}) - g_i^{\min}\right)^2 + \left(\upsilon_{g_i}^{\min}\right)^2} - \left(g_i(\boldsymbol{x}) - g_i^{\min}\right) - \left(\upsilon_{g_i}^{\min}\right) = 0\right\}_{i=1}^{Nic}. \tag{3.37}$$

In these equations, $\upsilon_{g_i}^{\max}$ and $\upsilon_{g_i}^{\min}$ are complementarity variables that must be added to the set of algebraic state variables to be estimated. The values of $\upsilon_{g_i}^{\max}$ and $\upsilon_{g_i}^{\min}$ are null if the corresponding $g_i(\boldsymbol{x})$ is within limits. If limit violations occur, $g_i(\boldsymbol{x})$ will be fixed at the offending limit during the state estimation solution process. At the optimal solution, $\upsilon_{g_i}^{\max} \ge 0$ if $g_i(\boldsymbol{x}) = g_i^{\max}$ and $\upsilon_{g_i}^{\min} \ge 0$ if $g_i(\boldsymbol{x}) = g_i^{\min}$.

The way in which $g_i(\boldsymbol{x})$ is formulated depends on the physical limits that it represents. Without a loss of generality, the physical limits considered in this proposal are the following: i) active and reactive power flows through transmission elements [Abur & Celik 1993] [Singh *et al.* 1997]; ii) the generation of active and reactive powers [Clements *et al.* 1995]; iii) nodal voltage magnitudes; iv) modulation indexes associated with the operation of voltage source converters (VSCs); and v) on-load tap changers (OLTC). Hence, $g_i(\boldsymbol{x})$ is mathematically expressed as follows.

The active power flow through the *i*-th transmission element connected between nodes *k* and *m* is given by

$$g_i^{(p)}(\boldsymbol{x}) = P_{km}(\boldsymbol{x}) = v_k^2(g_i^{sh} + g_{ij}) - v_k v_m \left(g_{ij}\cos(\theta_k - \theta_m) + b_{ij}\sin\left(\theta_k - \theta_m\right)\right), \tag{3.38}$$

where the values of g_i^{sh}, g_{ij}, b_i^{sh}, and b_{ij} are obtained from the equivalent π model of a transmission element. On the other hand, the reactive power flow through the *i*-th transmission element connected between nodes *k* and *m* is given by

$$g_i^{(q)}(\boldsymbol{x}) = Q_{km}(\boldsymbol{x}) = -v_k^2(b_i^{sh} + b_{ij}) - v_k v_m \left(g_{ij} \sin(\theta_k - \theta_m) - b_{ij} \cos\left(\theta_k - \theta_m\right)\right). \tag{3.39}$$

Similarly, the generation of active power to be injected at the *k*-th node is given by

$$g_i^{Pgen}(\boldsymbol{x}) = P_{gen}^k(\boldsymbol{x}) = P_D^k + \sum_{m \in \Omega_k} P_{km}(\boldsymbol{x}), \tag{3.40}$$

where P_D^k is the active power consumed at node *k*, while Ω_k is the set of nodes directly connected to node *k*. On the other hand, the generation of reactive power to be injected at the *k*-th node is given by

$$g_i^{Qgen}(\boldsymbol{x}) = Q_{gen}^k(\boldsymbol{x}) = Q_D^k + \sum_{m \in \Omega_k} Q_{km}(\boldsymbol{x}), \tag{3.41}$$

where Q_D^k is the reactive power consumed at node *k*.

Lastly, $g_i^{v}(\boldsymbol{x}) = v_k$, $g_i^{m_a}(\boldsymbol{x}) = m_{a,j}$ and $g_i^{T_v}(\boldsymbol{x}) = T_{v,j}$ if the voltage magnitude at node *k*, the *j*-th VSC modulation index and the *j*-th OLTC value are kept within specified limits, respectively.

3.5.2 State estimation problem with inequality constraints

In general, the state estimation problem can be mathematically formulated as a generic optimization problem given by

$$\begin{aligned} &\min_{\boldsymbol{x} \in \mathbb{R}^{n_{sv}}} J(\boldsymbol{x}) \\ &\textit{subject to} \quad \boldsymbol{x} \in \boldsymbol{X} \subseteq \mathbb{R}^{n_{sv}} \end{aligned}, \tag{3.42}$$

where $J(\boldsymbol{x}) : \mathbb{R}^{n_{sv}} \to \mathbb{R}$ is a scalar error function to be minimized with respect to the algebraic state variables to be estimated. The set $\boldsymbol{X} \subseteq \mathbb{R}^{n_{sv}}$ represents the feasible region of the problem, and n_{sv} is the number of algebraic state variables. If a mixture of *Nec* equality and *Nic* inequality constraint functions are included in the formulation, the feasibility region is defined as the set of algebraic state variables that simultaneously satisfy all the constraints:

$$\boldsymbol{X} = \left\{ \boldsymbol{x} \in \mathbb{R}^{n_{sv}} : \left\{ c_i(\boldsymbol{x}) = 0 \right\}_{i=1}^{Nec}, \left\{ g_i^{\min} \leq g_i(\boldsymbol{x}) \leq g_i^{\max} \right\}_{i=1}^{N_{ic}} \right\} . \tag{3.43}$$

This generic optimization problem can be reformulated based on the theoretical concepts described in Section 2.8.1 such that the set of inequality constraints $\left\{ g_i^{\min} \leq g_i(\boldsymbol{x}) \leq g_i^{\max} \right\}_{i=1}^{N_{ic}}$ is transformed into a set of nonlinear equality constraints given by the Fischer-Burmeister function $\left\{ \varphi_i\left(g_i(\boldsymbol{x}), \upsilon_{g_i} \right) = 0 \right\}_{i=1}^{2Nic}$. This transformation results in the equality constrained nonlinear optimization problem given by

$$\begin{aligned} &\min_{\boldsymbol{x} \in \mathbb{R}^{n_{sv}}} J(\boldsymbol{x}) \\ &\textit{subject to } \ \boldsymbol{x} \in \boldsymbol{X} \subseteq \mathbb{R}^{n_{sv}}, \ \boldsymbol{X} = \left\{ \boldsymbol{x} \in \mathbb{R}^{n_{sv}} : \left\{ c_i(\boldsymbol{x}) = 0 \right\}_{i=1}^{Nec}, \left\{ \varphi_i\left(g_i(\boldsymbol{x}), \upsilon_{g_i} \right) = 0 \right\}_{i=1}^{2Nic} \right\} \end{aligned} . \tag{3.44}$$

The way in which the scalar error function $J(\boldsymbol{x})$ is defined depends on the estimator to be employed. Hence, if $J(\boldsymbol{x})$ is defined as the sum of all weighted squared measurement errors, the optimization problem (3.44) corresponds to the formulation of the state estimation approach most commonly used in control centers, i.e., the equality-constrained WLS state estimator, where all inequality constraints are explicitly considered. Lastly, since the mathematical formulation of the estimation problem remains unaltered with the inclusion of inequality constraints, the traditional numerical methods normally applied for solving (3.44) remains the same, as demonstrated in the next section.

3.5.3 Hachtel’s augmented matrix method

A variety of methods can be used for solving the equality-constrained WLS state estimation problem given by (3.44). Among them, Hachtel’s augmented matrix method has shown very good compromise between numerical stability and computational efficiency [Gjelsvik *et al.* 1985] and is the one used in this proposal. In matrix notation, the constrained WLS state estimation problem (3.44) is formulated as follows:

$$\begin{aligned} &\arg\min_{\boldsymbol{x}_{ext}, \boldsymbol{r}} \ J(\boldsymbol{x}_{ext}) = \frac{1}{2} \boldsymbol{r}^{\mathrm{T}} \boldsymbol{W} \boldsymbol{r} \\ &\textit{subject to} \quad \boldsymbol{c}_{ext}(\boldsymbol{x}_{ext}) = \boldsymbol{0} \ , \\ &\qquad \boldsymbol{r} - \boldsymbol{z} + \boldsymbol{h}(\boldsymbol{x}_{ext}) = \boldsymbol{0} \end{aligned} \tag{3.45}$$

where $\boldsymbol{x}_{ext}$ and $\boldsymbol{r}$ denote the vectors of decision variables. In other words, the residuals $\left\{r_i\right\}_{i=1}^{M}$ are considered explicit decision variables along with

$$\boldsymbol{x}_{ext} = \left[\boldsymbol{x}, \left\{\upsilon_{g_i}^{\max}\right\}_{i=1}^{Nic}, \left\{\upsilon_{g_i}^{\min}\right\}_{i=1}^{Nic}\right]^{\mathrm{T}} \in \mathbb{R}^{(n_{sv}+2Nic)}. \tag{3.46}$$

The residuals are weighted by the matrix $\boldsymbol{W} = diag\left\{1/\sigma_i^2\right\}_{i=1}^{M}$, where the standard deviation σ_i of the measurement *i* reflects the expected accuracy of the corresponding meter. The first set of equality constraints in (3.45) are given by

$$\boldsymbol{c}_{ext}(\boldsymbol{x}_{ext}) = \left[\underbrace{\left\{c_i(\boldsymbol{x})\right\}_{i=1}^{Nec}}_{\boldsymbol{c}(\boldsymbol{x})}, \underbrace{\left\{\varphi_i\left(g_i(\boldsymbol{x}), \upsilon_{g_i}\right)\right\}_{i=1}^{2Nic}}_{\boldsymbol{\varphi}(\boldsymbol{x}_{ext})}\right]^{\mathrm{T}} = \boldsymbol{0}, \tag{3.47}$$

where $\boldsymbol{c}(\boldsymbol{x})$ is composed of the set of virtual measurements. Lastly, the second set of equality constraints are associated with the measurement residual definition.

The Lagrangian method is used for solving (3.45) based on the Lagrangian function

$$\mathcal{L} = J(\boldsymbol{x}_{ext}) - \boldsymbol{\lambda}^{\mathrm{T}}\boldsymbol{c}_{ext}(\boldsymbol{x}_{ext}) - \boldsymbol{\mu}^{\mathrm{T}}\left(\boldsymbol{r} - \boldsymbol{z} + \boldsymbol{h}(\boldsymbol{x}_{ext})\right), \tag{3.48}$$

where $\boldsymbol{\lambda}$ and $\boldsymbol{\mu}$ are Lagrange multipliers.

After deriving the four sets of equations associated with the first-order optimality conditions, replacing $\boldsymbol{r} = \boldsymbol{W}^{-1}\boldsymbol{\mu}$ and linearizing the resulting three sets of equations by the Gauss-Newton method with respect to $\boldsymbol{x}_{ext}$, the sparse, symmetric set of equations

$$\left.\begin{bmatrix} \boldsymbol{W}^{-1} & \boldsymbol{H} & \boldsymbol{0} \\ \boldsymbol{H}^{\mathrm{T}} & \boldsymbol{0} & \boldsymbol{C}^{\mathrm{T}} \\ \boldsymbol{0} & \boldsymbol{C} & \boldsymbol{0} \end{bmatrix}\right|_{\boldsymbol{x}_{ext}^{k-1}} \begin{bmatrix} \boldsymbol{\mu}^k \\ \Delta\boldsymbol{x}_{ext} \\ \boldsymbol{\lambda}^k \end{bmatrix} = \begin{bmatrix} \boldsymbol{z} - \boldsymbol{h}\left(\boldsymbol{x}_{ext}^{k-1}\right) \\ \boldsymbol{0} \\ -\boldsymbol{c}_{ext}\left(\boldsymbol{x}_{ext}^{k-1}\right) \end{bmatrix}, \tag{3.49}$$

are obtained for the *k*-th iteration of the solution process. In this case, $\boldsymbol{H}$ and $\boldsymbol{C}$ are the Jacobian matrices of $\boldsymbol{h}$ and $\boldsymbol{c}_{ext}$, respectively, with respect to $\boldsymbol{x}_{ext}$.

The adjustments $\Delta\boldsymbol{x}_{ext}$ obtained at the *k*-th iteration are used to obtain new values of algebraic state variables: $\boldsymbol{x}_{ext}^{k} = \boldsymbol{x}_{ext}^{k-1} + \Delta\boldsymbol{x}_{ext}$. This iterative process is repeated until an acceptable tolerance $\operatorname{Max}\left|\left\{x_{ext,i}^{k}\right\}_{i=1}^{n_{sv}+2Nic}\right| \leq TOL$ is achieved or the maximum number of iterations has been exceeded.

3.6 Conclusions

A Hachtel-based SE approach has been proposed to assess the operating state of an arbitrary number of interconnected AC and MTDC networks. DC-DC converters have also been considered in order to include in the formulation integrated DC networks operating at different voltage levels or interconnecting monopolar and bipolar DC grids. In contrast to other proposals, the controllable parameters of the VSCs and OLTC transformers composing the AC-DC interfaces, as well as the duty cycle of DC-DC converters, are simultaneously estimated along with the nodal voltages at the AC and DC networks.

This iterative estimation process is performed based on measurements provided by a SCADA system and PMUs without altering the level of measurement redundancy. To achieve this goal, the estimated residual provided by the Hachtel method is used in a proposed multiple bad data analysis to detect, identify and correct bad data at each iteration of the estimation process. In this context, the smearing effect has been taken into account to detect the set of state variables affected by measurements with gross errors, which is of relevance because these states have in turn a direct effect on the estimated residual of other measurements that could be erroneously identified as bad data. Hence, this analysis allows that measurements suspected of being erroneous because of the smearing effect not to be identified as bad data.

Lastly, a new approach for including inequality constraints in a rather straightforward manner in equality-constrained WLS-based state estimators is proposed in this chapter. Based on the concepts of complementarity constraints and merit functions, the inequality constraints are transformed into nonlinear algebraic equations that are directly included in the set of constraints associated with the original formulation of these kinds of estimators. Hence, the mathematical formulation and standard mathematical techniques currently applied to solving equality-constrained WLS-based state estimators, which are the ones used in control centers, remain unaltered.

Chapter 4

4 Case Studies for Static State Estimation

4.1 Introduction

In this chapter, the effectiveness of the proposed formulations described in chapter 3 is demonstrated by estimating the operating state of different electric networks. Firstly, the static state estimation of AC-DC networks based on the formulation reported in Section 3.3 is detailed. Secondly, the application of the bad data analysis approaches described in Section 3.4 for detecting, identifying and correcting/eliminating multiple measurements under Gaussian and non-Gaussian errors are presented by numerical examples. The bad data analysis is performed through Monte Carlo simulations and the results obtained by the proposed approach are compared with classical and Robust BDA methods. Finally, case studies are presented to show the applicability of the inequality constrained SE formulation detailed in Section 3.5.

4.2 AC-DC static state estimation

The effectiveness of the proposed method of Section 3.3 is demonstrated by estimating the operating state of a multi-terminal AC-DC network. The set of measurements employed for the estimates is obtained from a custom-made AC-DC power flow (PF) program based on the proposal of Section 2.9 using the control parameters reported in [Vrana *et al*. 2013] and ensures the system's observability. Furthermore, these measurements are associated with those that will be provided by a SCADA system and PMUs. At least one voltage synchrophasor measurement is included in each AC system to have a voltage phase angular reference. PMUs are placed at the VSC stations to measure the currents through the phase reactors. Finally, the standard deviations used to represent the noise in these types of measurements are as follows [Zamora-Cárdenas *et al*. 2016]: $\sigma_{V}^{SCADA} = 0.004$, $\sigma_{P,Q.inj}^{SCADA} = 0.010$, $\sigma_{P,Q.branch}^{SCADA} = 0.008$, $\sigma_{V}^{PMU} = 0.002$, $\sigma_{\theta_V}^{PMU} = 0.0017$, $\sigma_{Ireal}^{PMU} = 0.002$ and $\sigma_{Iimag}^{PMU} = 0.002$.

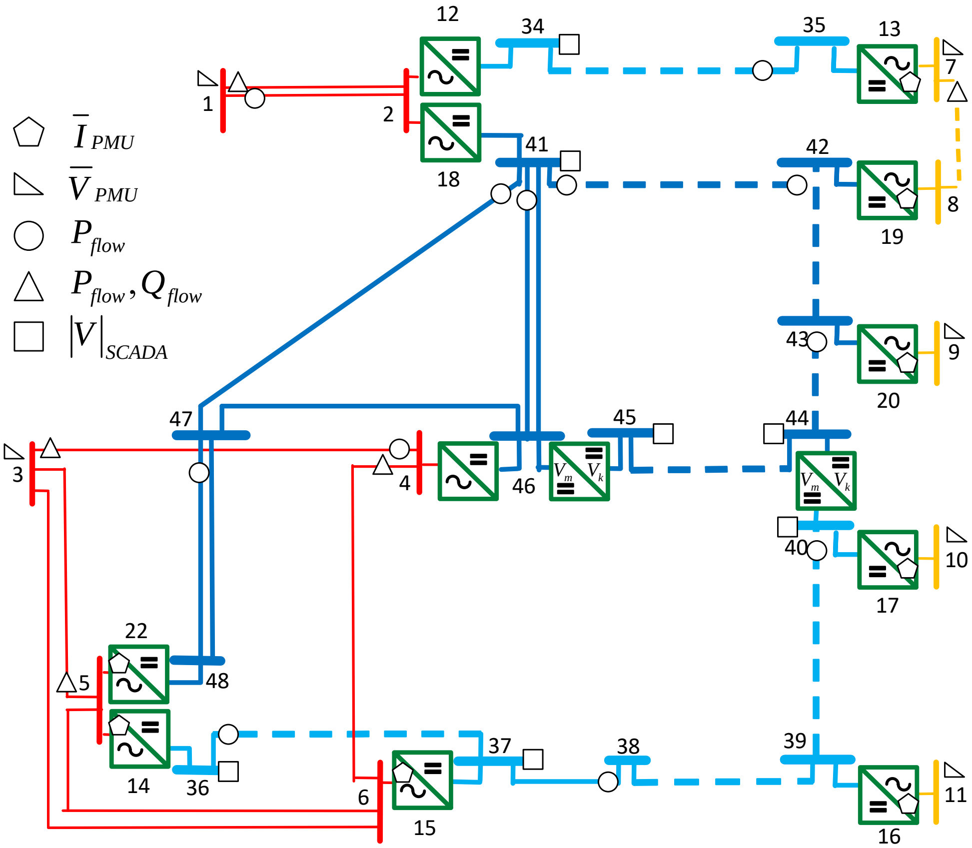

Fig. 4.1 Measurement placement in CIGRE test system for SE

The CIGRE test system [Vrana *et al.* 2013] is shown in Fig. 4.1 together with the location of the measurements used to perform the SE. This system is detailed in Section 2.10.

The system parameters are given in [Vrana *et al.* 2013] but those corresponding to AC–DC converters, except the nominal power, have been replaced by the following data corresponding to the VSC-based AC–DC station model detailed in Section 2.3: $\bar{\mathbf{Y}}_T = -j100$, $\bar{\mathbf{Y}}_{sf} = j0.05$, $\bar{\mathbf{Y}}_{pr} = -j100$ and $R_1 = 0.0004$.

Based on the 153 measurements considered for the study, The SE converged in five iterations to a tolerance of 10^{-4} with a final value of the objective function of 0.348. After comparing the results of the 105 estimated state variables with respect to their corresponding values obtained from the PF study, the higher absolute error was for the modulation index of the VSC converter between nodes 2 and 34, with SE value of 0.8229 and a PF value of 0.8234. A comparison of the SE and PF values for the 105 state variables is presented in Table 4.1 and Table 4.2.

Table 4.1 Bus voltage comparison between SE and PF solution.

Bus	***$|V|$ SE***	***$|V|$ PF***	***θ SE***	***θ PF***	***Bus***	***$|V|$ SE***	***$|V|$ PF***	***θ SE***	***θ PF***
AC 1	1.0001	1.0000	0.0000	0.0000	AC 25	0.9995	0.9999	11.7326	11.7353
AC 2	0.9999	0.9999	-21.9362	-21.9372	AC 26	1.0001	1.0002	6.2413	6.2475
AC 3	1.0002	1.0000	0.0076	0.0000	AC 27	1.0002	1.0000	0.0056	0.0000
AC 4	1.0002	1.0000	12.6779	12.6834	AC 28	0.9999	1.0000	0.0147	0.0000
AC 5	1.0003	1.0000	11.8100	11.8128	AC 29	1.0017	1.0016	-23.2015	-23.2029
AC 6	1.0004	1.0000	5.7413	5.7474	AC 30	1.0005	1.0004	-4.2300	-4.2174
AC 7	1.0001	1.0000	0.2286	0.2472	AC 31	1.0001	1.0000	-0.0108	0.0000
AC 8	1.0001	1.0000	-3.8487	-3.8360	AC 32	1.0005	1.0003	13.6154	13.6212
AC 9	1.0000	1.0000	0.6194	0.6303	AC 33	1.0002	1.0003	12.8724	12.8751
AC 10	0.9999	1.0000	-0.0483	-0.0630	DC 34	1.0001	1.0000	-	-
AC 11	0.9999	1.0000	0.3207	0.3151	DC 35	1.0092	1.0091	-	-
AC 12	0.9995	0.9999	-21.9143	-21.9153	DC 36	0.9902	0.9900	-	-
AC 13	1.0002	1.0000	0.2061	0.2247	DC 37	0.9872	0.9871	-	-
AC 14	0.9995	1.0000	11.8030	11.8057	DC 38	0.9987	0.9985	-	-
AC 15	0.9999	1.0000	5.7867	5.7929	DC 39	1.0068	1.0067	-	-
AC 16	1.0002	1.0000	0.2920	0.2865	DC 40	1.0115	1.0114	-	-
AC 17	0.9999	1.0000	-0.0426	-0.0573	DC 41	1.0101	1.0100	-	-
AC 18	1.0001	1.0000	-22.0514	-22.0524	DC 42	1.0140	1.0139	-	-
AC 19	1.0001	1.0000	-3.8833	-3.8707	DC 43	1.0144	1.0146	-	-
AC 20	1.0001	1.0000	0.5621	0.5730	DC 44	1.0090	1.0092	-	-
AC 21	1.0002	1.0000	12.7631	12.7687	DC 45	1.0053	1.0056	-	-
AC 22	0.9999	1.0000	11.9066	11.9094	DC 46	0.9983	0.9982	-	-
AC 23	0.9994	0.9998	-21.6950	-21.6963	DC 47	0.9929	0.9927	-	-
AC 24	0.9999	0.9996	-0.0185	0.0000	DC 48	0.9836	0.9835	-	-

Table 4.2 Taps, modulation indexes and duty cycles, SE vs PF comparison.

HVDC	***T_v SE***	***T_v PF***	***m_a SE***	***m_a PF***	***DC-DC***	***D SE***	***D PF***
1	1.0004	1.0000	0.8198	0.8202	1	0.9966	0.9962
2	0.9999	1.0000	0.8049	0.8048	2	1.0060	1.0057
3	1.0008	1.0000	0.8229	0.8234			
4	1.0004	1.0000	0.8326	0.8328			
5	0.9997	1.0000	0.8061	0.8060			
6	1.0000	1.0000	0.8111	0.8113			
7	0.9999	1.0000	0.8029	0.8029			
8	1.0000	1.0000	0.7995	0.7995			
9	0.9999	1.0000	0.8000	0.7998			
10	1.0000	1.0000	0.8234	0.8233			
11	1.0004	1.0000	0.8361	0.8363			

4.3 BDA analysis

4.3.1 Statistical analysis of the proposed methods

In this section, the IEEE 14-bus test system is used for the statistical analysis of the LNER-based BDA reported in [Martínez-Parrales & Fuerte-Esquivel 2018] and detailed in Section 3.4. In this case, 37 branch power flow measurements and three nodal voltage phasor measurements are considered for the studies assuming errors with and without a Gaussian distribution. A statistical comparison of the obtained results with respect to the ones given by other proposals of bad data analysis is also reported.

4.3.1.1 Generation of the measurements' errors

To create enough statistics, five databases of 5000 errors per measurement are generated. These errors are added to the true measurements obtained from a power flow study: $z_i^{phy} = z_i^{true} + \varepsilon_i, \forall i = 1,...,m$. The errors in all databases are generated considering a zero mean and a variance of σ^2 according to the type of measurement to make a fair statistical comparison. The standard deviations σ associated with the SCADA branch power flows are 0.008, while the ones associated with the PMU voltage magnitudes and angles are 0.002 and 0.0017, respectively [Alcaide-Moreno B. A. *et al*. 2015].

The first database is generated following a Gaussian distribution. The histogram associated with the errors generated for the active power flow measurement from node 1 to node 2 $e_{P1,2}$ is shown in Fig. 4.2. The second database is composed of errors that are generated with a Gaussian mixture distribution of two Gaussian components. The error's components of the *i*-th measurement are represented with means of $-0.5\sigma_i$ and $2\sigma_i$, with standard deviations of $0.7\sigma_i$ and $1.3\sigma_i$ and with weights of 0.7 and 0.3, respectively, as shown in Fig. 4.3 for $e_{P1,2}$. A Laplace distribution with a zero mean and a scale parameter σ_i is used to generate the third database of errors, as shown in Fig. 4.4. The fourth database is composed of random errors with zero mean and $\pm\sqrt{3}\sigma_i$ limits, as shown in Fig. 4.5. Lastly, the fifth database of errors is generated following a Weibull distribution with shape parameter value of 1.5, as shown in Fig. 4.6.

Note that the vertical lines placed in ± 0.024 in Fig. 4.2 to Fig. 4.6 represent the $\pm 3\sigma_{P1,2}$ limits for $e_{P1,2}$; this implies that when the generated error is outside those limits its corresponding measurement will be considered as a bad datum. Lastly, and in order to show how those error distributions deviated from a truly Gaussian distribution, the red line shown in Fig. 4.3 to Fig. 4.6 represents the Gaussian distribution error reported in Fig. 4.2.

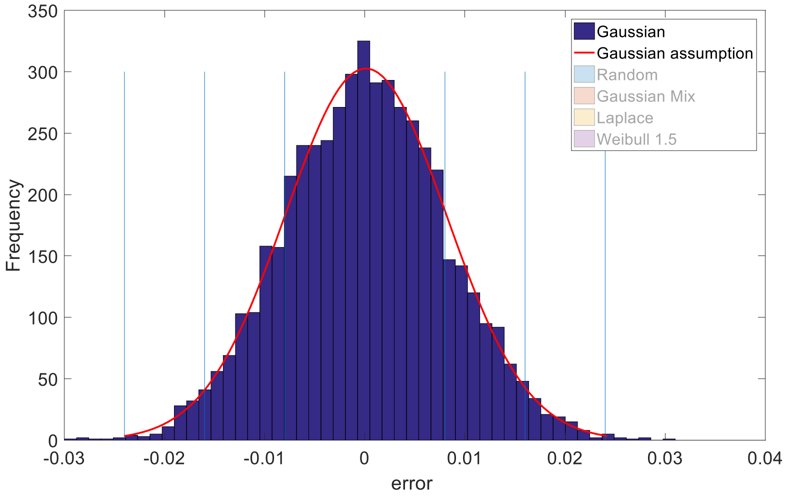

Fig. 4.2 Histogram of database 1 for $e_{P1,2}$

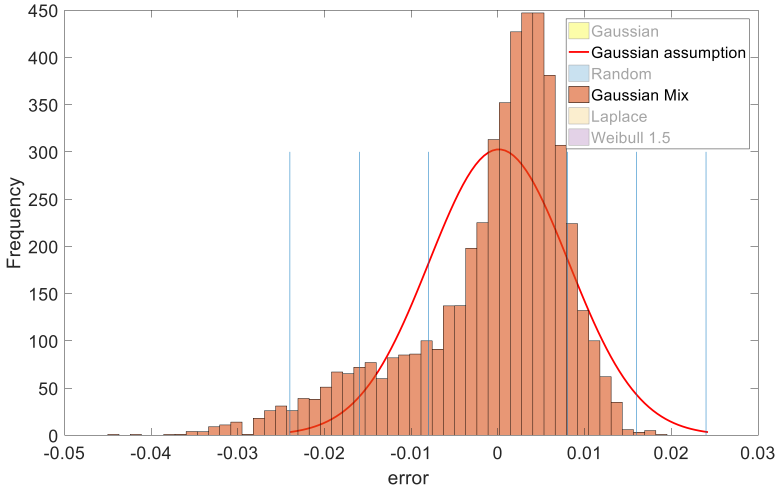

Fig. 4.3 Histogram of database 2 for $e_{P1,2}$

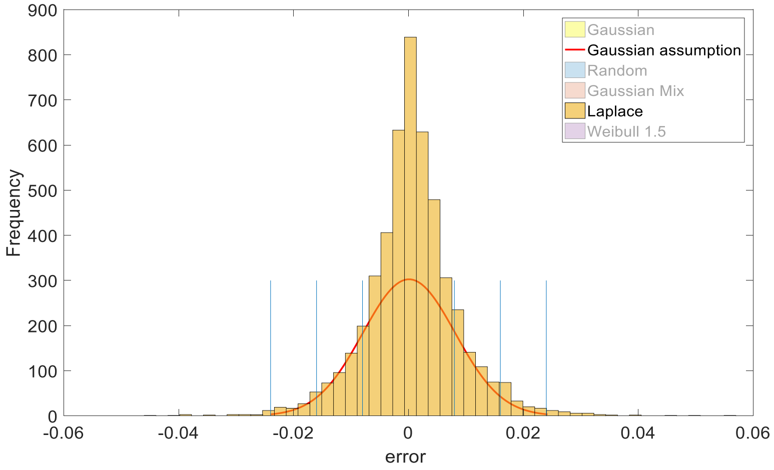

Fig. 4.4 Histogram of database 3 for eP1,2

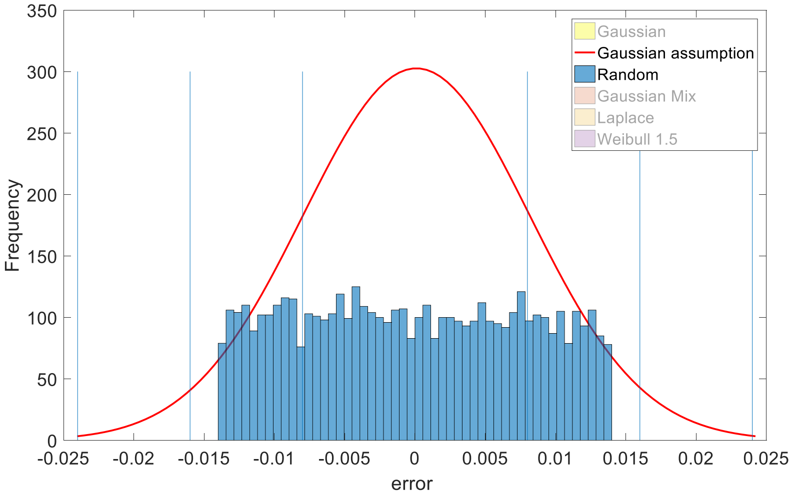

Fig. 4.5 Histogram of database 4 for $e_{P1,2}$

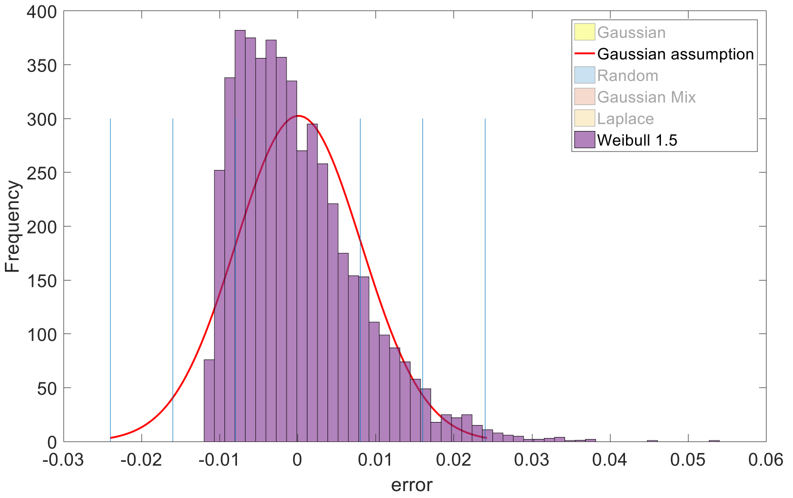

Fig. 4.6 Histogram of database 5 for $e_{P1,2}$

4.3.1.2 Statistical analysis of the proposed bad data analysis

The performance of the bad data analysis methods is statistically analyzed in this section. To achieve this goal, the true measurement of active power flowing from node 1 to 5 is corrupted by adding a specific gross error. This gross error is expressed in terms of the measurement's standard deviation, i.e. $e_{BD} = \beta\sigma_{P_{1-5}}$, and the corresponding bad data measurement is referred to as z_{BD}. The errors of the rest of measurements are as reported in Section 4.3.1.1.

Based on the information mentioned above and the five generated databases of errors described in Section 4.3.1.1, the Monte Carlo method is applied to perform 5000 SE studies per database to statistically assess how each LNER-based BDA detailed in Section 3.4 behaves according to how the errors are distributed. The application of this BDA during or after the state estimation process is referred to as BDA 1 or BDA 2, respectively.

The same experiment is performed using four other BDA methods for comparison, which are applied after the operating state has been estimated. In all these methods the identified bad data are eliminated from the measurements' database before performing another state estimation process. This sequential process of solution is repeated until no bad data are identified. The method BDA 3 is based on the largest normalized estimated residual test (LNERT), where all measurements with their LNER bigger than *Th* are considered bad data. Note that in this method none of the proposed filtering processes is applied. The other method referred to as BDA 4 is similar to BDA 3 but uses the LNRT instead of the LNERT. In this case, the calculated residuals $\boldsymbol{r} = \boldsymbol{z} - \boldsymbol{h}(\hat{\boldsymbol{x}})$ are normalized with respect to the square root of the diagonal elements of the residuals' covariance matrix $\boldsymbol{\Omega} = \boldsymbol{R}\boldsymbol{A}_1\boldsymbol{R}$: $|r_i| / \sqrt{\Omega_{ii}}$, $\forall i = 1, \ldots, m$. This matrix is calculated as reported in [Wu *et al.* 1988], with the submatrix $\boldsymbol{A}_1$ obtained from

$$\begin{pmatrix} \boldsymbol{R} & \boldsymbol{H}(\hat{\boldsymbol{x}}) & \boldsymbol{0} \\ \boldsymbol{H}(\hat{\boldsymbol{x}})^{\mathrm{T}} & \boldsymbol{0} & \boldsymbol{C}(\hat{\boldsymbol{x}})^{\mathrm{T}} \\ \boldsymbol{0} & \boldsymbol{C}(\hat{\boldsymbol{x}}) & \boldsymbol{0} \end{pmatrix}^{-1} = \begin{pmatrix} \boldsymbol{A}_1 & \boldsymbol{A}_2 & \boldsymbol{A}_3 \\ \boldsymbol{A}_2^{\mathrm{T}} & \boldsymbol{A}_4 & \boldsymbol{A}_5 \\ \boldsymbol{A}_3^{\mathrm{T}} & \boldsymbol{A}_5^{\mathrm{T}} & \boldsymbol{A}_6 \end{pmatrix}. \tag{4.1}$$

In order to have a robust state estimation, the method BDA 4 is extended by computing the projection statistics assuming that the evaluation of the weighted Jacobian matrix considering a flat start of nodal voltages is valid for the entire estimation process [Mili *et al.* 1996]. This robust BDA is called BDA 5. Lastly, the projection statistics are calculated based on the nodal voltages estimated at the second iteration of the state estimation process to provide a robust state estimator named BDA 6.

Based on the information mentioned above, the number of studies in which z_{BD} is correctly detected and identified by the six BDA methods, for different values of β within the interval [2, 72] and *Th*=3, is reported in Table 4.3. Note that when $\beta = 2$, z_{BD} is free of gross error.

Table 4.3 Comparison between BDA methods for different βs

BDA Method	Detected errors	β							
		2	4	5	6	7	8	24	72
Gaussian distributed errors									
BDA 1	z_{BD}/**other *z***	5/**20**	2488/**26**	4741/**20**	4998/**18**	5000/**20**	5000/**20**	5000/**18**	5000/**21**
BDA 2	z_{BD}/**other *z***	5/**20**	2489/**25**	4742/**20**	4998/**19**	5000/**16**	5000/**15**	5000/**14**	5000/**14**
BDA 3	z_{BD}/**other *z***	5/**20**	2488/**24**	4742/**17**	4998/**15**	5000/**14**	5000/**14**	5000/**14**	5000/**14**
BDA 4	z_{BD}/**other *z***	12/**1023**	1977/**2838**	2968/**2401**	3511/**1922**	4000/**1600**	4494/**1226**	5000/**369**	5000/**370**
BDA 5	z_{BD}/**other *z***	22/**697**	3490/**963**	4570/**685**	4800/**494**	4898/**402**	4946/**357**	5000/**317**	5000/**317**
BDA 6	z_{BD}/**other *z***	6/**844**	1356/**3296**	2184/**3017**	2702/**2562**	3252/**2173**	3856/**1831**	5000/**205**	5000/**204**
Gaussian mixture distributed errors									
BDA 1	z_{BD}/**other *z***	14/**169**	2394/**181**	4709/**165**	4996/**155**	5000/**158**	5000/**158**	5000/**150**	5000/**173**
BDA 2	z_{BD}/**other *z***	14/**169**	2394/**182**	4708/**170**	4994/**154**	5000/**152**	5000/**152**	5000/**152**	5000/**152**
BDA 3	z_{BD}/**other *z***	14/**169**	2393/**181**	4706/**169**	4994/**152**	5000/**152**	5000/**152**	5000/**152**	5000/**152**
BDA 4	z_{BD}/**other *z***	35/**1985**	2022/**3509**	3045/**3192**	3593/**2765**	4061/**2427**	4505/**2080**	5000/**1222**	5000/**1204**
BDA 5	z_{BD}/**other *z***	63/**1559**	3364/**1705**	4550/**1444**	4791/**1276**	4892/**1171**	4949/**1117**	5000/**1074**	5000/**1061**
BDA 6	z_{BD}/**other *z***	26/**1445**	1441/**3613**	2282/**3415**	2781/**3021**	3252/**2700**	3832/**2358**	5000/**731**	5000/**730**
Laplace distributed errors									
BDA 1	z_{BD}/**other *z***	3/**183**	2294/**196**	4777/**177**	4992/**173**	4998/**172**	5000/**177**	5000/**168**	5000/**190**
BDA 2	z_{BD}/**other *z***	3/**182**	2294/**196**	4775/**176**	4991/**165**	4998/**160**	5000/**157**	5000/**156**	5000/**156**
BDA 3	z_{BD}/**other *z***	3/**182**	2289/**189**	4772/**168**	4990/**159**	4998/**156**	5000/**156**	5000/**156**	5000/**156**
BDA 4	z_{BD}/**other *z***	10/**1393**	2017/**3185**	2935/**2863**	3515/**2400**	4058/**1960**	4515/**1627**	5000/**841**	5000/**826**
BDA 5	z_{BD}/**other *z***	19/**1159**	3512/**1314**	4573/**1098**	4778/**940**	4892/**838**	4941/**799**	5000/**752**	5000/**747**
BDA 6	z_{BD}/**other *z***	7/**1084**	1304/**3627**	2127/**3382**	2674/**2902**	3231/**2501**	3830/**2165**	5000/**539**	5000/**540**
Random distributed errors									
BDA 1	z_{BD}/**other *z***	0/**0**	2395/**3**	4768/**2**	5000/**0**	5000/**0**	5000/**0**	5000/**0**	5000/**0**
BDA 2	z_{BD}/**other *z***	0/**0**	2395/**3**	4768/**2**	5000/**0**	5000/**0**	5000/**0**	5000/**0**	5000/**0**
BDA 3	z_{BD}/**other *z***	0/**0**	2395/**3**	4768/**2**	5000/**0**	5000/**0**	5000/**0**	5000/**0**	5000/**0**
BDA 4	z_{BD}/**other *z***	5/**812**	2047/**2552**	3038/**2142**	3524/**1718**	4007/**1389**	4473/**1031**	5000/**125**	5000/**122**
BDA 5	z_{BD}/**other *z***	15/**517**	3507/**710**	4597/**471**	4801/**282**	4900/**185**	4955/**133**	5000/**89**	5000/**88**
BDA 6	z_{BD}/**other *z***	4/**690**	1430/**3080**	2253/**2821**	2726/**2404**	3250/**2002**	3837/**1693**	5000/**44**	5000/**43**
Weibull distributed errors									
BDA 1	z_{BD}/**other *z***	0/**80**	2535/**79**	4716/**86**	4993/**77**	5000/**77**	5000/**75**	5000/**76**	5000/**82**
BDA 2	z_{BD}/**other *z***	0/**80**	2536/**78**	4716/**86**	4993/**82**	5000/**82**	5000/**82**	5000/**82**	5000/**82**
BDA 3	z_{BD}/**other *z***	0/**80**	2536/**78**	4716/**85**	4993/**82**	5000/**82**	5000/**82**	5000/**82**	5000/**82**
BDA 4	z_{BD}/**other *z***	0/**1147**	2062/**2898**	3015/**2521**	3606/**2023**	4113/**1641**	4528/**1362**	5000/**573**	5000/**563**
BDA 5	z_{BD}/**other *z***	7/**862**	3573/**1130**	4546/**869**	4773/**705**	4877/**615**	4939/**556**	5000/**503**	5000/**504**
BDA 6	z_{BD}/**other *z***	0/**903**	1366/**3408**	2134/**3175**	2686/**2723**	3284/**2280**	3906/**1922**	5000/**349**	5000/**351**

The number of correct identifications of z_{BD} as a bad datum is similar for all LNERT-based BDA methods for all values of β. Note that these three methods use the normalized estimated residuals: $|\hat{r}_i|/\sigma_i > Th$,$\forall i = 1,\ldots,m$. In these three methods, the error in z_{BD} with a magnitude of 4σ is detected less than half of the time. This implies that the z_{BD} together with its correlated measurements is capable of biasing the estimates $\hat{\boldsymbol{x}}$ enough to reduce the z_{BD}

estimated residual's magnitude to less than 3σ in more than half of the occurrences. Lastly, as the error in z_{BD} increases, the number of successful detections improves.

The number of times that another measurement is identified as a bad datum is also similar for the first three methods. This occurs between 14 and 26 times for the Gaussian distribution, between 152 and 182 times for the Gaussian mixture distribution, between 156 and 196 times for the Laplace distribution, between 0 and 3 times for the random distribution and between 75 and 86 times in Weibull distribution. Some of these detections are correct, however, because some of the randomly generated errors are greater than 3σ, as shown in Fig. 4.2 to Fig. 4.6.

On the other hand, both the classical and robust BDAs based on the LNRT present a poor performance compared with the other three methods, requiring a higher value of β to correctly identify z_{BD} as a bad datum in each one of the SE simulations. Furthermore, there is a significant difference in the number of uncorrupted measurements that have been detected and identified with gross errors. In these cases, the normalized residuals introduce a high masking effect that causes too many good measurements to be incorrectly identified as bad data.

4.3.1.3 Quality of the estimates

The difference between the true value of a state variable and the set of its estimated values through the Monte Carlo simulations is referred to as the error of estimated variables (EEV). The variance of each EEV is calculated as the mean squared error (MSE) given by $MSE_i = \frac{1}{5000}\sum_{mc=1}^{5000}\left(x_i - \hat{x}_{i,mc}\right)^2 \ ,\forall i = 1,...,n$. Note that the true values of $\boldsymbol{x}$ are obtained from a power flow study from which the set of perfect physical measurements were generated.

Two quality indicators are calculated to quantify the accuracy of the estimates for the five types of generated errors. The first quality indicator κ concerns the maximum MSE, $\kappa = \max\left\{MSE\right\}$, and represents the variance of the worst estimated state variable. On the other hand, the second quality indicator ρ is computed as the average of all MSE values, i.e. $\rho = \frac{1}{n}\sum_{i=1}^{n} MSE_i$, and represents the average of the variances of the estimates. Note that lower values of κ and ρ indicate a higher quality of the estimates.

The quality of the estimates obtained from the Monte Carlo simulations described in Section 4.3.1.2 is reported in Table 4.4, where the quality indicators are expressed in 1x10^{-6}. When $\beta = 2$, the measurement z_{BD} is free of gross error such that the quality indicators associated with these case studies can be used as references to measure the quality of estimates when z_{BD} contains a gross error. In this context, note that the values of κ and ρ are similar and almost constant for all values of β in the estimations based on the LNERT-based state estimators, independently of the types of probability distributions considered for the randomly generated errors.

On the other hand, the values of κ and ρ are much higher for the robust BDAs than the ones related to the other BDA methods, which leads to less accurate estimations. The reason for these results is directly related to the misidentification of too many good measurements as incorrect data, as indicated in Table 4.3, and the incorrect projection statistics calculated at the flat start. Conversely, if the projection statistics are calculated considering the estimated values of nodal voltages at the second iteration of the solution process, all measurements associated with zero resistance elements give a better projection in the factor space. This leads to estimates that are more accurate.

4.3.2 Comparison under multiple bad data

The effectiveness of the LNERT-based estimator in obtaining accurate state estimations is demonstrated by comparing its results with respect to the ones given by the classical LNRT-based estimator and by a robust estimator. The robust estimator results are obtained by using the MATLAB code available on-line in [Zhao & Mili 2016], which implements the proposal reported [Mili *et al.* 1996] and [Zhao *et al.* 2016], and is referred to as “a two-stage robust power system state estimation method with unknown measurement noise.”

Numerical simulations are performed in the IEEE 118-bus test system considering the measurements’ configuration reported in [Zhao & Mili 2018], but removing all measurements of currents since the code provided in [Zhao & Mili 2016] does not process these types of measurements. The measurements’ values are generated by adding noise to their true values, which were obtained from a power flow study. The noise in the measurements is generated by

Table 4.4 Quality of the estimates

BDA method	Parameter	β							
		2	4	5	6	7	8	24	72
Gaussian distributed errors									
BDA 1	κ / ρ	6.31 / 3.05	6.39 / 3.21	6.32 / 3.08	6.31 / 3.06	6.31 / 3.07	6.32 / 3.09	6.31 / 3.06	6.30 / 3.05
BDA 2	κ / ρ	6.31 / 3.05	6.42 / 3.24	6.33 / 3.07	6.31 / 3.03	6.31 / 3.03	6.31 / 3.03	6.31 / 3.03	6.31 / 3.03
BDA 3	κ / ρ	6.31 / 3.05	6.42 / 3.24	6.33 / 3.07	6.31 / 3.03	6.31 / 3.03	6.31 / 3.03	6.31 / 3.03	6.31 / 3.03
BDA 4	κ / ρ	>7e3 / 280	>2e6/>7e4	>1e6/>4e4	>1e9/>5e7	>3e7/>1e6	>7e6/>2e5	>1e4 / 450	>2e3 / 94
BDA 5	κ / ρ	>2e3 / 96	>6e6/>2e5	>3e7/>1e6	>1e4 / 365	>1e4 / 372	>1e4 / 372	>1e4 / 365	>3e3 / 114
BDA 6	κ / ρ	7.60 / 4.09	12.4 / 6.53	15.8 / 7.53	18.2 / 8.23	18.0 / 8.33	14.5 / 7.46	7.49 / 3.84	7.48 / 3.83
Gaussian mixture distributed errors									
BDA 1	κ / ρ	8.35 / 3.83	8.50 / 4.02	8.39 / 3.84	8.36 / 3.84	8.37 / 3.85	8.38 / 3.87	8.36 / 3.84	8.36 / 3.83
BDA 2	κ / ρ	8.39 / 3.84	8.58 / 4.07	8.40 / 3.86	8.35 / 3.80	8.35 / 3.80	8.35 / 3.80	8.35 / 3.80	8.35 / 3.80
BDA 3	κ / ρ	8.39 / 3.84	8.58 / 4.07	8.41 / 3.86	8.35 / 3.80	8.35 / 3.80	8.35 / 3.80	8.35 / 3.80	8.35 / 3.80
BDA 4	κ / ρ	>1e9/>5e7	>1e9/>5e7	>1e9/>5e7	>1e9/>4e7	>1e9/>4e7	>1e9/>5e7	>3e9/>1e8	>1e9/>5e8
BDA 5	κ / ρ	>1e9/>6e7	>1e9/>6e7	>1e9/>5e7	>1e9/>5e7	>1e9/>3e7	>2e9/>7e7	>1e9/>5e7	>1e9/>5e7
BDA 6	κ / ρ	10.6 / 5.36	13.5 / 7.83	17.2 / 8.84	19.5 / 9.65	20.1 / 9.99	17.4 / 9.25	10.3 / 4.90	10.3 / 4.90
Laplace distributed errors									
BDA 1	κ / ρ	6.64 / 3.08	6.73 / 3.26	6.67 / 3.09	6.66 / 3.08	6.66 / 3.10	6.66 / 3.12	6.67 / 3.09	6.67 / 3.07
BDA 2	κ / ρ	6.69 / 3.09	6.81 / 3.29	6.76 / 3.06	6.75 / 3.02	6.75 / 3.02	6.75 / 3.02	6.75 / 3.02	6.75 / 3.02
BDA 3	κ / ρ	6.69 / 3.09	6.81 / 3.29	6.76 / 3.06	6.75 / 3.03	6.75 / 3.02	6.75 / 3.02	6.75 / 3.02	6.75 / 3.02
BDA 4	κ / ρ	>1e5/>1e3	>3e5/>1e4	>3e9/>1e8	>1e7/>4e5	>2e6/>1e5	>2e6/>1e5	>2e6/>1e5	>1e6/>3e4
BDA 5	κ / ρ	>4e6/>1e5	>3e5/>1e4	>4e6/>2e5	>8e6/>2e5	>2e5/>1e4	>9e5/>3e4	>6e6/>2e5	>3e5/>1e4
BDA 6	κ / ρ	7.72 / 4.16	14.1 / 6.97	17.6 / 8.01	19.8 / 8.71	19.5 / 8.78	15.9 / 7.79	7.73 / 3.77	7.72 / 3.76
Random distributed errors									
BDA 1	κ / ρ	6.31 / 2.98	6.42 / 3.15	6.34 / 3.01	6.32 / 2.99	6.33 / 3.00	6.34 / 3.02	6.33 / 3.00	6.32 / 2.98
BDA 2	κ / ρ	6.31 / 2.98	6.44 / 3.18	6.35 / 3.00	6.32 / 2.96	6.32 / 2.96	6.32 / 2.96	6.32 / 2.96	6.32 / 2.96
BDA 3	κ / ρ	6.31 / 2.98	6.44 / 3.18	6.35 / 3.00	6.32 / 2.96	6.32 / 2.96	6.32 / 2.96	6.32 / 2.96	6.32 / 2.96
BDA 4	κ / ρ	>1e3 / 43	>7e3 / 543	>1e4 / 982	>3e4/>2e3	>3e5/>1e4	>3e4/>2e3	>1e4 / 665	>3e3 / 133
BDA 5	κ / ρ	873 / 34.4	>4e5/>1e4	>4e5/>1e4	>4e5/>1e4	>4e5/>1e4	>4e5/>1e4	>4e5/>1e4	>4e5/>1e4
BDA 6	κ / ρ	7.26 / 3.97	12.2 / 6.39	15.6 / 7.38	17.8 / 8.11	17.8 / 8.24	14.5 / 7.42	7.19 / 3.68	7.19 / 3.68
Weibull distributed errors									
BDA 1	κ / ρ	6.28 / 2.91	6.38 / 3.06	6.30 / 2.94	6.28 / 2.91	6.29 / 2.93	6.30 / 2.94	6.29 / 2.92	6.28 / 2.91
BDA 2	κ / ρ	6.29 / 2.91	6.42 / 3.09	6.31 / 2.93	6.28 / 2.88	6.28 / 2.88	6.28 / 2.88	6.28 / 2.88	6.28 / 2.88
BDA 3	κ / ρ	6.29 / 2.91	6.42 / 3.09	6.31 / 2.93	6.28 / 2.88	6.28 / 2.88	6.28 / 2.88	6.28 / 2.88	6.28 / 2.88
BDA 4	κ / ρ	>2e6/>1e5	>1e7/>7e5	>2e8/>7e6	>8e7/>4e6	>4e6/>1e5	>1e7/>5e5	>5e5/>1e4	>1e6/>6e4
BDA 5	κ / ρ	>3e7/>1e6	>7e6/>2e5	>2e6/>8e4	>9e6/>3e5	>1e6/>6e4	>2e7/>8e5	>1e5/>7e3	>5e8/>1e7
BDA 6	κ / ρ	7.38 / 3.81	12.5 / 6.38	16.0 / 7.34	18.1 / 7.99	17.1 / 7.80	12.8 / 6.68	7.28 / 3.56	7.27 / 3.55

using Gaussian, Gaussian mixture and Laplace distributions, employing the parameters reported in [Zhao & Mili 2018] to obtain three different sets of measurements, one for each type of probability distribution.

Once each set of measurements has been generated as reported above, a subset of their measurements is corrupted to have two different cases of multiple bad data. Case study 1 considers 13 bad data, where 12 of them are correlated, 11 have different levels of interaction and 2 are critical measurements. On the other hand, case study 2 includes 13 uncorrelated bad data, where 2 of them are critical measurements. Two leverage indicators are obtained for comparison, where the first one is adopted in this thesis to identify which measurements are leverage points. The first leverage indicator of each measurement is obtained from the corresponding diagonal element of the hat matrix $\boldsymbol{K}$ derived in [Abur & Exposito 2004]. A value of K_{ii} close to 1 and greater than 0.85 indicates that the corresponding measurement is a leverage point, while a unitary value indicates that the corresponding measurement is not a leverage point but a critical measurement [Abur & Exposito 2004]. The second leverage indicator is obtained by applying the projection statistics (PS) to the weighted measurement Jacobian matrix $H^{w} = R^{-1/2}H$ that considers the nodal voltages estimated at the second iteration of the estimation process. In this case, the *i*-th measurement is considered as a leverage point if $PS_i > \chi^2_{k,0.975}$, where *k* is the number of nonzero elements in the *i*-th row of H^{w} [Mili *et al.* 1996]. On the other hand, the interaction between measurements is determined by the off-diagonal elements of the residual sensitivity matrix S [Abur & Exposito 2004].

The set of measurements with gross errors for both cases is reported in Table 4.5, which details the type of corrupted measurement, its corresponding K_{ii} value, the weights w_i obtained with the MATLAB code in [Zhao & Mili 2016], as well as the corrupted and true values of measurements. These last values are given in p.u. The weight w_i is computed by $w_i = \min\left\{1, \chi^2_{k,0.975} / PS_i\right\}$. Note that a value lower than 1 indicates that $PS_i > \chi^2_{k,0.975}$ such that the corresponding measurement is identified as a leverage point.

For case study 1, the K_{ii} values indicate that measurements $P^{SCADA}_{flow,5-6}$ and $Q^{SCADA}_{flow,5-6}$ are critical and the leverage points with bad data are $P^{SCADA}_{injec,38}$, $Q^{SCADA}_{injec,38}$, $P^{SCADA}_{flow,98-80}$ and $Q^{SCADA}_{flow98-80}$. None of these measurements is identified by the LNERT since residual-based BDA are unable to detect critical measurements and leverage points [Abur & Exposito 2004]. On the other hand, the correlated measurements are those that have electrical variables in

Table 4.5 Measurements with gross errors for the 118-Bus system

Case 1				Case 2			
Measurement Type	K_{ii}	w_i	**Z_{BD} Value (Z_{true} Value)**	**Measurement Type**	K_{ii}	w_i	**Z_{BD} Value (Z_{true} Value)**
P^{SCADA}_{flow} 5-6	1	0.0124	0.2 (0.885)	P^{SCADA}_{flow} 30-8	0.86	1	-0.4 (-0.739)
Q^{SCADA}_{flow} 5-6	1	0.0125	0.2 (0.041)	P^{SCADA}_{flow} 32-31	0.66	0.1800	0.8 (0.302)
P^{SCADA}_{flow} 66-62	0.33	0.0004	0.5 (0.379)	Q^{SCADA}_{flow} 19-34	0.11	0.9207	-0.8(-0.106)
Q^{SCADA}_{flow} 66-62	0.34	0.0006	0.5 (0.147)	Q^{SCADA}_{flow} 54-55	1	0.2207	-0.8 (0.015)
P^{SCADA}_{injec} 38	0.98	0.0861	0.15 (0.000)	Q^{SCADA}_{flow} 59-60	0.40	0.9385	0.8 (0.036)
Q^{SCADA}_{injec} 38	0.98	0.0817	0.15 (0.000)	Q^{SCADA}_{flow} 66-62	0.33	0.0006	0.8 (0.147)
Q^{SCADA}_{flow} 71-73	0.50	0.2125	0.2 (-0.107)	Q^{SCADA}_{flow} 83-84	1	1	0.8 (0.147)
Q^{SCADA}_{injec} 73	0.50	0.2125	0.2 (0.097)	P^{SCADA}_{flow} 85-88	0.36	0.2034	-0.8 (-0.503)
P^{SCADA}_{injec} 112	0.74	0.2341	0.1 (-0.680)	P^{SCADA}_{flow} 70-75	0.29	0.4033	-0.8 (-0.001)
P^{SCADA}_{flow} 99-80	0.20	1	0.19 (-0.193)	Q^{SCADA}_{injec} 73	0.50	0.2125	0.2 (0.097)
Q^{SCADA}_{flow} 99-80	0.19	1	0.13 (-0.130)	Q^{SCADA}_{flow} 104-100	0.13	0.3731	-0.8 (-0.093)
P^{SCADA}_{flow} 98-80	0.99	1	-0.2 (-0.286)	Q^{SCADA}_{flow} 110-109	0.45	0.0070	0.8 (0.112)
Q^{SCADA}_{flow} 98-80	0.99	1	-0.2 (-0.105)	P^{SCADA}_{flow} 51-49	0.37	0.0633	-1.0 (-0.644)

common in their mathematical representations. In the context of the interaction between measurements, three interactions must be highlighted based on the values of the measurement's residual variances and covariances, as well as the values of the residual sensitivity matrix ***S*** [Abur & Exposito 2004]: $Q^{SCADA}_{flow,71-73}$ with respect to $Q^{SCADA}_{injec,73}$, $P^{SCADA}_{flow98-80}$ with respect to $P^{SCADA}_{flow,99-80}$ and $Q^{SCADA}_{flow98-80}$ with respect to $Q^{SCADA}_{flow99-80}$. In the former interaction, the sensitivity values are the same, i.e., $S_{ii}=S_{ij}=0.5$, which implies that the sensitivities of the measurements' residuals to the measurements' errors are equally affected by the errors in $Q^{SCADA}_{flow,71-73}$ and $Q^{SCADA}_{injec,73}$. On the other hand, the sensitivities of the residuals of $P^{SCADA}_{flow,98-80}$ and $Q^{SCADA}_{flow,98-80}$ with respect to its own errors are 0.01 while the sensitivities of their residuals with respect to the errors in $P^{SCADA}_{flow,99-80}$ and $Q^{SCADA}_{flow,99-80}$, respectively, are 0.05. This implies that the residuals of $P^{SCADA}_{flow,98-80}$ and $Q^{SCADA}_{flow,98-80}$ are more affected by the errors in $P^{SCADA}_{flow,99-80}$ and $Q^{SCADA}_{flow,99-80}$, respectively, than by its own measurement error: the error of the interacting measurement has five times more contribution to the residual.

Lastly, for case study 2, the K_{ii} values indicate that the measurements $Q_{flow,54-55}^{SCADA}$ and $Q_{flow,83-84}^{SCADA}$ are critical, while the bad measurement with the highest leverage force is $P_{flow,30-8}^{SCADA}$.

Based on the estimations obtained by the LNERT-based estimator [Martínez-Parrales & Fuerte-Esquivel 2018], the classical LNRT-based estimation method and the two-stage robust method proposed in [Mili *et al.* 1996] and [Zhao *et al.* 2016], the following quality estimation indexes are reported in Table 4.6 and Table 4.7 for the set of studies associated with cases 1 and 2, respectively. The set of indexes is composed of the biggest absolute error of estimated bus voltage magnitudes (BAEVM), which is expressed in p.u., the biggest absolute error of estimated bus voltage angles (BAEVA) in degrees, the mean absolute errors of estimated bus voltage magnitudes (MAEVM) in $1\text{x}10^{-3}$ p.u. and the mean absolute errors of estimated bus voltage angles (MAEVA) in $1\text{x}10^{-3}$ degrees. These results clearly show that the LNERT-based BDA are capable of obtaining better estimates than the classical or robust methods.

Regarding the identification of bad data, apart from the critical measurement and leverage points, the measurements $Q_{flow,71-73}^{SCADA}$ and $Q_{injec,73}^{SCADA}$ were not identified as a bad datum in case studies 1 and 2, respectively. All other measurements with gross errors were properly detected. Lastly, the estimations of voltage magnitudes and phase angles at each system's node are illustrated in Fig. 4.7 and Fig. 4.8, respectively, for case study 1 considering Gaussian mixture noise in the measurements. These figures clearly show the similitude of the results obtained by the LNERT-based BDAs to the true values of state variables obtained from a power flow study, despite some erroneous measurements not being detected by the bad data analysis.

4.3.2.1 Analysis of the effect of undetected bad data in case study 1

In case study 1, the measurements $P_{flow,5-6}^{SCADA}$ and $Q_{flow,5-6}^{SCADA}$ are critical since they define without redundancy the voltage angle and magnitude of node 6: their removal causes the voltage at node 6 to become unobservable. On the other hand, there exist six redundant good measurements that relate the magnitude and phase angle of voltage at node 5 to the voltages at nodes 3, 4 and 8. This redundancy permits obtaining a very good estimate of the voltage at node 5 even though the errors in critical measurements $P_{flow,5-6}^{SCADA}$ and $Q_{flow,5-6}^{SCADA}$ are not detected by the BDA. The estimated and true values of the voltage magnitude at node 5 are 1.0025 p.u.

Table 4.6 Results for IEEE 118-bus system case 1 of multiple bad data

	BDA 1			BDA 2			BDA 4			ROBUST ESTIMATOR		
Distribution	Gauss	G. M.	Laplace	Gauss	G. M.	Laplace	Gauss	G. M.	Laplace	Gauss	G. M.	Laplace
BAEVM	0.014	0.012	0.013	0.015	0.013	0.014	0.015	0.031	0.032	0.237	0.257	0.238
BAEVA	2.27	2.21	2.24	2.27	2.21	2.23	2.90	2.22	4.29	14.10	15.48	15.50
MAEVM	1.37	1.49	0.810	1.42	1.50	0.768	1.57	3.56	3.40	16.6	17.7	16.3
MAEVA	98.3	128.2	82.7	84.6	117.7	70	167	211	238	1157	1243	988

Table 4.7 Results for IEEE 118-bus system case 2 of multiple bad data

	BDA 1			BDA 2			BDA 4			ROBUST ESTIMATOR		
Distribution	Gauss	G. M.	Laplace	Gauss	G. M.	Laplace	Gauss	G. M.	Laplace	Gauss	G. M.	Laplace
BAEVM	0.084	0.087	0.084	0.084	0.087	0.084	0.677	0.728	0.725	0.663	0.663	0.659
BAEVA	2.98	2.82	2.91	2.96	2.80	2.89	131	34.4	34.2	147.3	143.6	140.4
MAEVM	2.54	2.33	2.03	2.46	2.52	1.74	12.6	11.1	11.6	23.7	25.3	23.7
MAEVA	235.4	280.7	249.1	158	192.6	139	1373	606	791	4605	4692	4426

and 1.0020 p.u., respectively, while the estimated and true values of the voltage angle at node 5 are $-14.0058°$ and $-13.9706°$, respectively. On the other hand, the estimates at node 6 depend completely on the erroneous critical measurements, which results in estimated and true values of voltage magnitude of 0.9890 p.u. and 0.9900 p.u., respectively, and in voltage angle values of $-14.4874°$ and $-16.6974°$, respectively. In this case, the accurate estimation of the voltage at node 5 and the parameters of transmission line between nodes 5 and 6 allow only that a small deviation of the estimated voltage at node 6, with respect to its true value, is required to accomplish the corrupted values of measurements $P_{flow,5-6}^{SCADA}$ and $Q_{flow,5-6}^{SCADA}$. This happens regardless of the method used to perform the BDA, as shown in Fig. 4.7 and Fig. 4.8. Note that the deviation of voltage angle deviation in bus 6 corresponds to the BAEVA reported in Table 4.6.

Regarding corrupted measurements that are leverage points, the measurements $P_{injec,38}^{SCADA}$, $Q_{injec,38}^{SCADA}$ are not detected by the LNERT-based BDA methods, but good estimates were achieved for the voltage at node 38. The estimated and true values for the voltage magnitude are 0.9622 p.u. and 0.9620 p.u., respectively, while for the voltage phase angles are $-12.8507°$ and $-12.8930°$, respectively. The reason behind this result is that node 38 is physically connected to nodes 30, 37 and 65, and four good redundant power flow measurements associate the state variables of node 38 with the ones related to nodes 30 and 65. The gross errors of measurements $P_{injec,38}^{SCADA}$ and $Q_{injec,38}^{SCADA}$, however, affect the estimated voltage at node

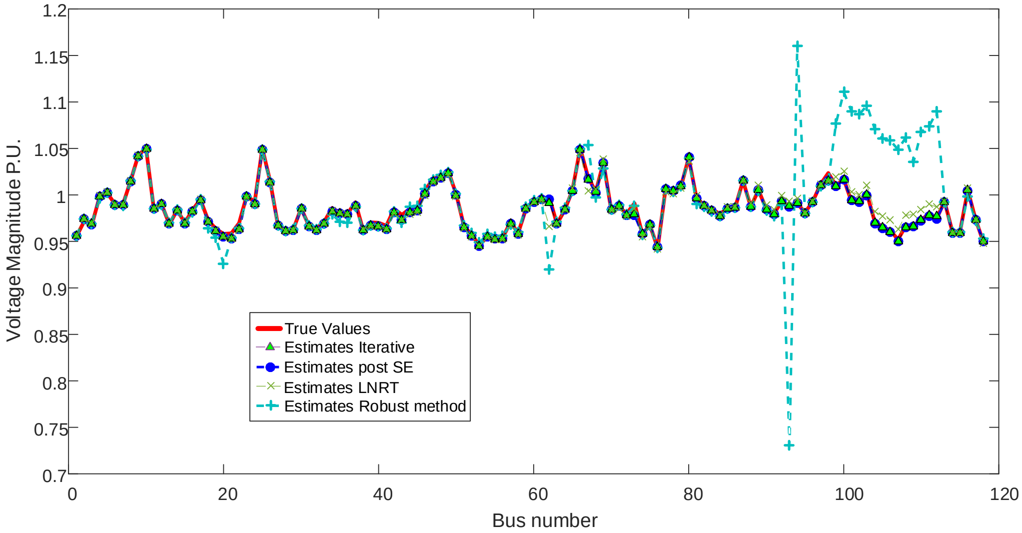

Fig. 4.7 Comparison between true and estimated values of voltage magnitudes.

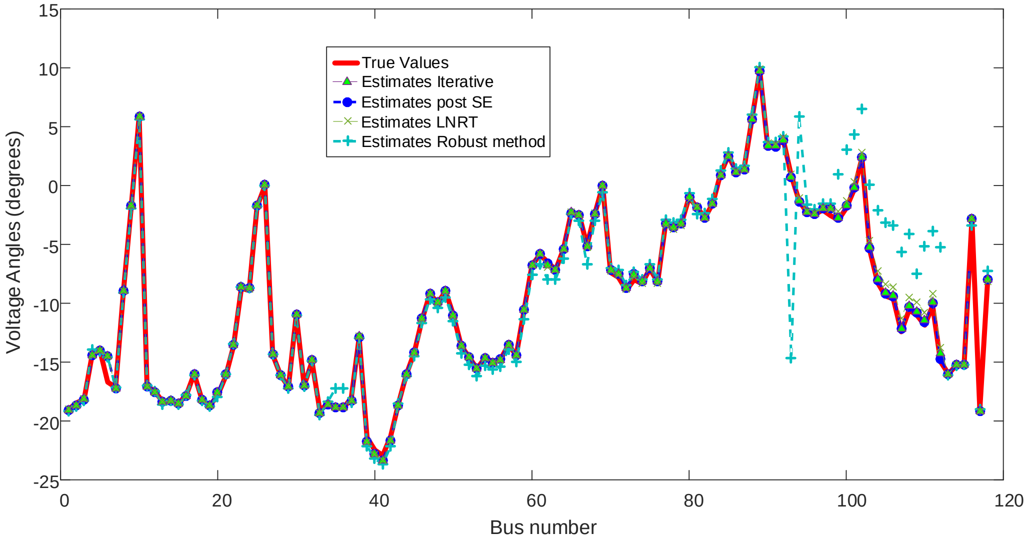

Fig. 4.8 Comparison between true and estimated values of voltage angles.

37, where the estimated nodal voltage is $0.9879\angle -18.2491°$, while the true value is $0.9921\angle -18.0297°$. This has a direct effect on the computed power flow through the transformer connected between nodes 37 and 38, which results in a power flow of 2.5505 + j1.2501 p.u., while the true power flow is 2.437 + j1.12 p.u..

The pair of corrupted power flow measurements from node 99 to 80 are detected by the LNERT-based BDAs thanks to four good redundant measurements associated with node 99, which are composed of the active and reactive power flows from node 99 to 100 and the pair of power injection measurements at node 99. Node 99 is only connected to nodes 100 and 80 such that the bad data identification permits having an accurate estimation of the state variables associated with node 80, where the estimated and true nodal voltage values are $1.0402\angle -1.0037°$ and $1.0400\angle -1.0016°$, respectively. On the other hand, bus 98 has no redundant measurements such that the estimation of its nodal voltage will be affected by the undetected bad leverage measurements $P_{flow,98-80}^{SCADA}$ and $Q_{flow98-80}^{SCADA}$. In this case, the estimated and true nodal voltage values are $1.0156\angle -1.9401°$ and $1.0235\angle -2.5526°$, respectively.

Lastly, the bad measurement $Q_{flow,71-73}^{SCADA}$ is not detected by any of the LNERT-based BDAs, even though it is not a critical measurement or a leverage point. The reason behind this is the existing correlation between $Q_{flow,71-73}^{SCADA}$ and the corrupted measurement $Q_{injec73}^{SCADA}$, where node 71 is the only one connected to node 73. From both erroneous measurements, the LNERT-based BDA selects $Q_{injec73}^{SCADA}$ as a measurement with gross error after the second filtering. In the case of BDA 1, this erroneous measurement will be incorrectly modified during the estimation process to accomplish the erroneous value of $Q_{flow,71-73}^{SCADA}$. On the other hand, when using BDA 2 measurement $Q_{injec73}^{SCADA}$ is removed such that $Q_{flow,71-73}^{SCADA}$ becomes a critical measurement. Since node 71 is physically connected to node 72 and there are two good redundant measurements $P_{flow,71-72}^{SCADA}$ and $Q_{flow,71-72}^{SCADA}$, the estimates of state variables at node 71 are not affected. The estimates at node 73, however, are biased such that the estimated and true voltage values are $0.9784\angle -7.5263°$ and $0.9910\angle -8.0022°$, respectively. Note that the voltage magnitude deviation at node 73 corresponds to the BAEVM reported in Table 4.6.

4.3.3 Applicability of bad data analysis in large-scale systems

The performance of the LNERT-based approaches is analyzed in the large-scale Mexican electric power system, with a geographical representation as shown in Fig. 4.9. For this purpose, a 7659-bus network composed of 482 generator buses, 4225 transmission lines, 4436 transformers and 3493 load buses is considered for the study. This network represents seven control areas electrically interconnected to improve reliability, diversifying generation and supplying security. The complete set of measurements is obtained from a power flow study and is contaminated by adding random noise generated under Gaussian, Gaussian mixture and Laplace distribution, respectively. The measurement redundancy is 2.35 as reported in [Abur

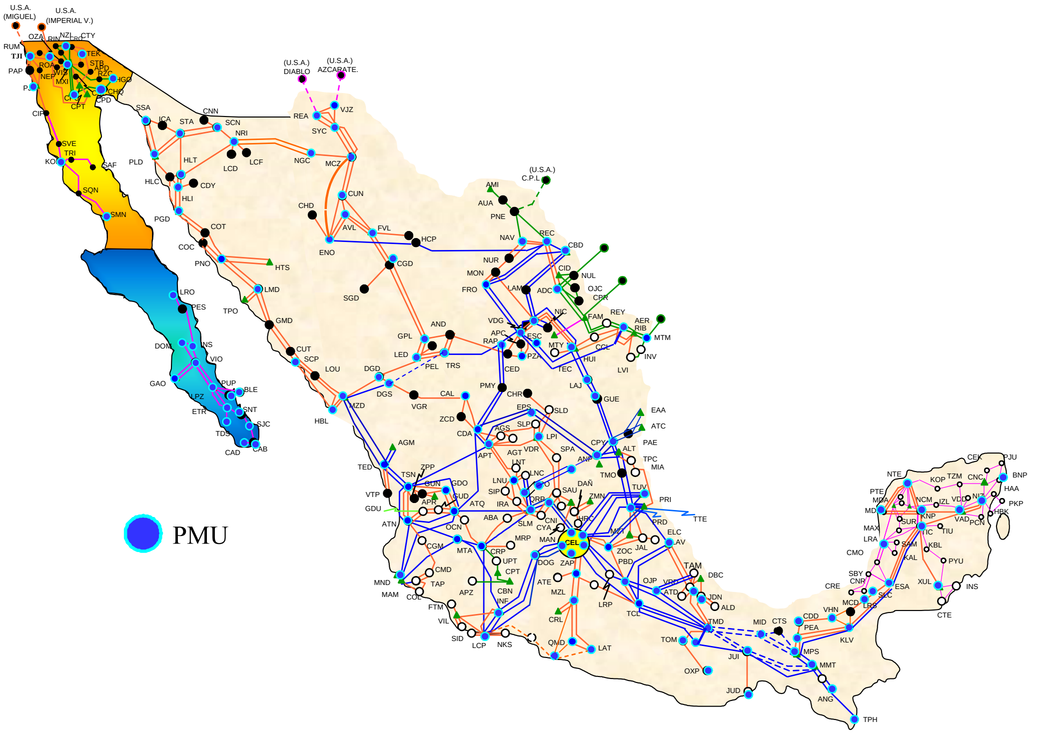

Fig. 4.9 Location of PMUs in the Mexican system

& Lin 2018]. Lastly, 300 randomly chosen measurements, excluding critical measurements since their errors cannot be detected by the LNERT, are corrupted with gross errors as shown in Table 4.8, where the errors' magnitudes as well as their proportions correspond to the ones reported in [Abur & Lin 2018].

The state estimation has been obtained for the three different sets of measurements with gross errors by using the LNERT-based and the LNRT approaches previously described. The results for these case studies are reported in Table 4.9 and consider a mismatch tolerance of 10^{-4} and a maximum number of 1000 iterations. As expected, the BDA 1 and BDA 2 approaches are significantly faster and require fewer numbers of iterations than the standard bad data analysis based on the LNERT. This is due to the simultaneous processing of multiple bad data. These results also demonstrate that performing the bad data analysis at each iteration step of the estimation process, as proposed in [Martínez-Parrales & Fuerte-Esquivel 2018], further reduces the number of iterations and improves the CPU times required for solving the SE problem. The implementation of this approach, however, requires modifying the state estimation program's code. The state estimation process does not converge to a solution if the

Table 4.8 Magnitude of gross errors in the Mexican system.

Error Magnitude	Proportion of Bad Data	Error Magnitude	Proportion of Bad Data
$+80\sigma$	5%	-80σ	5%
$+40\sigma$	10%	-40σ	10%
$+20\sigma$	15%	-20σ	15%
$+10\sigma$	20%	-10σ	20%

Table 4.9 Results for different BDA methods in a large system

	Distribution	BDA 1	BDA 2	BDA 3	BDA 4	BDA 5	BDA 6
Iterations	Gaussian	17	23	583	74	1000	1000
	Gaussian Mix.	16	23	582	24	1000	1000
	Laplace	16	23	582	25	1000	1000
Time (sec)	Gaussian	76	96	2439	9244	4555	4589
	Gaussian Mix.	72	99	2577	3437	4308	4284
	Laplace	73	99	2640	3949	4315	4186
BDCI (**GMIIB**)	Gaussian	288 (**23**)	283 (**18**)	285 (**16**)	31 (**6**)	- (**-**)	- (**-**)
	Gaussian Mix.	283 (**33**)	279 (**22**)	278 (**23**)	8 (**3**)	- (**-**)	- (**-**)
	Laplace	286 (**29**)	282 (**19**)	281 (**20**)	9 (**2**)	- (**-**)	- (**-**)
MAEVM (**MAEVA**)	Gaussian	0.385 (**22.04**)	0.366 (**20.99**)	0.368 (**20.96**)	0.604 (**31.26**)	- (-)	- (-)
	Gaussian Mix.	0.459 (**27.20**)	0.442 (**26.07**)	0.443 (**26.07**)	0.666 (**39.56**)	- (**-**)	- (**-**)
	Laplace	0.233 (**14.41**)	0.208 (**13.24**)	0.209 (**13.24**)	0.476 (**27.98**)	- (**-**)	- (**-**)

projection statistics method is used together with the LNRT, i.e., BDA 5 and BDA 6, independently of the type of noise in the measurements. The computing time for these two BDA methods is shorter, however, than the one required for BDA 4, even though the latter achieves the solution in 74 iterations or fewer. These longer computing times for BDA 4 are associated with the computational burden in calculating the residual covariance matrix necessary for normalizing the residuals.

The projection statistics and the associated weights used in BDA 5 and BDA 6 were calculated off-line with a homemade MATLAB-based program, which took over 29 hours for each *PS*. The results of this program were validated with respect to the ones obtained by using the program reported in [Zhao & Mili 2016]. This validation was performed by analyzing small power systems such as the ones reported in Sections 4.3.1 and 4.3.2. The computer used to perform all these studies was a Lenovo P71 with a Xeon CPU E3-1505Mv6 of 3 GHz and 40 GB of RAM.

On the other hand, the number of measurements with gross errors that have been correctly identified as bad data in the set of measurements are also reported by using the acronym BDCI, while the good measurements that have been incorrectly identified as bad are indicated by using the acronym GMIIB. Note that for BDA 5 and BDA 6, the values of BDCI and GMIIB are not available since these methods did not converge to a solution.

These results shows that the lowest identification rate of bad data for the BDA 2 and BDA 1 approach are 93% and 94%, respectively. Similarly, the highest misidentification rate of good measurements for these two approaches corresponds to 7.3% and 11%, respectively. These two metric rates are defined as reported in [Abur & Lin 2018]: BDCI/(number of bad data) and GMIIB/(number of bad data), respectively. Note that the LNRT has its lowest identification rate at 2.7% and its highest misidentification rate at 1%.

Lastly, the accuracy of the state estimations is quantified by the indexes associated with the mean absolute errors of estimated voltage magnitudes (MAEVM), expressed in $1\text{x}10^{-3}$ p.u., and of estimated voltage angles (MAEVA) in $1\text{x}10^{-3}$ degrees. These results show that the estimator using BDA 2 achieves the best estimates. Since this proposal eliminates the identified bad measurements instead of correcting them such as BDA 1, the smearing effect of those bad data is completely eliminated during the estimation process, yielding better estimates. On the other hand, the values of accuracy indexes given by the LNERT method, which does not apply any smearing effect filter, are very similar to the ones given by the other two LNERT-based approaches but with a very high computational burden. This demonstrates that the filtering processes explained in Section 3.4 drastically reduce the computing time without affecting the estimates. Lastly, the indexes for the LNRT-based method show less accuracy than the LNERT-based methods.

4.4 Constrained static state estimation

The effectiveness of the proposed approach is numerically demonstrated by using the IEEE 14-bus test system, the CIGRE test system and a 7659-bus representation of the Mexican interconnected power system. The state estimations are conducted using measurement data generated from power flow studies and considering random errors with a normal probability density function and zero mean. The standard deviations considered for the different types of measurements are $\sigma_{P_n} = \sigma_{Q_n} = 0.02$, $\sigma_{P_{ij}} = \sigma_{Q_{ij}} = 0.01$, $\sigma_v = 0.004$, $\sigma_V^{PMU} = 0.001$ and $\sigma_{\theta_V}^{PMU} = 0.001$. Lastly, three different approaches of bad data analysis (BDA) are used for detecting, identifying and correcting/eliminating the gross errors intentionally introduced in the set of measurements. These approaches are the following: i) the unified SE-BDA method based on the largest normalized estimated residual test (LNERT) [Martínez-Parrales & Fuerte-Esquivel 2018]; ii) a BDA only based on the largest normalized residual test (LNRT) [Abur & Lin 2018]; and iii) the classic BDA based on the chi-squared test χ^2 and the LNRT [Abur & Exposito 2004]. For the application of each BDA methodology, a *Th* value of 3 is used for the iterative method based on the LNERT. On the other hand, a threshold of 3 is adopted for the LNRT approach, whereas the chi-squared test is applied using a significance level of 0.99.

4.4.1 IEEE 14-bus test system

The system's topological structure and the locations of the different types of measurements used in the study are shown in Fig. 4.10. The system is divided into two control areas in which interchanges of power must be maintained within physical limits of tie lines. One control area, referred to as an internal system, is composed of buses 1 through 9, excluding bus 6, and is connected to the other control area, which can be considered an external system, through tie lines 9-10, 9-14 and 5-6. Nodal injection measurements are not available for the internal system, but this kind of measurement is available at all nodes of the external system, together with a few others types of measurements.

The power flows shared between the two control areas are assumed to be bound as reported in Table 4.10. Additionally, the voltage magnitudes at buses 8 and 14, together with the power injection at bus 8, are also constrained as indicated in Table 4.10. All data reported in column 4 of this table are obtained from the power flow study, where voltage magnitudes are given in per unit (p.u.) and active and reactive powers are given in MW and MVArs, respectively.

Since all constrained variables remain within their feasible bounds when the operating state is estimated considering the set of measurements with no gross errors, a new state estimation is performed but considers the bad data introduced in the set of measurements reported in Table 4.11. Note that the first two corrupted measurements correspond to conforming errors [Abur & Exposito 2004], while the last four are leverage points [Abur & Exposito 2004].

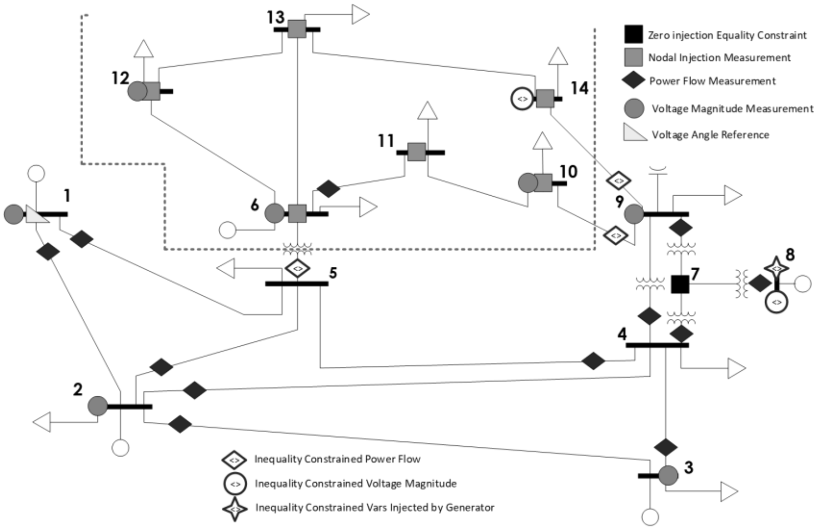

Fig. 4.10 IEEE 14-bus system and measurement configuration

Table 4.10 IEEE 14-bus system inequality constraints

Electric variable	***Lower limit***	***Upper limit***	***Power Flow***
v_8	0.95	1.09	1.09
v_{14}	0.95	1.05	1.0355
$P_{9\text{-}14} + \mathrm{j}\, Q_{9\text{-}14}$	9 + j 3	30 + j 15	9.43 + j 3.61
$P_{9\text{-}10} + \mathrm{j}\, Q_{9\text{-}10}$	5 + j 2	30 + j 12	5.23 + j 4.22
$P_{5\text{-}6} + \mathrm{j}\, Q_{5\text{-}6}$	42 + j 10	82 + j 30	44.09 + j 12.47
$P_8 + \mathrm{j}\, Q_8$	0 – j 6	24 + j 24	0 + j 17.62

Table 4.11 Measurements with gross errors for IEEE 14-bus system

Measurement	***Original value***	***Corrupted value***
$Q_{8\text{-}7}$	17.62	27.01
$Q_{9\text{-}7}$	-4.98	-15.79
P_6	-11.20	11.20
Q_6	5.23	-5.23
P_{14}	-14.90	4.70
Q_{14}	-5.00	13.90

The state estimation results for the case in which inequality constraints are not considered in the study are reported in Table 4.12 for the nodal voltages and in Table 4.13 for the constrained variables. The number of iterations required by the estimator according to the BDA employed in the study, as well as the amount of bad data correctly and incorrectly identified, are also reported in this table. These results clearly show that the estimated values of several bounded electric variables are well outside their specified limits. The estimation results also depend on how well the selected BDA approach performs, as could be expected.

Table 4.12 Estimated values of bus voltages

	Without inequality constraints						***With inequality constraints***					
	Iterative		***LNRT***		χ^2		***Iterative***		***LNRT***		χ^2	
Bus	v	θ	v	θ	v	θ	v	θ	v	θ	v	θ
1	1.0611	0.00	1.0616	0.00	1.0611	0.00	1.0545	0.00	1.0546	0.00	1.0528	0.00
2	1.0461	-4.97	1.0467	-4.97	1.0461	-4.97	1.0394	-5.03	1.0395	-5.03	1.0377	-5.05
3	1.0106	-12.67	1.0111	-12.65	1.0106	-12.67	1.0039	-12.84	1.0040	-12.83	1.0023	-12.88
4	1.0205	-10.30	1.0211	-10.29	1.0205	-10.30	1.0126	-10.44	1.0127	-10.44	1.0106	-10.48
5	1.0222	-8.77	1.0229	-8.76	1.0222	-8.77	1.0146	-8.89	1.0147	-8.89	1.0126	-8.92
6	1.0680	-12.52	1.0665	-14.23	1.0680	-12.52	1.0592	-14.15	1.0583	-14.16	1.0550	-14.21
7	1.0652	-13.28	1.0658	-13.32	1.0652	-13.28	1.0512	-13.53	1.0512	-13.48	1.0512	-13.56
8	1.1095	-13.28	1.1101	-13.33	1.1095	-13.28	1.0900	-13.53	1.0900	-13.48	1.0900	-13.56
9	1.0502	-14.83	1.0508	-14.90	1.0502	-14.83	1.0365	-15.15	1.0364	-15.08	1.0376	-15.18
10	1.0461	-14.55	1.0467	-15.07	1.0461	-14.55	1.0334	-15.34	1.0333	-15.27	1.0344	-15.37
11	1.0535	-13.40	1.0533	-14.79	1.0535	-13.40	1.0442	-14.90	1.0440	-14.83	1.0416	-14.98
12	1.0560	-13.74	1.0548	-15.90	1.0560	-13.74	1.0499	-15.67	1.0520	-15.28	1.0430	-15.99
13	1.0556	-13.71	1.0419	-16.54	1.0556	-13.71	1.0397	-15.46	1.0410	-15.21	1.0321	-15.72
14	1.0736	-14.57	1.0698	-15.76	1.0736	-14.57	1.0179	-16.27	1.0178	-16.19	1.0189	-16.29

Table 4.13 Estimated values without inequality constraints

Estimated Variable	***Iterative***	***LNRT***	χ^2
v_8	**1.1095**	**1.1101**	**1.1095**
v_{14}	**1.0736**	**1.0698**	**1.0736**
$P_{9\text{-}14} + j\,Q_{9\text{-}14}$	**-5.05 – j6.71**	**2.30 - j8.39**	**-5.05 - j6.71**
$P_{9\text{-}10} + j\,Q_{9\text{-}10}$	**-3.81** + j6.58	5.15 + j3.21	**-3.81** + j6.58
$P_{5\text{-}6} + j\,Q_{5\text{-}6}$	**30.36** + j13.53	44.20 + j15.60	**30.36** + j13.53
$P_8 + j\,Q_8$	0 + **j27.86**	**-0.1 + j27.88**	0 + **j27.86**
Iterations	4	7	4
Correct identifications	0	0	0
Incorrect identifications	0	1	0
MSE	1.92 x10^{-4}	9.20x10^{-5}	1.92 x10^{-4}

Since the prime objective of this Section is to demonstrate the efficiency of the proposed approach, the capacity of each BDA methodology for detecting, identifying and correcting/eliminating bad data is not discussed here. In this context, the study described above is repeated but considers inequality constraints through the proposed approach, with the results reported in Table 4.12 and Table 4.14. As expected, the estimated values of all algebraic state variables that would violate their physical limits were enforced during the estimation process to the values of their corresponding violated limit, independently of the BDA method used for the estimation. Note also that the number of iterations required to estimate the operating state increased with respect to the ones required when no inequality constraints are considered. This was due to four bad data being correctly identified, while two other good data were incorrectly considered as gross errors. Lastly, the quality of the estimates are quantified by using the mean

Table 4.14 Estimated values with the proposed method

Estimated variable	*Iterative*	*LNRT*	χ^2
v_8	1.0900	1.0900	1.0900
v_{14}	1.0179	1.0178	1.0189
$P_{9\text{-}14} + \mathrm{j}\, Q_{9\text{-}14}$	9.00 + j3.00	9.00 + j3.00	9.00 + j3.00
$P_{9\text{-}10} + \mathrm{j}\, Q_{9\text{-}10}$	5.00 + j2.00	5.00 + j2.00	5.00 + j2.00
$P_{5\text{-}6} + \mathrm{j}\, Q_{5\text{-}6}$	42.00 + j14.64	42.00 + j15.08	42.00 + j15.63
$P_8 + \mathrm{j}\, Q_8$	0.00 + j24.00	0.00 + j24.00	0.00 + j24.00
Iterations	15	25	14
Correct identifications	4	4	0
Incorrect identifications	2	2	0
MSE	$6.77\text{x}10^{-5}$	$6.15\text{x}10^{-5}$	$9.51\text{x}10^{-5}$

squared error (MSE), which is defined as the average of the squared differences between the estimated and the true value of the algebraic state variables. The values of this quality index are reported in Table 4.13 and Table 4.14, from which the higher quality of the estimates obtained by the proposed approach can be observed.

The four measurements correctly identified as bad data by the iterative LNERT- and LNRT-based methods are $Q_{8\text{-}7}$, P_6, P_{14} and Q_{14}. These performances of both BDA methods reflects the impact of using inequality constraints linked to measurements with gross errors: the residual values of these bad data increased when considering the inequality constraints. By way of example, the measurement $Q_{8\text{-}7}$ is directly associated with the reactive power injection at node 8, which is bounded to 24 MVArs. The enforcement of this limit results in a residual value of 3.01 MW for $Q_{8\text{-}7}$, which in turn allows this measurement to be identified as an erroneous datum. A similar line of reasoning can be applied to the other three identified bad data: the measurement P_6 is associated with the bounded power flow $P_{5\text{-}6}$, while measurements P_{14} and Q_{14} are related to the constrained variables $P_{9\text{-}14}$, $\mathrm{Q}_{9\text{-}14}$ and v_{14}.

Lastly, the state estimation study reported above is newly performed by using the constrained-based WLS and WLAV state estimators, which are solved with an interior point method. Two different BDAs are performed together with the WLS-based estimator, as reported in Table 4.15. Since the residual covariance matrix is not obtained in the interior point method, the weighted residuals are used instead of the normalized ones to perform the BDA [Mili & Van Cutsem 1988]. The results of these estimations, which are reported in Table 4.15, clearly show that the MSE index obtained when minimizing the WLS errors through an

Table 4.15 Estimated values with the interior point method

Estimated variable	*WLS* *No BDA*	*WLS* *+LWRT*	*WLS* *+ χ^2 + LWRT*	*WLAV*
$\boldsymbol{v_8}$	1.0900	1.0680	1.0680	1.0899
$\boldsymbol{v_{14}}$	1.0240	1.0070	1.0070	1.0284
$\boldsymbol{P_{9\text{-}14} + \mathrm{j}\, Q_{9\text{-}14}}$	9.00 + j3.00	30.00 + j3.00	30.00 + j3.00	9.11 + j3.05
$\boldsymbol{P_{9\text{-}10} + \mathrm{j}\, Q_{9\text{-}10}}$	7.41 + j6.70	5.00 + j4.39	5.00 + j4.39	5.08 + j4.71
$\boldsymbol{P_{5\text{-}6} + \mathrm{j}\, Q_{5\text{-}6}}$	42.00 + j19.96	42.00 + j16.44	42.00 + j16.44	42.12 + j18.05
$\boldsymbol{P_8 + \mathrm{j}\, Q_8}$	0.02 + j21.1	0.00 + j1.84	0.00 + j1.84	0.08 + j15.92
Correct identifications	-	3	3	-
Incorrect identifications	-	2	2	-
MSE	$1.25\text{x}10^{-4}$	$1.77\text{x}10^{-4}$	$1.77\text{x}10^{-4}$	$2.36\text{x}10^{-5}$

interior point method is greater than the MSE obtained by the proposed approach. The opposite occurs, as expected, when the study is performed by using the robust WLAV estimator.

4.4.2 CIGRE test system

The effectiveness of the proposed approach in constraining the values of an OLTC and the modulation index of a VSC within their physical limits is numerically demonstrated in this section. For this purpose, the operation state associated with the CIGRE test system shown in Fig. 4.11a is estimated under the conditions detailed in [Martínez-Parrales & Fuerte-Esquivel 2018]. The electric circuit representing a VSC-based AC-DC station connected to the secondary winding of an OLTC transformer is shown in Fig. 4.11b. The upper and lower physical limits of the VSC modulation index are 1.0 and 0, respectively, while the upper and lower physical limits of the OLTC are 1.1 and 0.9, respectively. Based on the information reported in [Martínez-Parrales & Fuerte-Esquivel 2018], the measurements associated with currents inside the AC-DC converter station connected at node 37 are removed to make the power flow measurement from node 36 to 37 a critical measurement; this power flow measurement is then corrupted with a gross error. The effect of this undetectable gross error is that the estimated values of both the modulation index and the OLTC of the AC-DC converter station connected at node 37 are outside their physical limits, as reported in Table 4.16. On the other hand, the estimated values of these algebraic state variables are fixed to the violated physical limit when the inequality constraints are considered during the estimation process, as reported in Table 4.17.

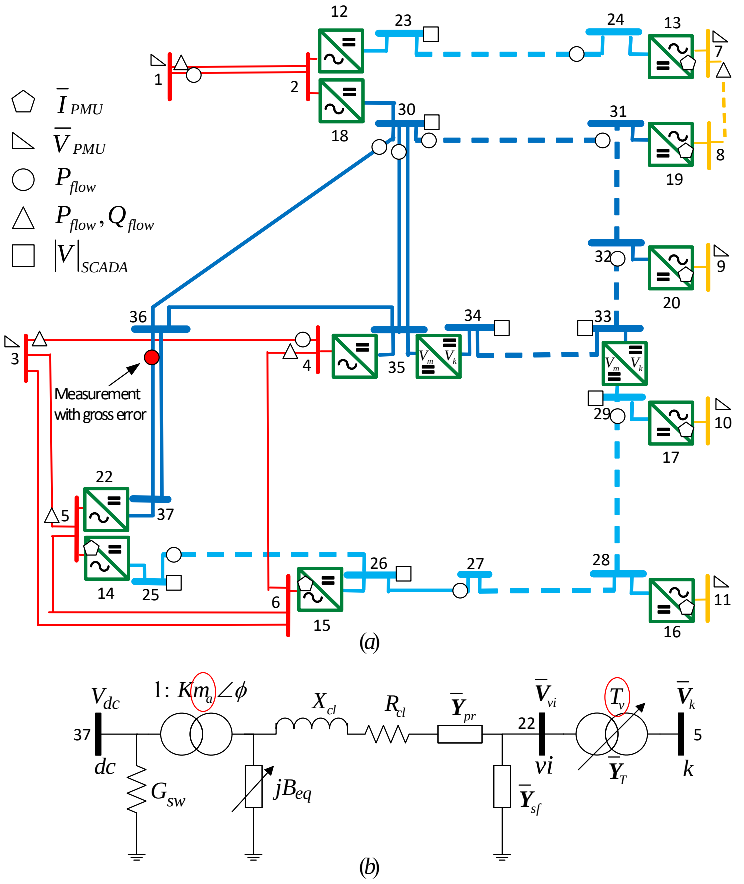

Fig. 4.11 CIGRE test system a) measurement's configuration and b) detail of the AC-DC converter station connected to node 37.

Table 4.16 Estimated values of CIGRE system without inequality constraints

Estimated Variable	***Iterative***	***LNRT***	χ^2
m_a	**1.0409**	**1.0404**	**1.0404**
T_v	**0.8544**	**0.8551**	**0.8551**
Iterations	5	10	5
Correct identifications	0	0	0
Incorrect identifications	1	1	0
MSE	4.83×10^{-2}	4.80×10^{-2}	4.80×10^{-2}

Table 4.17 Estimated values of CIGRE system with the proposed method

Estimated Variable	***Iterative***	***LNRT***	χ^2
m_a	1.0000	1.0000	1.0000
T_v	0.9000	0.9000	0.9000
Iterations	14	28	28
Correct identifications	0	0	0
Incorrect identifications	2	1	1
MSE	2.77×10^{-2}	3.02×10^{-2}	3.02×10^{-2}

4.4.3 Mexican 7659-bus system

The Mexican electric power system considered in this section corresponds to a 7659-bus network composed of 482 generator buses, 3493 load buses, 4225 transmission lines and 4436 transformers. This electric power system is divided into seven regional control areas electrically interconnected through 21 tie lines, as shown in Fig. 4.12, for improving its operating reliability. Furthermore, there are 22 other transmission lines of paramount importance at different control areas for ensuring a secure operational control. Hence, all these 43 transmission lines must transmit power without violating their physical limits.

Based on the information mentioned above, a set of 33092 measurements with Gaussian noise are generated by means of a power flow study. Furthermore, 22 of those measurements are corrupted with gross errors in order to bias the state estimation. The number of transmission lines in which the power flows are estimated outside their physical limits is reported in Table 4.18 for each state estimation study, i.e. with and without taking into account the inequality constraints. Note that these studies were performed considering different types of BDA. The results associated with the number of iterations, the computational time required to achieve convergence during the estimation process and the MSE are also reported in this table. Note that when the proposed method is applied all the estimated power flows of the constrained lines are inside the specified bounds, independently of the BDA method applied.

4.5 Conclusions

The proposed approach’s capability of estimating the operating state of an integrated AC-DC multi-terminal network and of correcting multiple bad data has been successfully illustrated by numerical examples.

On the other hand, the suitability of applying LNERT-based bad data analysis together with a WLS-based state estimator, which is the one currently used in control centers, to obtain accurate estimates when the error distribution of measurements is not truly Gaussian has been demonstrated by numerical examples. This solves the problem that occurs in practice in which realistic PMU errors follow non-Gaussian probability distributions and SCADA measurements can also have non-Gaussian noises. Furthermore, the LNERT-based approaches for bad data analysis improve the numerical solution feasibility by correcting or eliminating multiple bad

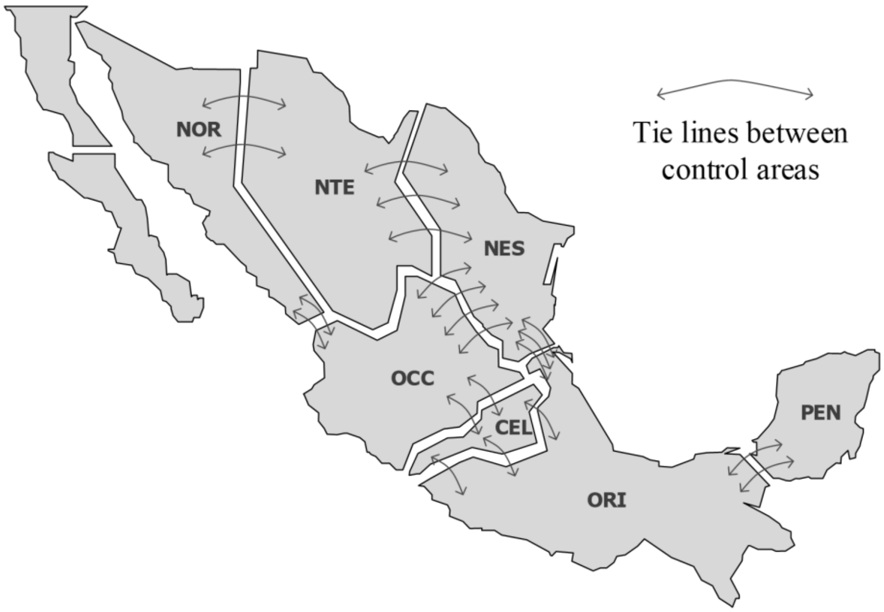

Fig. 4.12 The Mexican interconnected system, control areas and tie lines.

Table 4.18 Time comparison by applying the proposed method in large systems

	No physical limits			With physical limits		
	Iterative	***LNRT***	χ^2	***Iterative***	***LNRT***	χ^2
Flows out of bounds	8	9	11	0	0	0
Iterations	21	5	4	38	40	16
Time in seconds	87.26	371	191	155	2393	183
MSE	$1.86\text{x}10^{-3}$	$2.66\text{x}10^{-3}$	$2.66\text{x}10^{-3}$	$5.85\text{x}10^{-4}$	$1.76\text{x}10^{-3}$	$1.84\text{x}10^{-3}$

measurements in each SE solution process. The risk of incorrectly identifying good measurements affected by bad measurements through the smearing effect is highly reduced, with a negligible increase in the computational burden. Lastly, it has been demonstrated that the computational time necessary for solving the state estimation problem by the LNERT-based approaches for very large systems is reduced with respect to other methods. This is an important breakthrough because, while maintaining accuracy, a practical application of these approaches to on-line state estimation assessment becomes attainable.

The capability of the proposed approach for automatically checking and enforcing physical limits during the state estimation process has been successfully illustrated by numerical examples. Furthermore, the use of this proposal for the state estimation of systems with large dimensions and detailed modeling comes within reach, as numerically demonstrated with its application to the Mexican interconnected electric power system.

Lastly, the representation of inequality constraints by nonlinear algebraic equations based on the Fischer-Burmeister function is completely general and can be employed for considering physical limits in any other kinds of constrained state estimators: constrained least absolute value state estimators, without modifying the way in which these estimators are mathematically formulated and solved.

Chapter 5

5 Tracking Nodal Frequency and State Estimation

5.1 Introduction

Synchronization of the nodal frequency at a nominal frequency value throughout the network is essential to ensure reliable operation of the entire power system. This synchronization is achieved by maintaining a near real-time balance between the input mechanical power in generators and the load power. A large disturbance in this balance results in frequency deviations in time and space. Since significant frequency deviations can lead to load shedding, operating instability and even blackouts, system operators use a combination of control actions to restore the system frequency very close to its nominal level. The effectiveness of these control actions, however, will depend on the accuracy with which the system-wide frequency is measured. A novel approach for directly estimating the voltage frequency at each node of an electric power system is proposed in this chapter. The nodal frequency estimation is performed based on a tracking state estimation and considers two different methodologies, according to the existing time frame between estimations. Lastly, case studies are presented to evaluate this proposal together with its application in observing interarea oscillations.

5.2 Formulation of tracking state estimation

A tracking state estimator processes a redundant set of physical measurements $\boldsymbol{z} \in \mathbb{R}^{\mathrm{m}}$ at short intervals of time in order to estimate the state variables $\hat{\boldsymbol{x}} \in \mathbb{R}^{\mathrm{n}}$ that define the operating point of a power system, thus achieving the monitoring and discerning of the operative dynamics occurring in the system. The set of physical measurements considered for the estimation are the ones provided by a supervisory control and data acquisition (SCADA) system and by phasor measurement units (PMU).

A tracking state estimation (TSE) recursively solves (3.23), as detailed in Section 3.3, at successive discrete times until the maximum absolute increment of the state variables is lower than a specified tolerance, e.g. $1x10^{-4}$ such that $\left\|\Delta\hat{\boldsymbol{x}}^{k}\right\|_{\infty} < 1x10^{-4}$, or the number of iteration *k* is equal to a maximum limit, e.g. 20. Moreover, the initial values $\hat{x}^0$ for the iterative solution of (3.23) at the time instant t are equal to the estimated states $\hat{x}^k$ obtained at the previous time instant $t-1$.

5.2.1 Processing of measurements

Unlike PMUs, time tagging in SCADA measurements is not typically available, so it is not possible to exactly know the time at which these measurements were taken. Furthermore, the SCADA measurements gathering process is very different to the one associated with PMUs so that both types of measurements arrive to the control center's master unit with different delays and periodicity. This time skew problem has a direct impact on the estimated state when the system is experiencing dynamic perturbations greater than normal quasi-static changes that the system is subject under a normal state of operation.

In a given substation, the *r*-th RTU scans the values of all *u* available transducers and stores these values in the internal memory in a sequential manner, taking δ_r seconds for each value. This process is cyclically repeated every T_r^s seconds, where $T_r^s = u\delta_r$ and is in the order of 1 second. When the RTU data are requested at a given time, the *u* measurements contained in the internal memory are sent to the control center with a transmission time τ_r that is usually less than 0.5 seconds [Alcaide-Moreno B. A. *et al.* 2017]. The *r*-th RTU data are requested by the control center at regular time intervals T_r^{dr} in the order of 2 to 5 seconds. This means that the *u*-th measured value arrives to the control center $\tau_r + \delta_{ur}$ seconds after it was taken, where $\delta_{ur} = \rho\delta_r$ and the value of ρ is between 0 and *u*. Moreover, The delay time given by the difference between the instant at which a measurement arrives to the control center and the moment when this measurement is processed by the estimator is denoted by κ_r such that the total delay time is $\Delta_u = \tau_r + \delta_{ur} + \kappa_r$.

The set of measurements processed by the TSE at time intervals T^{TSE} is composed of time-tagged PMU and SCADA measurements as well as SCADA measurements without the time tag. Even though the power electric systems are evolving in the direction to make the system observable by only time-tagged measurements, today´s control centers depend on measurements without a time stamp to make the system observable for the state estimation.

In this context, the delay time associated with time-tagged SCADA measurements is known by simply comparing the TSE processing time *t* with the *u*-th measurement time stamp ts_u^{SCADA}, $\Delta_u = t - ts_u^{SCADA}$. The delay time can now be used to assign the time-tagged SCADA measurements to an SE interval $\left[t-(p+1)T^{TSE}, t-pT^{TSE}\right]$ such that $\left(p+1\right)T^{TSE} \leq \Delta_u < pT^{TSE}$, where p is a positive integer value.

Similarly to that reported in [Alcaide-Moreno B. A. *et al*. 2017], the TSE processes at instant *t* all non-time tagged SCADA measurements received during the interval $\left[t-T^{TSE}, t\right]$, the time-tagged SCADA measurements associated with the interval $\left[t-(p+1)T^{TSE}, t-pT^{TSE}\right]$ and the PMU measurements received in the time interval $t-(p+0.5)T^{TSE}$, as illustrated in Fig. 5.1.

5.3 Nodal frequency estimation

A PMU measurement contains a time stamp to indicate the moment at which the measurement was performed. This physically means that at a given time t_1 the PMU measures the difference between the angle of phase A at the *i*-th node, i.e., ϕ_i, and the angle of the reference signal ϕ_{ref} synchronized with the GPS clock and rotating at the nominal system's frequency such that

$$\theta_{PMU,i}^{t_1} = \phi_i^{t_1} - \phi_{ref}^{t_1} \quad . \tag{5.1}$$

A similar line of reasoning is applied to the PMU measurement taken at time instant t_2 such that $\theta_{PMU,i}^{t_2} = \phi_i^{t_2} - \phi_{ref}^{t_2}$. Hence, the difference $\Delta\theta_{PMU,i}^{t_{1,2}} = \theta_{PMU,i}^{t_2} - \theta_{PMU,i}^{t_1}$ can be denoted as

$$\begin{aligned} \Delta\theta_{PMU,i}^{t_{1,2}} &= \left(\phi_i^{t_2} - \phi_{ref}^{t_2}\right) - \left(\phi_i^{t_1} - \phi_{ref}^{t_1}\right) \\ &= \left(\phi_i^{t_2} - \phi_i^{t_1}\right) - \left(\phi_{ref}^{t_2} - \phi_{ref}^{t_1}\right), \end{aligned} \tag{5.2}$$

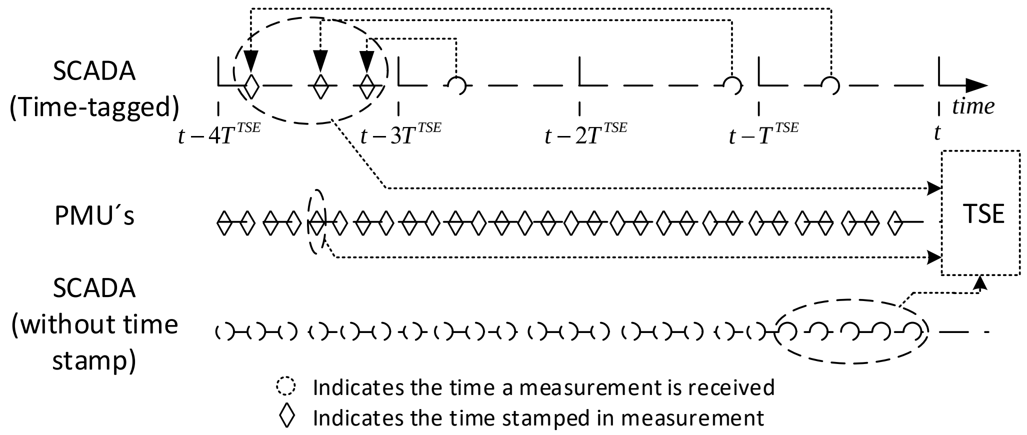

Fig. 5.1 Measurements' handling for TSE

where $\phi_i^{t_2}-\phi_i^{t_1}$ represents the angular displacement of phase A at the i-th node, while $\phi_{ref}^{t_2}-\phi_{ref}^{t_1}$ represents the angular displacement of the reference signal during the time given by $\Delta t_{1,2}=t_2-t_1$. A positive value of $\Delta\theta_{PMU,i}^{t_{1,2}}$ indicates that the phase angle displacement at the i-th node was greater than the signal reference's angle displacement: the frequency of the nodal phase angle is greater than the reference frequency.

The angular displacement at the i-th node in one period of time can be computed with respect to the reference signal T_{ref} , which rotates one cycle of 2π radians, by using the following linear relationship:

$$\Delta\theta_{PMU,i}^{T}=\frac{\Delta\theta_{PMU,i}^{t_{1,2}}}{\Delta t_{1,2}}T_{ref} \quad . \tag{5.3}$$

The angular displacement $\Delta\theta_{PMU,i}^{T}$ represents the amount of radians that the phase angle A at the i-th node has rotated faster or slower than the 2π radians that the nominal frequency has rotated during T_{ref} .

The existing relationship between the frequency computed from the PMU measurements at the i-th node and the reference frequency can be calculated by using the linear relationship between the amount of rotated radians during a period of time and the frequency:

$$\frac{f_{PMU,i}}{f_{ref}}=\left(\frac{2\pi+\Delta\theta_{PMU,i}^{T}}{2\pi}\right) . \tag{5.4}$$

On the other hand, by assuming that the phasor measurements processed at each SE solution have the same time stamp, the rate of change of each estimated phasor over time can be determined based on two consecutives SE studies . Note that even with different PMU vendors the SE can compensate for the time skew problem by choosing the appropriate PMU sample.

By considering the estimation process as a filtering process for physical measurements, the computation of the nodal frequency is more accurate when using the estimated voltage angles $\hat{\boldsymbol{\theta}}$ than by considering PMU measurements. In this context, the voltage angles are estimated with respect to a reference signal at system's nominal frequency, e.g. 60 Hz., synchronized to the GPS signal, and at the same time the PMU errors are detected, identified and eliminated/corrected during the state estimation process.

By considering two consecutive SE solutions, named SE$_1$ and SE$_2$, the associated time stamps can be used to calculate the time difference $\Delta t_{1,2}$ associated with the angle estimates $\hat{\theta}_i^{SE_1}$ and $\hat{\theta}_i^{SE_2}$ at the *i*-th node:

$$\Delta t_{1,2} = \left(t \ in \ SE_2\right) \ - \ \left(t \ in \ SE_1\right). \tag{5.5}$$

Note that in the context of a TSE $\Delta t_{1,2} = T^{TSE}$. Furthermore, the estimated rate of change of the phase angle at the *i*-th node over one period T_{ref} of the reference signal can be calculated as

$$\Delta\hat{\theta}_i^T = \frac{\hat{\theta}_i^{SE2} - \hat{\theta}_i^{SE1}}{\Delta t_{1,2}} T_{ref} \ . \tag{5.6}$$

Lastly, the estimated frequency at the *i*-th node of the system can be calculated as

$$\hat{f}_i = \left(\frac{2\pi + \Delta\hat{\theta}_i^T}{2\pi}\right) f_{ref} \ . \tag{5.7}$$

These estimated frequencies represent the average voltage frequency of each bus during the time between the PMU samples used for the SE$_1$ and the PMU samples used for the SE$_2$.

Because of the nature of the periodic sinusoidal signals, an aliasing effect can occur if the time between SE solutions is too long for the frequency deviation. For example, if the nodal voltage frequency is 61Hz and the reference is 60Hz, every one second the nodal voltage frequency will be re-synchronized with the reference signal, and no phasor change will be detected every one second between PMU samples. Moreover, to be able to correctly detect if the nodal voltage frequency is faster or slower than the reference, the time between the PMU samples used for each SE solution in the case of 1 Hz. of frequency deviation must be 0.5 seconds.

Based on the information mentioned above, the maximum time $\Delta t_{1,2}^{\max}$ between PMU samples used in two consecutive SEs for a given frequency deviation $\Delta f = \left| f_i - f_{ref} \right|$ is then given by

$$\Delta t_{1,2}^{\max} = \frac{0.5}{\Delta f} \ . \tag{5.8}$$

The National Center for Energy Control in Mexico, known as CENACE in its Spanish acronym, is responsible for the SE of the Mexican system. In this center, the SE solutions are executed every 30 or 60 seconds, and in the near future each SE will be performed considering both SCADA and PMU measurements; therefore, according to (5.8), the estimated maximum frequency deviation that could be detected without the aliasing effect for the rate of 30 seconds is 0.017 Hz.

Since the frequency deviations may be higher, three solutions are proposed to overcome this problem: i) After the first SE is executed on-line, frequency deviations up to 5 Hz. are computed off-line by using (5.8) and the set of PMU samples that arrived to the control center 0.5 seconds after the first SE. ii) The SE can be executed in a local area to be able to observe higher frequency deviations in real time through faster on-line SE executions, where 10 SE solutions per second permit observing power oscillations and to detect interarea oscillations. iii) An alternative technique can be applied, when the time between measurements scans is too large, by using three consecutive on-line SE solutions to obtain the estimated frequency, as explained next.

5.3.1 Frequency estimation for larger times between state estimations

When the system is not observable with PMUs only, SCADA measurements are needed, and a hybrid SE is executed. In this context, since the SCADA sample times are between 2 to 5 seconds, the time between two consecutive SE processes may be too large to obtain the estimated nodal frequencies with (5.6) and (5.7) according to (5.8). This problem is overcome by performing three consecutive SE solutions instead of just two. In this case, the estimated rate of change of the phase angle at the *i*-th node over one period of the reference signal T_{ref} is given by

$$\Delta\hat{\theta}_i^T = \frac{\left(\hat{\theta}_i^{SE_3} - \hat{\theta}_i^{SE_2}\right) - \left(\hat{\theta}_i^{SE_2} - \hat{\theta}_i^{SE_1}\right)}{\Delta t_{2,3} - \Delta t_{1,2}} T_{ref} \ . \tag{5.9}$$

As can be noted from (5.9), the time difference $\Delta t_{1,2}$ between the SE1 and SE2 must be different than the time difference $\Delta t_{2,3}$ between the SE2 and SE3 to avoid an indetermination. This can be achieved by choosing the PMU data samples according to the time stamp. For example, if the PMUs are reporting 10 data samples per second, between the SE1 and the SE2 the estimator can wait for 600 samples, which represents 60 seconds. On the other hand, the estimator can also wait for 601 samples, representing 60.1 seconds, between the SE2 and SE3.

The estimated nodal frequencies can be obtained by substituting (5.9) in (5.7), and by considering the maximum difference between the SE time differences. These results in the following equation that avoids the aliasing effect for a given frequency deviation:

$$\left|\Delta t_{2,3} - \Delta t_{1,2}\right|^{\max} = \frac{0.5}{\Delta f} \ . \tag{5.10}$$

As can be derived from (5.10), if $\Delta t_{1,2}$ is 60 seconds and $\Delta t_{2,3}$ is 60.1 seconds, the frequency deviation could be up to 5 Hz. so the range of frequencies that can be estimated is from 55 Hz. to 65 Hz.

5.4 Case studies

5.4.1 Nodal frequency estimation

The applicability of the nodal frequency estimation by the proposed approach, in the context of a system entirely observable by PMUs, is presented in this section.

The 50 generators and 145-bus test system presented in [Vittal *et al.* 1992] [Ortega-rivera *et al.* 2018] is used to obtain the estimates of the nodal voltage phasors with (3.23) and the nodal frequencies with (5.7). In this system, 44 machines are represented with the classical model and 6 machines are characterized by the two-axis model and an AC4A exciter.

The TSE considers the reception of 10 PMU measurement sets per second such that $\Delta t_{1,2} = T^{TSE} = 0.1\text{s}$. The system is observable through 34 PMU voltage phasor measurements and 118 PMU branch current measurements for a total set of 304 measurements.

The transient security assessment tool named TSAT, which is a time-domain simulator of the DSATools™ software, is used to generate the set of PMUs' measurements used for the TSE. For this purpose, the system is subjected to a contingency scenario defined by a solid three-phase fault, incepted at t_0=5s at node 7 and cleared at t_{cl}=5.1s. The set of true measurements is generated by considering 10 samples per second for 60 seconds of the system's dynamic behavior. Furthermore, the true values of the nodal frequencies are obtained from this software.

To simulate the noise in the measurements, a non-Gaussian noise is added to the true values, and gross errors are included. Note that the measurements with gross errors are detected and corrected during the SE process by using the bad data analysis proposed in Section 3.4.

Fig. 5.2 shows the nodal frequencies at nodes 93, 104 and 110 obtained by the proposed approach, the TSAT software and the frequency divider approach reported in [Milano & Ortega 2017]. These three nodes correspond to the point of connection of the generators represented by a six-order model without PMUs installed in their corresponding nodes.

To obtain a quality indicator, an MSE is calculated for each *i*-th node according to (5.11) for the proposed frequency estimates $\hat{f}_i^s$, while (5.12) is used for the results of the frequency divider $f_i^{FD,s}$. Note that the frequencies f_i^s obtained at the *i*-th node through the TSAT simulation are considered as the reference values, and the superindex *s* represents the number of SEs studied:

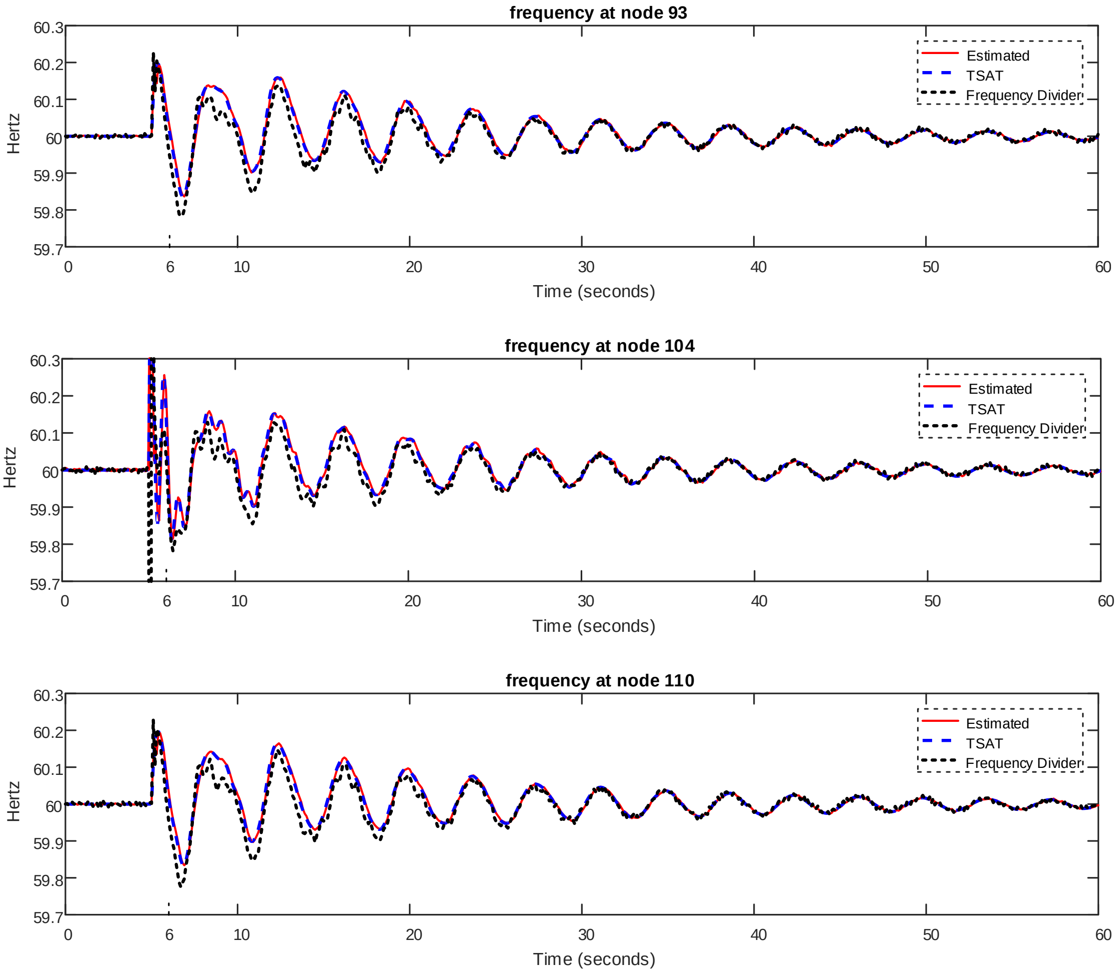

frequency at node 93

frequency at node 104

frequency at node 110

Fig. 5.2 Estimated, TSAT and frequency divider's frequencies at nodes 93, 104 and 110.

$$MSE_i = \frac{1}{540}\sum_{s=61}^{600}\left(f_i^s - \hat{f}_i^s \right)^2, \quad \forall i = 1,\ldots,145\,, \tag{5.11}$$

$$MSE_i = \frac{1}{540}\sum_{s=61}^{600}\left(f_i^s - f_i^{FD,s} \right)^2, \quad \forall i = 1,\ldots,145\,. \tag{5.12}$$

The MSEs are calculated from $t = 6s$ to $t = 60s$ to avoid in their computation the first five seconds of steady state and the large spikes that appear in the frequency divider during the fault transients. The MSEs are illustrated in Fig. 5.3, which clearly shows that the proposed method is more accurate than the frequency divider method. For the case of the proposed method, the highest MSE value of 5.995x10^{-4} corresponds to node 89. On the other hand, the highest MSE value for the frequency divider method was 1.139x10^{-2} at node 63.

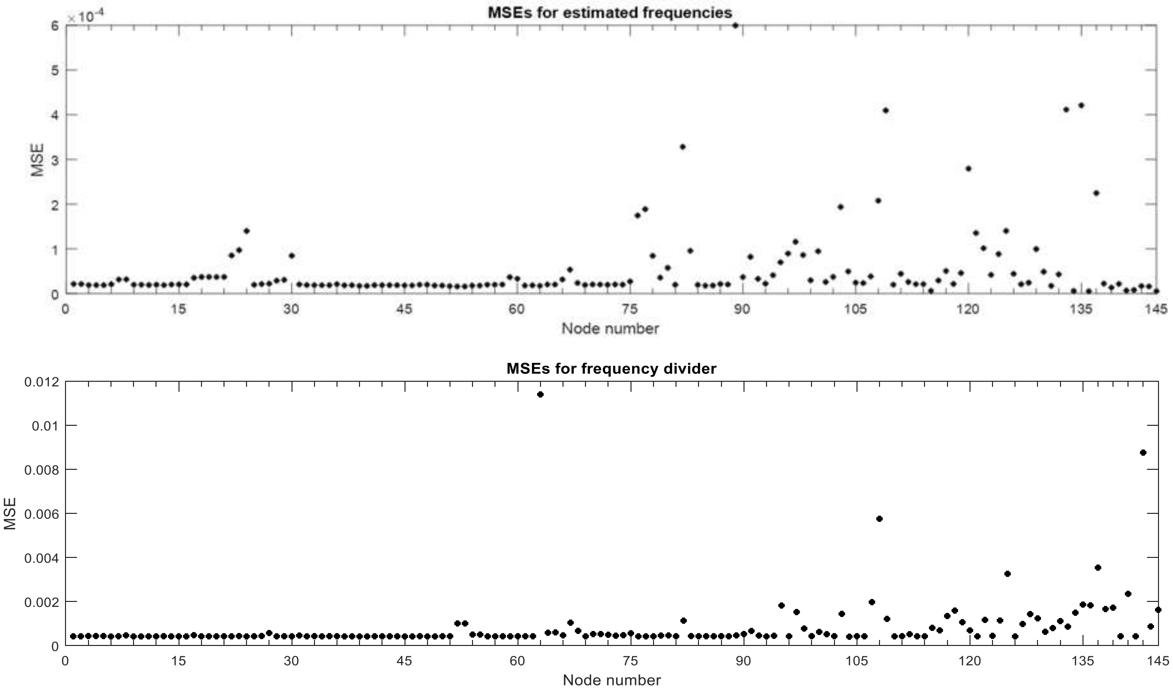

Fig. 5.3 Nodal MSEs for the estimated frequencies and the frequency divider.

Lastly, Fig. 5.4 and Fig. 5.5 shows the frequency profiles obtained by the proposed approach, the frequency divider approach and the time-domain simulation for nodes 89 and 63, respectively, where the highest MSE value are associated with the proposed method and the frequency divider method, respectively.

5.4.2 Detection of interarea oscillations

The proposed nodal frequency estimation method is applied in this section to determine interarea oscillations without requiring parametric information from the generators, such as the dynamic parameters or internal reactances. The benchmark system composed of two areas with four generators and 10 nodes, shown in Fig. 5.6, is used for this purpose. In this system, the machines are represented by the two-axis model.

The set of PMUs is composed of five measurements of voltage phasors and 11 measurements of branch currents for a total of 32 measurements, which are located as shown in Fig. 5.6.

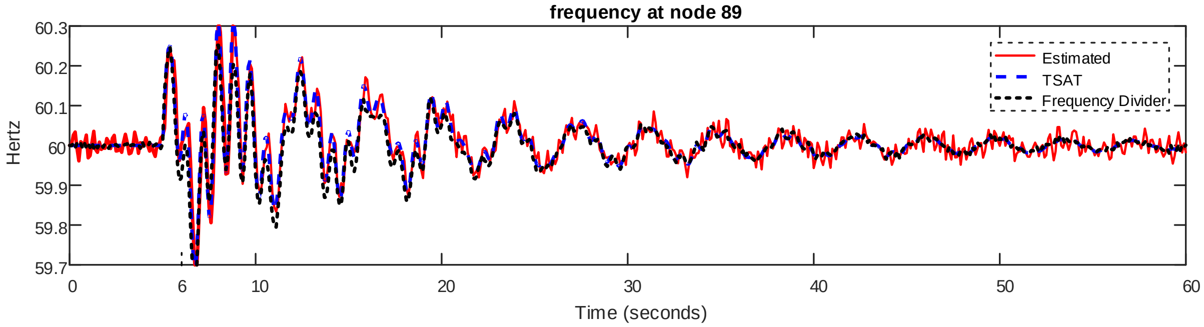

Fig. 5.4 Estimated, TSAT and frequency divider's frequencies at node 89.

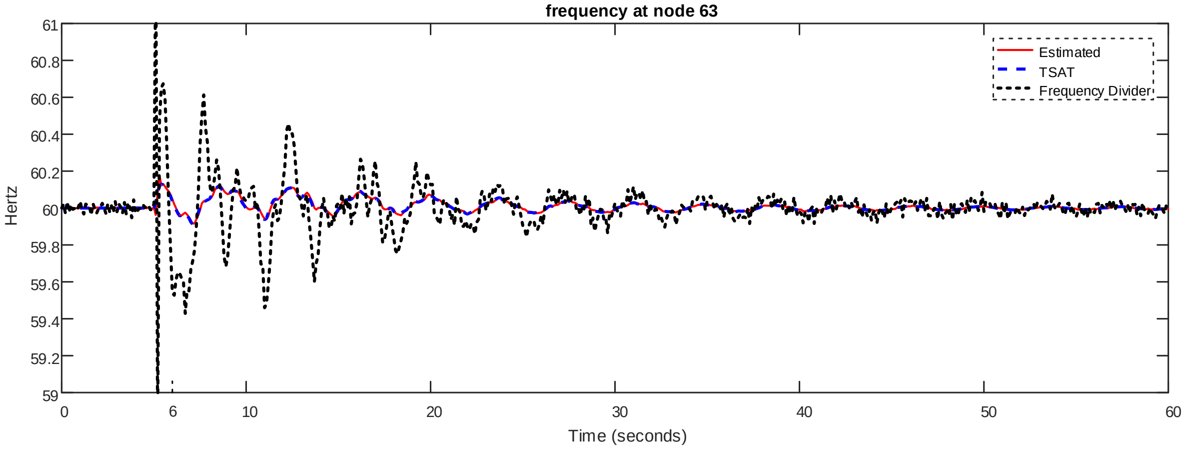

Fig. 5.5 Estimated, TSAT and frequency divider's frequencies at node 63.

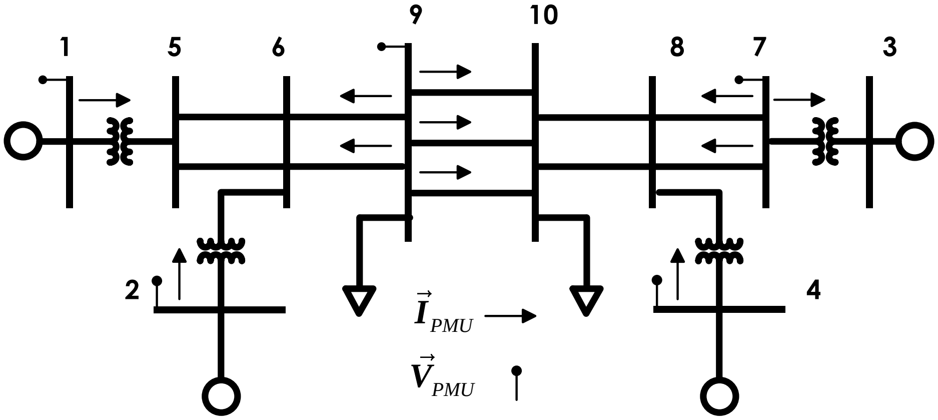

Fig. 5.6 Two-area test system.

Homemade software is used to generate the set of abovementioned measurements by considering 10 samples per second during 30 seconds of simulation. Two case studies are simulated as follows. In case 1, a three-phase short circuit on bus 9 takes place at $t = 0.1s$, which is cleared at $t = 0.115s$. For the other case, the load connected at node 9 is increased by 30% at a constant power factor for 2 seconds: from $t = 5s$ to $t = 7s$.

In both case studies, a non-Gaussian noise is added to the true values for generating the PMU measurements. Once the frequency estimates are obtained, a moving average filter of five samples is applied to reduce the noise on the estimates according to

$$\hat{f}_i^{t,\,filtered} = \left(\hat{f}_i^{t} + \hat{f}_i^{t-0.1s} + \hat{f}_i^{t-0.2s} + \hat{f}_i^{t-0.3s} + \hat{f}_i^{t-0.4s} \right) / \, 5 \, . \tag{5.13}$$

The estimated frequencies at the generators' nodes are presented in Fig. 5.7 for case study 1. From these results, the shape of the interarea mode under which generators 1 and 2 swing together against generators 3 and 4 following the disturbance is clear.

A similar dynamic behavior can be observed in Fig. 5.8 for case study 2.

Lastly, the interarea oscillation between machines 1 and 3 is obtained by simply subtracting the frequencies of node 3 from the frequencies of node 1. These interarea oscillations are presented in Fig. 5.9 and Fig. 5.10 for the case studies 1 and 2, respectively.

5.5 Conclusions

A methodology to obtain the nodal frequencies from a tracking state estimator is presented in this chapter, where the measurements' errors are reduced by the state estimator during the solution process. Furthermore, a simple average filter can be applied to obtain cleaner frequency estimates in cases where the frequency deviations are too small compared to the noise in the estimates.

When the time between estimates is too large, the frequency estimates are not useful to observe power oscillations, but the calculated estimated frequency may represent a steady frequency deviation that is important for the automatic generation control.

The nodal frequencies permit observing the behavior of the synchronous generators in the context of interarea oscillations when no machine inertias or internal parameters' information is necessary.

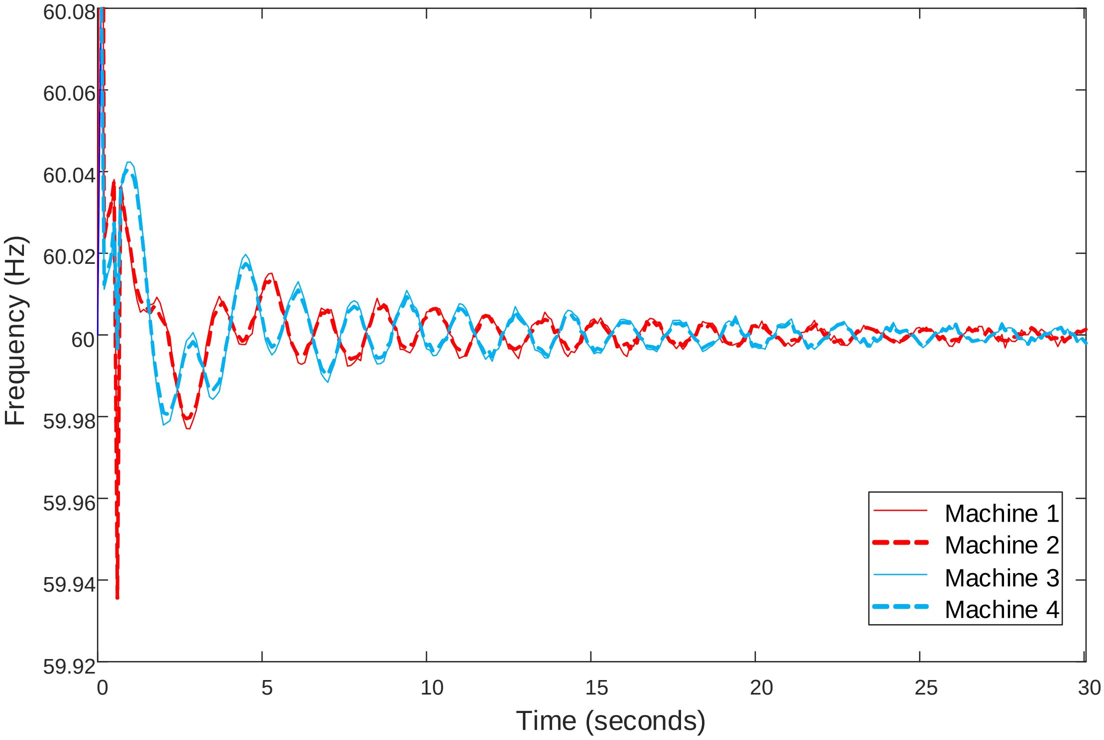

Fig. 5.7 Nodal frequencies of machines for case 1.

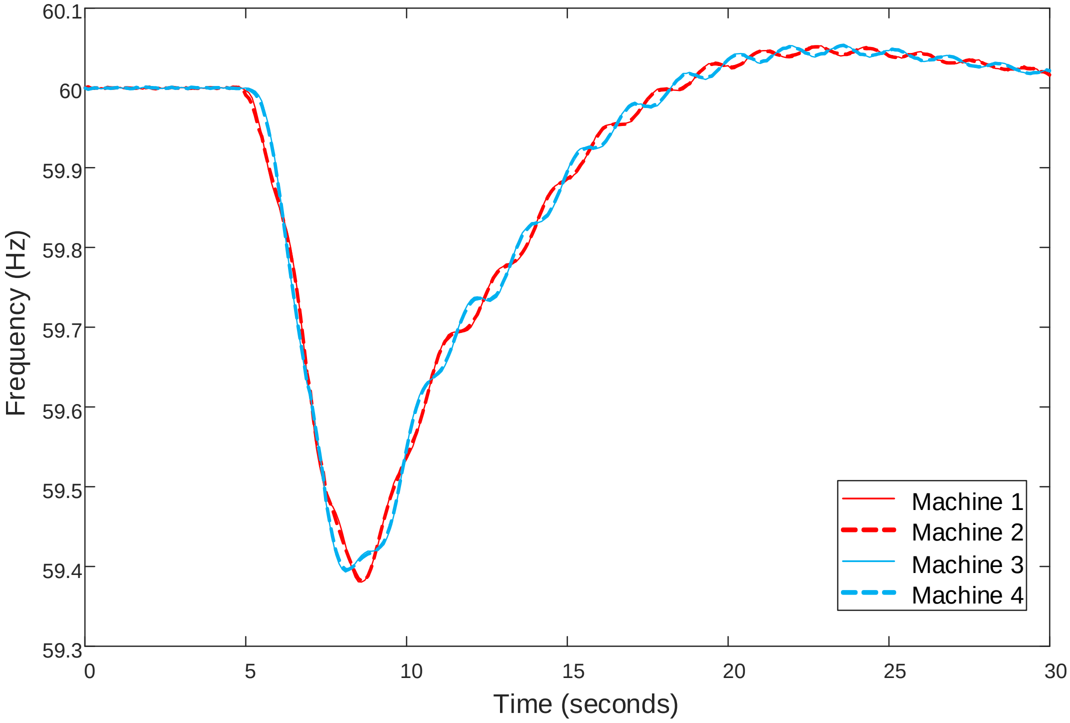

Fig. 5.8 Nodal frequencies of machines for case 2.

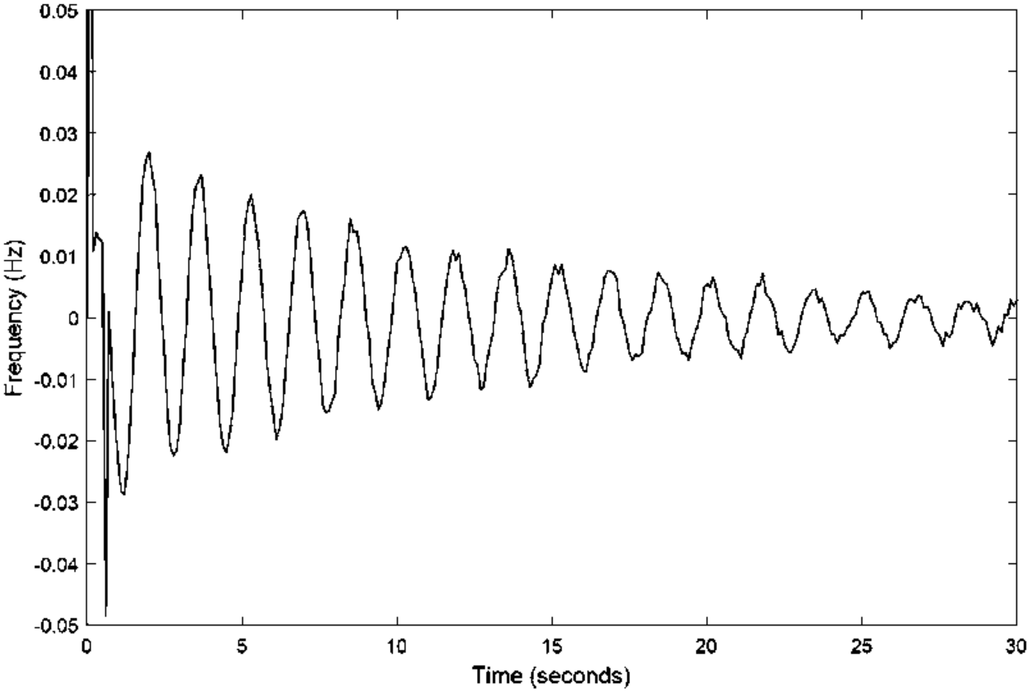

Fig. 5.9 Interarea oscillation between machines 1 and 3 in case 1.

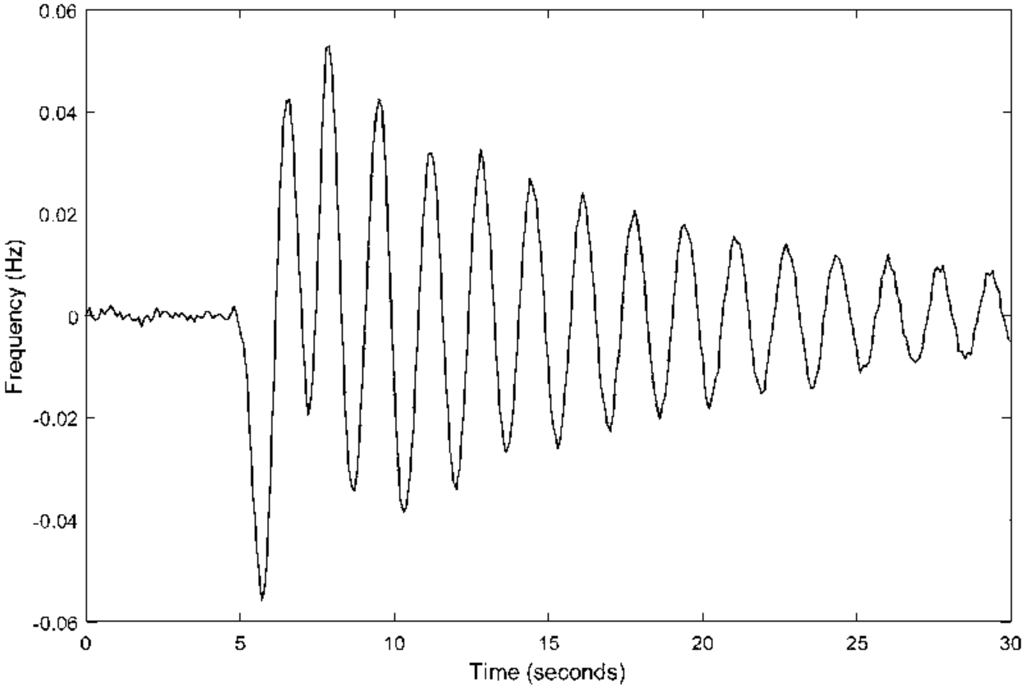

Fig. 5.10 Interarea oscillation between machines 1 and 3 in case 2.

Chapter 6

6 General conclusions and future work

6.1 Conclusions

The evolution of electrical power transmission systems into VSC-based multi-terminal AC-DC systems requires the appropriate tools for assessing their secure and economic operation. Different proposals have been made in this work to accomplish that requirement.

The proposed VSC model together with the proposed complementarity constraints' method ensures that the power flow solutions do not violate any of the converter's operational limits.

The proposed Hachtel-based state estimation approach obtained an operating state of multi-terminal AC-DC networks with a relative error in the estimates below 0.06% under the scenario where the measurements' set contained Gaussian noise and no bad data.

The quality of the estimates using the proposed bad data analysis remained almost unaltered in the presence of a measurement with a gross error, independently of the error magnitude or the measurements' errors distributions. Compared to a robust estimator, the proposal achieved estimates with 1.14 to 2.97 times better quality indicators. Under a multiple bad data scenario, the biggest absolute error in the estimates obtained with the proposed method was between 6.2 to 21.4 times smaller than the ones obtained with the robust estimator. Moreover, unlike the robust estimator, the application of the proposed method is feasible for large-scale electric power systems, like the Mexican interconnected system. Furthermore, the proposed method was between 47.7 to 121.6 times faster than the classical method used by CENACE and achieved better estimates with a bad data identification rate between 9.29 to 35.37 times higher.

The proposed constrained state estimator demonstrates its capability for improving the quality of estimates when undetectable measurements with gross errors are present. The MSE in the estimates was reduced between 1.50 to 2.84 times in the IEEE-14 bus test system, between 1.59 to 1.74 times in the CIGRE test system and between 1.45 to 3.18 times in the Mexican system.

The higher MSE in the nodal frequencies computed by using the frequency divider was 1.139×10^{-2}, while the higher MSE in the estimated nodal frequencies was only 5.995×10^{-4} with the proposed formulation. This represents an accuracy of 19 times better for frequency values with the proposed method. Moreover, the worst estimated nodal frequencies by the proposed formulation still contained the most important information about the frequency oscillation, while the least accurate frequencies obtained by using the frequency divider method completely differed from the true values. This makes the proposed formulation useful for detecting interarea oscillations and other frequency derived analysis.

6.2 Future work

Departing from the proposals reported in this thesis, future research is detailed below.

Similar to the proposed VSC model, a dynamic model can be developed where converters' transients can be taken into consideration for studies of different time frames.

A methodology to assess the optimal location of the measurement devices in order to enhance the bad data detection.

Forecasted information can be introduced in the multi-terminal AC-DC state estimator in order to take further advantage of the proposed inequality constrained approach and to obtain better estimates.

A methodology to determine the minimal number of PMUs required for a reliable nodal frequency tracking.

The estimated frequencies together with Prony's method can be used to separate the frequency oscillations into their components: frequency, amplitude, phase and damping. These elements can be used for different studies such as

- Islanding detection,
- Automatic generation control correction,
- Machines inertia estimation,
- Reverse modal analysis.

References

Abur, A., & Celik, M. K. (1993). Least absolute value state estimation with equality and inequality constraints. *IEEE Transactions on Power Systems, 8*, 680-686.

Abur, A., & Exposito, A. G. (2004). *Power system state estimation: theory and implementation.* CRC Press.

Abur, A., & Lin, Y. (2018). A Highly Efficient Bad Data Identification Approach for Very Large Scale Power Systems. *IEEE Transactions on Power Systems*.

Acha, E., & Castro, L. M. (2016). A generalized frame of reference for the incorporation of, multi-terminal VSC-HVDC systems in power flow solutions. *Electric Power Systems Research, 136*, 415-424.

Acha, E., Kazemtabrizi, B., & Castro, L. M. (2013). A new VSC-HVDC model for power flows using the Newton-Raphson method. *IEEE Transactions on Power Systems, 28*, 2602-2612.

Alcaide-Moreno, B. A., Fuerte-Esquivel, C. R., Castro, L. M., & Zamora-Cárdenas, E. A. (2015). Generalized State Estimation of Flexible AC Power Systems Considering Wind Generators and Primary Frequency Control. *Electric Power Components and Systems, 43*(13), 1534-1547.

Alcaide-Moreno, B. A., Fuerte-Esquivel, C. R., Glavic, M., & Van Cutsem, T. (2017). Electric power network state tracking from multirate measurements. *IEEE Transactions on Instrumentation and Measurement, 67*, 33-44.

Angeles-Camacho, C., Tortelli, O. L., Acha, E., & Fuerte-Esquivel, C. R. (2003). Inclusion of a high voltage DC-voltage source converter model in a Newton--Raphson power flow algorithm. *IEE Proceedings-Generation, Transmission and Distribution, 150*, 691-696.

Arrillaga, J., Liu, Y. H., & Watson, N. R. (2007). *Flexible power transmission: the HVDC options.* John Wiley & Sons.

Beerten, J., Cole, S., & Belmans, R. (2012). Generalized steady-state VSC MTDC model for sequential AC/DC power flow algorithms. *IEEE Transactions on Power Systems, 27*, 821-829.

Billups, S. C., & Murty, K. G. (2000). Complementarity problems. *Journal of Computational and Applied Mathematics, 124*, 303-318. doi:10.1016/s0377-0427(00)00432-5

Cao, J., Du, W., & Wang, H. (2012). The incorporation of generalized VSC MTDC model in AC/DC power system state estimation. *Sustainable Power Generation and Supply (SUPERGEN 2012), International Conference on*, (pp. 1-6).

Chakrabarti, S., Kyriakides, E., Ledwich, G., & Ghosh, A. (2010). Inclusion of PMU current phasor measurements in a power system state estimator. *IET generation, transmission \& distribution, 4*(10), 1104-1115.

Clements, K. A., Davis, P. W., & Frey, K. D. (1995). Treatment of inequality constraints in power system state estimation. *IEEE Transactions on Power Systems, 10*, 567-574.

Cutsem, T. V., Ribbens-Pavell, M., & Mili, L. (1984). Hypothesis testing identification: A new method for bad data analysis in power system state estimation. *Power Apparatus and Systems, IEEE Transactions on*(11), 3239-3252.

de la Villa Jaén, A., Acha, E., & Expósito, A. G. (2008). Voltage source converter modeling for power system state estimation: STATCOM and VSC-HVDC. *IEEE Transactions on Power Systems, 23*(4), 1552-1559.

Diaz, G., & Gonzalez-Moran, C. (2012). Fischer-Burmeister-Based Method for Calculating Equilibrium Points of Droop-Regulated Microgrids. *IEEE Transactions on Power Systems, 27*, 959-967. doi:10.1109/tpwrs.2011.2175754

Donde, V., Feng, X., Segerqvist, I., & Callavik, M. (2016). Distributed state estimation of hybrid AC/HVDC grids by network decomposition. *IEEE Transactions on Smart Grid, 7*(2), 974-981.

Fischer, A. (1992). A special newton-type optimization method. *Optimization, 24*, 269-284. doi:10.1080/02331939208843795

Fletcher, J., & Yang, J. (2010). Introduction to doubly-fed induction generator for wind power applications. *Paths to Sustainable Energy*, 259-278.

Gjelsvik, A., Aam, S., & Holten, L. (1985). Hachtel's augmented matrix method-A rapid method improving numerical stability in power system static state estimation. *Power Apparatus and Systems, IEEE Transactions on, 1*(11), 2987-2993.

Gol, M., & Abur, A. (2014). LAV based robust state estimation for systems measured by PMUs. *IEEE Transactions on Smart Grid, 5*, 1808-1814.

Golpîra, H., & Messina, A. R. (2018). A Center-of-Gravity-Based Approach to Estimate Slow Power and Frequency Variations. *IEEE Transactions on Power Systems, 33*, 1026-1035.

Haileselassie, T. M. (2012). Control, dynamics and operation of multi-terminal VSC-HVDC transmission systems.

Kotiuga, W. W., & Vidyasagar, M. (1982). Bad data rejection properties of weughted least absolute value techniques applied to static state estimation. *IEEE Transactions on Power Apparatus and Systems*(4), 844-853.

Leyffer, S. (2002). Complementarity constraints as nonlinear equations: Theory and numerical experience. *Optimization with Multivalued Mappings, 2*, 169-208. doi:10.1007/0-387-34221-4_9

Li, S. (2013). Power flow modeling to doubly-fed induction generators (DFIGs) under power regulation. *IEEE Transactions on Power Systems, 28*, 3292-3301.

Li, W., & Vanfretti, L. (2015). A PMU-based state estimator considering classic HVDC links under different control modes. *Sustainable Energy, Grids and Networks, 2*, 69-82.

Lin, Y., & Abur, A. (2018, 11). A Highly Efficient Bad Data Identification Approach for Very Large Scale Power Systems. *IEEE Transactions on Power Systems, 33*, 5979-5989. doi:10.1109/TPWRS.2018.2826980

Martínez-Parrales, R., & Fuerte-Esquivel, C. R. (2018). A new unified approach for the state estimation and bad data analysis of electric power transmission systems with multi-terminal VSC-based HVDC networks. *Electric Power Systems Research, 160*, 251-260.

Milano, F. (2018). Rotor Speed-Free Estimation of the Frequency of the Center of Inertia. *IEEE Transactions on Power Systems, 33*, 1153-1155.

Milano, F., & Ortega, A. (2017). Frequency divider. *IEEE Transactions on Power Systems, 32*, 1493-1501.

Mili, L., & Van Cutsem, T. (1988). Implementation of the hypothesis testing identification in power system state estimation. *Power Systems, IEEE Transactions on, 3*(3), 887-893.

Mili, L., Cheniae, M. G., Vichare, N. S., & Rousseeuw, P. J. (1996). Robust state estimation based on projection statistics [of power systems]. *IEEE Transactions on Power Systems, 11*, 1118-1127.

Monticelli, A. (2000, 2). Electric power system state estimation. *Proceedings of the IEEE, 88*, 262-282. doi:10.1109/5.824004

Nguyen, Q. H., Todeschini, G., & Santoso, S. (2019). Power Flow in a Multi-Frequency HVac and HVdc System: Formulation, Solution, and Validation. *IEEE Transactions on Power Systems*.

Ortega-rivera, I. L., Vittal, V., Heydt, G. T., Fuerte-Esquivel, C. R., & Angeles-Camacho, C. (2018). A Dynamic State Estimator Based Control for Power System Damping. *IEEE Transactions on Power Systems*.

Orths, A., Hiorns, A., van Houtert, R., Fisher, L., & Fourment, C. (2012). The European North Seas Countries' Offshore Grid initiative—The way forward. *2012 IEEE Power and Energy Society General Meeting*, (pp. 1-8).

Pizano-Martinez, A., Fuerte-Esquivel, C. R., Ambriz-Perez, H., & Acha, E. (2007). Modeling of VSC-based HVDC systems for a Newton-Raphson OPF algorithm. *IEEE Transactions on Power Systems, 22*, 1794-1803.

Qifeng, D., Boming, Z., & Chung, T. (2000). State estimation for power systems embedded with FACTS devices and MTDC systems by a sequential solution approach. *Electric Power Systems Research, 55*(3), 147-156.

Rakpenthai, C., Premrudeepreechacharn, S., Uatrongjit, S., & Watson, N. R. (2006, 9). State Estimation of Power System with UPFC Using Interior Point WLAV Method. *Proc. 38th North American Power Symp*, (pp. 411-415). doi:10.1109/NAPS.2006.359605

Sandoval-Perez, U. (2015). Assessment of the impact of wind power generation on the steady-state operation of power systems. Morelia Mich: M.S. thesis, Faculty of Electrical Eng.

Singh, H., Alvarado, F. L., & Liu, W.-.. E. (1997, 2). Constrained LAV state estimation using penalty functions. *IEEE Transactions on Power Systems, 12*, 383-388. doi:10.1109/59.575725

Sundaresh, L., & Rao, P. S. (2014). A modified Newton–Raphson load flow scheme for directly including generator reactive power limits using complementarity framework. *Electric Power Systems Research, 109*, 45-53. doi:10.1016/j.epsr.2013.12.005

Tapia-Juarez, R., Fuerte-Esquivel, C. R., Espinosa-Juarez, E., & Sandoval, U. (2018). Steady-State Model of Grid-Connected Photovoltaic Generation for Power Flow Analysis. *IEEE Transactions on Power Systems, 33*, 5727-5737. doi:10.1109/tpwrs.2018.2817585

Vanfretti, L. (2009). Phasor measurement-based state estimation of electric power systems and linearized analysis of power system network oscillations. *Rensselaer Polytechnic Institute, Troy, New York, Troy, New York*.

Vittal, V., Martin, D., Chu, R., Fish, J., Giri, J. C., Tang, C. K., . . . Farmer, R. G. (1992). Transient stability test systems for direct stability methods. *IEEE Transactions on Power Systems, 7*, 37.

Vrana, T. K., Yang, Y., Jovcic, D., Dennetiere, S., Jardini, J., & Saad, H. (2013). The CIGRE B4 DC grid test system. *Electra, 270*(1), 10-19.

Wang, S., Zhao, J., Huang, Z., & Diao, R. (2017). Assessing Gaussian assumption of PMU measurement error using field data. *IEEE Transactions on Power Delivery*.

Wu, F. F., Liu, W.-H., Holten, L., Gjelsvik, L., & Aam, S. (1988). Observability analysis and bad data processing for state estimation using Hachtel's augmented matrix method. *IEEE Transactions on Power Systems, 3*(2), 604-611.

Yazdani, A., & Iravani, R. (2010). *Voltage-sourced converters in power systems: modeling, control, and applications.* John Wiley & Sons.

Zamora-Cárdenas, E., Fuerte-Esquivel, C., Pizano-Martínez, A., & Estrada-García, H. (2016). Hybrid state estimator considering SCADA and synchronized phasor measurements in VSC-HVDC transmission links. *Electric Power Systems Research, 133*, 42-50.

Zhang, X.-P. (2004). Multiterminal voltage-sourced converter-based HVDC models for power flow analysis. *IEEE Transactions on Power Systems, 19*, 1877-1884.

Zhao, J., & Mili, L. (2016). *Matlab Code of Robust Generalized Maximum-likelihood Estimator for Power System State Estimation using Projection Statistics.* doi:10.13140/rg.2.2.19176.26888/1

Zhao, J., & Mili, L. (2018). A framework for robust hybrid state estimation with unknown measurement noise statistics. *IEEE Transactions on Industrial Informatics, 14*, 1866-1875.

Zhao, J., Zhang, G., & La Scala, M. (2016). A two-stage robust power system state estimation method with unknown measurement noise. *Power and Energy Society General Meeting (PESGM), 2016*, (pp. 1-5).

Zhou, N., Huang, Z., Meng, D., Elbert, S., Wang, S., & Diao, R. (2014). Capturing dynamics in the power grid: Formulation of dynamic state estimation through data assimilation. *Pacific Northwest Nat. Lab., Richland, WA, USA, Tech. Rep. PNNL-23213.*